Appendix D

$K_L^0 \to \pi^+\pi^-\gamma$ Decay

The decay $K_L^0 \to \pi^+\pi^-\gamma$ is a radiative three-body decay. Using the photon energy in the kaon rest frame (E_γ^{CM}) and the kaon mass (M_K), the $\pi^+\pi^-$ invariant mass $M_{\pi\pi}$ is given as

$$M_{\pi\pi} = M_K \sqrt{1 - \frac{2\,E_\gamma^{CM}}{M_K}} < M_K \,.$$

The $K_L^0 \to \pi^+\pi^-\gamma$ events are thereby seen on the *lower* side of the $K_L^0 \to \pi^+\pi^-$ peak in the $M_{\pi\pi}$ distribution. Experiments to measure the $K_L^0 \to \pi^+\pi^-\gamma$ branching ratio are limited by the minimum photon energy that can be detected. The current branching ratio is obtained [62,18] :

$$B.R.(\,K_L^0 \to \pi^+\pi^-\gamma\,;\, E_\gamma^{CM} > 20\,MeV\,) = (\,4.41 \pm 0.32\,) \times 10^{-5}\,.$$

$E_\gamma^{CM} > 20 MeV$ corresponds to $M_{\pi\pi} < 477\,MeV/c^2$.

The $K_L^0 \to \pi^+\pi^-\gamma$ decay is made up of the following two processes [63].

1. *inner bremsstrahlung* (IB) :

   A photon is radiated by one of the charged pions from the $K_L - \pi\pi$ vertex, as shown in Fig A.4(a). It is a CP-*violating* process ($K_L(\,CP-\,) \to \pi^+\pi^-\gamma(\,CP+\,)$) and is suppressed in the K_L decay. The photon energy spectrum in the rest frame shows an $1/E_\gamma^{CM}$ behaviour and diverges when $E_\gamma^{CM} \to 0$. However, the events whose photon energies are less than the minimum detectable value of a given experiment are not observed and regarded as the $K_L^0 \to \pi^+\pi^-$ events. The measured $K_L^0 \to \pi^+\pi^-$ branching ratio included the contribution by low photon-energy $K_L^0 \to \pi^+\pi^-\gamma$ events[1] and the divergence is canceled in the *radiative corrections* of the $K_L^0 \to \pi^+\pi^-$ decay. The current experimental value is [62]:

   $$B.R.(\,K_L^0 \to \pi^+\pi^-\gamma\,;\, I.B.\,E_\gamma^{CM} > 20\,MeV\,) = (\,1.52 \pm 0.16\,) \times 10^{-5}\,.$$

2. *direct emission* (DE) :

   A photon comes directly from the $K_L - \pi\pi$ vertex as shown in Fig A.4(b) by M1 transition. It *conserves* CP ($K_L(\,CP-\,) \to \pi^+\pi^-\gamma(\,CP-\,)$). The photon energy spectrum is proportional to $(\,E_\gamma^{CM}\,)^3 \cdot (\,1 - 2\,E_\gamma^{CM}\,/\,M_K\,)$, which remains finite when $E_\gamma^{CM} \to 0$. This process is dominant for $E_\gamma^{CM} > 50\,MeV$. The current experimental value is [62]:

   $$B.R.(\,K_L^0 \to \pi^+\pi^-\gamma\,;\, D.E.\,E_\gamma^{CM} > 20\,MeV\,) = (\,2.89 \pm 0.28\,) \times 10^{-5}\,.$$

A Monte Carlo simulation for the $K_L^0 \to \pi^+\pi^-\gamma$ decay was made as follows. The decay generation routine for three-body decays was modified so as to chose the energies of the positive and negative pions using the *theoretical* formula [63] of the $K_L^0 \to \pi^+\pi^-\gamma$ decay. The minimum photon energy E_c was set to $0.5\,MeV$, which meant the $\pi\pi$ invariant mass was less than $497.17\,MeV$, and the measured $K_L^0 \to \pi^+\pi^-\gamma$ branching ratio with $E_\gamma^{CM} > 20\,MeV$ was extrapolated to the value with $E_\gamma^{CM} > 0.5\,MeV$ using the assumed photon energy spectrum in each of the two processes. We used, for example,

$$B.R.(\,K_L^0 \to \pi^+\pi^-\gamma\,;\, I.B.\,E_\gamma^{CM} > 0.5\,MeV\,) = (\,6.54 \pm 0.69\,) \times 10^{-5}\,.$$

The photon energy spectrum used for the simulation is shown in Fig A.5.

Fig. 5.4 in Section 5.2 was obtained by adding the Monte Carlo distributions of $K_L^0 \to \pi^+\pi^-$ and $K_L^0 \to \pi^+\pi^-\gamma$ events with proper weights. Furthermore, the distribution of $K_L^0 \to \pi^+\pi^-$ events was multiplied by the following factor :

$$(\,1 + \beta \ln \frac{E_c}{M_K/2}\,) \sim \left[\frac{E_c^{CM}}{M_K/2}\right]^\beta = 0.956\,,$$

[1] In *Review of Particle Properties* [18] it is stated : ' Most of this radiative mode, the low-momentum γ part, is also included in the parent mode listed without γ's. '

where β is the *Bond factor* :

$$\beta = \frac{2\alpha}{\pi}\left(2\ln\frac{M_K}{m_\pi} - 1\right) = 0.00717\,.$$

These factors were used in the radiative correction for the $K_L^0 \to \pi^+\pi^-$ decay.

Though there is some doubt as to the use of a fixed value of E_c, we think that this simulation is sufficient to generate the $M_{\pi\pi}$-distribution tail from the $K_L^0 \to \pi^+\pi^-$ decay.[2] It was also used to estimate the contamination of $\pi\pi(\gamma)$ events in the samples for particle identification, which was small and corrected for in the calculation of the efficiencies.

[2]The result of the simulation with $E_c = 1.0\,MeV$ was almost the same as that of the simulation with $E_c = 0.5\,MeV$.

Appendix E

Sample Selection for Particle ID Efficiencies

The muon, pion, and electron samples in each arm were selected from the minimum bias $K_L^0 \to \pi^+\pi^-$ events (Section 5.2). Events were selected with the same criteria except for the cut on *UD* and, in order to reject the $K_L^0 \to \pi^+\pi^-$ decay,

$$M_{\pi\pi} < 484\,MeV/c^2 \;\; or \;\; M_{\pi\pi} > 511\,MeV/c^2$$

was required. For the leptonic mode the efficiencies were computed with the events which satisfied the *parallel* coincidence requirement of the hodoscopes in both arms. For each event in the sample, the arm used for the particle identification (ID) efficiency measurement was named the " PID arm ", while the other arm, which was used to identify a specific decay mode, was named the " TAG arm ".

muon sample

The muon sample, which consisted of muons from the $K_L^0 \to \pi\mu\nu$ decay, was selected by tagging the pion in the TAG arm. To tag a pion by the muon identifier, a track which had no hit in MU-2, MU-3, and MU-4 and whose momentum was greater than $1.5\,GeV/c$ was used. This criterion[1] was named the " PION-tag ". The muon sample

[1]It was used only for the sample selection and was independent of the pion identification efficiency described in Section 4.3.

selection criteria were : $M_{\pi\pi} < 480\,MeV/c^2$, and a track which had a PION-tag in the muon identifier and was not " suspected " to an electron[2] in the TAG arm.

To measure the muon ID efficiency in the muon identifier, ε_{μ}^{MU}, a track which was not " suspected " to an electron in the PID arm was used. This rejected the electron from the $K_L^0 \to \pi e\nu$ decay. The efficiency of the muon to satisfy the PION-tag criterion, $\varepsilon_{\mu\to PION}^{MU}$, was also measured with this sample. The response of the Čerenkov counter and the shower counter to the muon (the efficiency of the muon to be *misidentified* as an electron by the Cerenkov counter, $\varepsilon_{\mu\to e}^{CH}$, or by the shower counter, $\varepsilon_{\mu\to e}^{EM}$, and the efficiency of the muon to be *discarded* by the shower counter, $\varepsilon_{\mu\to x}^{EM}$) was checked with the tracks which were identified as muons by the muon identifier in the PID arm. Tracks which were not " suspected " to electrons by the shower counter were used to check the Čerenkov counter, and tracks which were not identified as electrons by the Čerenkov counter were used to check the shower counter.

pion sample

The pion sample was selected by taking the electron from the $K_L^0 \to \pi e\nu$ decay in the Tag arm. The track in the TAG arm was identified as an electron by both the Čerenkov counter and the shower counter and was not identified as a muon by the muon identifier. The efficiency of the pion to be *misidentified* as an electron by the Čerenkov (shower) counter, $\varepsilon_{\pi\to e}^{CH}$ ($\varepsilon_{\pi\to e}^{EM}$), was measured with the tracks which were not identified as electrons by the shower (Čerenkov) counter in the PID arm. The efficiency of the pion to be *misidentified* as a muon by the muon identifier, $\varepsilon_{\pi\to\mu}^{MU}$ was measured with the same tracks as those for the shower counter.

electron sample

The electron sample consisted of electrons from the $K_L^0 \to \pi e\nu$ decay. The tracks were not identified as electrons by both the Čerenkov counter and the shower counter and were not identified as muons by the muon identifier in the TAG arm. The electron ID

[2]As used for muon identification (Section 4.3), a track with proper ADC information in the Čerenkov counter or the shower counter was " suspected " to be an electron track and was discarded.

efficiency in the Čerenkov (shower) counter, ε_e^{CH} (ε_e^{EM}), was measured by identifying an electron by the the shower (Čerenkov) counter in the PID arm. The efficiency of the electron to be *misidentified* as a muon by the muon identifier, $\varepsilon_{e\to\mu}^{MU}$, was measured with the tracks identified as electrons by both the Čerenkov counter and the shower counter.

remarks on the samples and efficiencies

Physically it is difficult to think of an electron that really penetrated the shower counter and the muon identifier, or a muon or a pion with a signal in the Čerenkov counter, or a muon with an energy deposit in the shower counter. The efficiencies $\epsilon_{\mu\to e}^{CH}$, $\epsilon_{\mu\to e}^{EM}$, $\epsilon_{\mu\to x}^{EM}$, $\epsilon_{\pi\to e}^{CH}$, and $\epsilon_{e\to\mu}^{MU}$ were mainly due to accidental hits of the counters.

Since there were two independent detectors for electron identification, a pure electron sample and, by tagging the electron in the TAG arm, a pure pion sample could be obtained. The contamination of these samples by other particles was negligible. The effect of the decay muon contained in the pion sample, estimated by using the Monte Carlo $K_L^0 \to \pi e\nu$ events, was subtracted from the pion misidentification efficiency $\epsilon_{\pi\to\mu}^{MU}$ obtained with the pion sample.

For the muon sample, however, pion contamination had to be estimated and corrected for to determine the muon identification efficiency ϵ_{μ}^{MU}. To do this it was necessary to know the efficiency of the muon to satisfy the PION-tag criteria. The value $\varepsilon_{\mu\to PION}^{MU}$ obtained with the muon sample was $0.4 \sim 0.6\,\%$, but the value calculated by using the misidentification efficiency in each counter, was about one third of it. This latter value is considered to be more true than the first one. It was because in the events which satisfied the PION-tag criteria in the PID arm there existed the $K_L^0 \to \pi\mu\nu$ events with a pion in the *PID arm* and the muon in the *TAG arm*. The number of such events was the same as that of the true muon tracks in the PID arm. There also existed $K_L^0 \to \pi^+\pi^-\gamma$ events and the $K_L^0 \to \pi e\nu$ events, whose electrons survived the rejection criteria.[3] Using $\varepsilon_{\mu\to PION}^{MU}$ the correction for the contamination, which came mainly from

[3]Since the efficiency of the electron to satisfy the PION-tag criteria was assumed to be 1.0. Since it was much larger than $\varepsilon_{\mu\to PION}^{MU}$, the contamination of this decay was not negligible in this case.

the pions of $K_L^0 \to \pi\mu\nu$ events whose muon satisfied the PION-tag criteria, increased the muon identification efficiency by about 0.5 %. This correction was done for each cycle and for each momentum bin (see Section 5.4). An example of the efficiencies is shown in Tables E.6, E.7, and E.8.

References

[1] M. Bott-Bodenhausen et al., *Phys. Lett.* **B24** (1967), 194.

[2] V. L. Fitch et al., *Phys. Rev.* **164** (1967), 1711.

[3] H. Foeth et al., *Phys. Lett.* **B30** (1969), 282.

[4] P. Darriulat et al., *Phys. Lett.* **B33** (1970), 249.

[5] S. L. Glashow, J. Iliopoulos, and L. Maiani, *Phys. Rev.* **D2** (1970), 1285.

[6] J. J. Aubert et al., *Phys. Rev. Lett.* **33** (1974), 1404.
J. -E. Augustin et al., *Phys. Rev. Lett.* **33** (1974), 1406.
C. Bacci et al., *Phys. Rev. Lett.* **33** (1974), 1408.

[7] A. R. Clark et al., *Phys. Rev. Lett.* **26** (1971), 1667.

[8] W. C. Carithers et al., *Phys. Rev. Lett.* **30** (1973), 1336.
W. C. Carithers et al., *Phys. Rev. Lett.* **31** (1973), 1025.

[9] Y. Fukushima et al., *Phys. Rev. Lett.* **36** (1976), 348.

[10] M. J. Shochet et al., *Phys. Rev. Lett.* **39** (1977), 59.
M. J. Shochet et al., *Phys. Rev.* **D19** (1979), 1965.

[11] Particle Data Group, G. P. Yost et al., *Phys. Lett.* **B204** (1988), 1.

[12] H. B. Greenlee et al., *Phys. Rev. Lett.* **60** (1988), 893.
E. Jastrzembski et al., *Phys. Rev. Lett.* **61** (1988), 2300.
S. F. Schaffner et al., *Phys. Rev.* **D39** (1989), 990.

[13] T. Inagaki et al., *Phys. Rev.* **D40** (1989), 1712.

[14] C. Mathiazhagan et al., *Phys. Rev. Lett.* **63** (1989), 2181.

C. Mathiazhagan et al., *Phys. Rev. Lett.* **63** (1989), 2185.

[15] A. P. Heinson et al., *Phys. Rev.* **D44** (1991), R1.

[16] L.-F. Li, in *Medium- and High- Energy Nuclear Physics, proceedings of the International Conference, Taipei, Taiwan,* 1988, edited by W.-Y. Pauchy Huang, Keh-Fei Liu, and Yiharn Tzeng (World Scientific, Singapore, 1989).

[17] L. M. Sehgal, *Phys. Rev.* **183** (1969), 1511.

[18] Particle Data Group, J. J. Hernández et al., *Phys. Lett.* **B239** (1990), 1.

[19] B. R. Martin, E. de Rafael, and J. Smith, *Phys. Rev.* **D2** (1970), 179.

[20] H. Stern and M. Gaillard, *Ann. Phys. (N.Y.)* **76** (1973) 580.

A. D. Dolgov, V. I. Zakharov, and L. B. Okun, *Usp. Fiz. Nauk* **107** (1972) 537. [*Sov. Phys. Usp.* 15 (1973) 404.]

[21] *KEK-PS User's Handbook (in Japanese)*, edited by J.Imazato (KEK, Tsukuba, 1988).

[22] T. K. Ohska et al., *KEK Report* **85-10** (1985); *IEEE Trans. Nucl. Sci.* **33** (1986) 98.

[23] T. K. Komatsubara, *Master Thesis,* Univ. of Tokyo *(in Japanese)* (1989).

[24] J. Toyoura, *Master Thesis,* Univ. of Tokyo *(in Japanese)* (1988).

[25] T. Inagaki et al., *KEK Internal* **85-1** (1985).

[26] T. Inagaki et al., *KEK Preprint* **88-26** (1988). (Contributed to the 24th International Conference on High Energy Physics, Munich, August 4-10, 1988)

[27] M.Kuze, *Doctor Thesis,* Univ. of Tokyo (1990).

[28] S. S. Yamamoto (KEK E137 Collaboration), *Nucl. Phys.* **A527** (1991), 731c.

[29] J. R. Sanford and C. L. Wang, *BNL reports* **11279** and **11479** *(unpublished)* (1967).

[30] P. Skubic et al., *Phys. Rev.* **D18** (1978), 3115.

[31] M. Sakamoto, *Senior Report,* Univ. of Tokyo *(in Japanese)* (1989).

[32] R. D. Cousins et al., *BNL proposal* # **791** (1984).

[33] H. Wind, *Nucl. Instr. and Meth.* **115** (1974), 431.

[34] M. Regler and R. Frühwirth, in *Proceedings of the Fifth NATO Advanced Study Institute on Techniques and Concepts of High Energy Physics, St. Croix, U.S. Virgin Islands,* 1988, edited by T. Ferbel (Plenum Press, New York, 1989).

R. Bock et al. *Data analysis techniquies for high-energy physics experiments* (Cambridge University Press, Cambridge, 1990).

[35] G. R. Lynch and O. I. Dahl, *Nucl. Instr. and Meth.* **B58** (1991), 6.

[36] N. M. Kroll and W. Wada, *Phys. Rev.* **98** (1955), 1355.

T. Miyazaki and E. Takasugi, *Phys. Rev.* **D8** (1973), 2051.

[37] G. D. Barr et al. *Phys. Lett.* **B259** (1991), 389.

[38] T. Akagi, *Doctor Thesis,* Tohoku Univ. (1992).

[39] C. Alff-Steinberger et al., *Phys. Lett.* **21** (1966), 595.

[40] P. A. Aarnio, J. Ranft, and G. R. Stevenson, *CERN Internal Report* **No. TIS-RP/106-Rev**, (1984) (unpublished).

[41] T. Akagi et al., *Phys. Rev. Lett.* **67** (1991), 2614.

[42] C. Campagnari (CDF Collaboration), in proceedings of the 25th International Conference on High Energy Physics, Singapore, 1990, edited by K. K. Phua and

Y. Yamaguchi (South Asia Theoretical Physics Association, Physical Society of Japan and co-sponsoring associations, 1991), 454.

[43] G. R. Harris and J. L. Rosner, *Enrico Fermi Institute preprint EFI* **91-38-Rev** (1991).

[44] M. Kobayashi and T. Maskawa, *Prog. Theor. Phys.* **49** (1973) 652.

[45] L. Maiani, in *Proceedings of the International Symposium on Lepton and Photon Interactions at High Energies, Hamburg,* 1977, edited by F.Gutbrod (DESY, Hamburg, 1977).

L. Wolfenstein, Phys. Rev. Lett. **51** (1983) 1945.

[46] N. Cabibbo, *Phys. Rev. Lett.* **10** (1963) 531.

[47] C. Q. Geng and P. Turcotte, *UdeM-LPN-TH-* **66** (1991).

C. Q. Geng, talk at the *KEK Workshop on Rare Kaon Decay Physics, KEK, Tsukuba,* 1991.

[48] G. Bélanger and C. G. Geng, *Phys. Rev.* **D43** (1991), 140.

C. Q. Geng and J. N. Ng, in proceedings of the 25th International Conference on High Energy Physics, Singapore, 1990, edited by K. K. Phua and Y. Yamaguchi (South Asia Theoretical Physics Association, Physical Society of Japan and co-sponsoring associations, 1991), 1050.

[49] T. Inami and C. S. Lim, *Prog. Theor. Phys.* **65** (1981) 297; **65** (1981) 1772(E).

[50] C. S. Kim, J. L. Rosner and C. -P. Yuan, *Phys. Rev.* **D42** (1990), 96.

[51] L. Bergström, E. Massó, and P. Singer, *Phys. Lett.* **B249** (1990), 141.

P. Singer, *Nucl. Phys.* **A527** (1991), 713c.

[52] C. Q. Geng and J. N. Ng, *Phys. Rev.* **D41** (1990), 2351.

[53] V. Barger, W. F. Long, E. Ma, and A. Pramudita, *Phys. Rev.* **D25** (1982), 1860.

[54] L. Bergström, E. Massó, P. Singer, and D. Wyler, *Phys. Lett.* **B134** (1984), 373.

[55] G. D. Barr et al. *Phys. Lett.* **B240** (1990), 283.

[56] K. E. Ohl et al., *Phys. Rev. Lett.* **65** (1990) 1407.

[57] M. S. Atiya et al., *Phys. Rev. Lett.* **64** (1990) 21.

[58] L. S. Littenberg, *Phys. Rev.* **D39** (1989), 3322.

[59] K. Arisaka, talk at the *KEK Workshop on Rare Kaon Decay Physics, KEK, Tsukuba,* 1991.

[60] T. Inagaki, talk at the *KEK Workshop on Rare Kaon Decay Physics, KEK, Tsukuba,* 1991.

[61] J. B. Marion and B. A. Zimmerman, *Nucl. Instr. and Meth.* **51** (1967) 93.

[62] A. S. Carroll et al., *Phys. Rev. Lett.* **44** (1980) 529.

[63] B. de Witt and J. Smith, *Field Theory in Particle Physics volume 1* (North-Holland, Amsterdam, 1986).

Experiment	Year	$N_{\mu\mu}$	Branching Ratio (10^{-9})	Reference
Bott-Bodenhausen et al.	1967	0	< 1600	[1]
Fitch et al.	1967	0	< 35000	[2]
Foeth et al.	1969	0	< 210	[3]
Darriulat et al.	1970	0	< 26	[4]
Clark et al.	1971	0	< 1.82	[7]
Carithers et al.	1973	9	12^{+8}_{-4}	[8]
Fukushima et al.	1976	3	$8.8^{+10.7}_{-5.5}$	[9]
Shochet et al.	1979	16	$8.1^{+2.8}_{-1.7}$	[10]
(PDG average)	1988		$9.5^{+2.4}_{-1.5}$	[11]
Schaffner et al.[E780]	1989	8	-	[12]
Inagaki et al.[E137]	1989	54	8.4 ± 1.1	[13]
Mathiazhagan et al.[E791]	1989	87	$5.8 \pm 0.6 \pm 0.4$	[14]
Heinson et al.[E791]	1991	281	$7.6 \pm 0.5 \pm 0.4$	[15]
(average)		368	7.0 ± 0.5	

Table A.1: $K_L^0 \to \mu^+\mu^-$ branching ratios from previous experiments

Material	Radiation length (10^{-3})	Nuclear interaction length (10^{-3})	Nuclear collision length (10^{-3})
decay chamber ($< 0.4\ Torr$, $10\ m$)	< 0.017	< 0.007	< 0.010
exit window	1.60	0.79	1.13
air ($23\ cm$)	0.76	0.31	0.45
drift chamber W1	1.08	0.27	0.39
helium bag	0.44	0.39	0.53
drift chamber W2	1.08	0.27	0.39
helium bag	0.61	0.64	0.85
drift chamber W3	1.08	0.27	0.39
helium bag	0.61	0.64	0.85
drift chamber W4	1.08	0.27	0.39
helium bag	0.44	0.39	0.53
drift chamber W5	1.17	0.31	0.45
Total	< 9.97	< 4.56	< 6.35

Table B.1: Radiation length, nuclear interaction length, and nuclear collision length up to W5

Detector	Z (cm)	X (cm)	Y (cm)
drift chamber W1	40	30.5 - 145.7	±43.2
drift chamber W2	135	35.7 - 150.9	±43.2
upstream magnet	225	44.2 - 174.2	±50.0
drift chamber W3	320	49.7 - 164.9	±57.6
downstream magnet	415	47.5 - 177.5	±50.0
drift chamber W4	505	54.7 - 169.9	±57.6
drift chamber W5	600	54.7 - 169.9	±57.6
hodoscope H1	620	54.9 - 170.1	±57.6
gas Čerenkov CH	646 - 812	47.4 - 177.6	±75.1
hodoscope H2	820	52.5 - 172.5	±70.0
shower counter EM	850 - 868	48.3 - 176.7	±76.0
muon identifier MU1	900	45.0 - 177.0	±81.0
muon identifier MU2	962	45.0 - 177.0	±81.0
muon identifier MU3	1003	41.0 - 181.0	±84.0
muon identifier MU4	1044	41.0 - 181.0	±84.0

Table B.2: Z position and X–Y coordinates covered by each detector element.

Cycle	label	# of shifts	Intensity (10^{12}ppp)	Production angle (degree)	Prescaling factor	# of lepton runs
88-3	K	25	1.0	0	300	99
88-5	L	28	1.1	0	300	127
					500	7
88-6	M	24	1.0	0	300	82
					500	36
88-7	N	24	$1.2 \sim 1.3$	0	500	134
88-8	O	25	$1.1 \sim 1.2$	0	500	112
88-9	P	26	$1.3 \sim 1.5$	0	500	189
88-10	Q	32	$1.3 \sim 1.5$	0	500	454
88-11		26				
88-12	R	22	$1.0 \sim 1.2$	0	500	227
88-13		26				
88-14	S	25	$1.4 \sim 1.5$	0	500	463
89-1		27				
89-2	T	25	$1.4 \sim 1.6$	0	500	173
89-3/4	U	47	$1.4 \sim 1.5$	0	500	266
89-5	V	43	$1.4 \sim 1.5$	0	500	317
89-6	W	44	$1.3 \sim 1.4$	0	500	298
89-7	X	40	$1.3 \sim 1.5$	0	500	302
89-8	Y	42	$1.2 \sim 1.3$	0	500	187
			$0.5 \sim 1.2$	0	300	46
PHASE-1		551				3519

Table C.1: Number of the lepton run and beam line condition for each cycle in the PHASE-1

Cycle	label	# of shifts	Intensity (10^{12}ppp)	Production angle (degree)	Prescaling factor	# of lepton runs
89-9	ZA	39	$0.9 \sim 1.2$	1	250	69
89-10	ZB	39	$0.9 \sim 1.2$	1	250	105
89-11	ZC	40	$1.2 \sim 1.5$	1,2	250	170
				0	500	33
89-12	ZD	39	$1.8 \sim 2.0$	2	250	175
			$2.4 \sim 2.5$	2	500	56
90-1	ZE	42	$2.5 \sim 2.6$	2	500	320
			1.2	2	250	3
90-2	ZF	42	$2.5 \sim 2.6$	2	500	180
			$1.5 \sim 1.8$	2	250	7
EXTENSION		241				1118
Total		792				4637

Table C.2: Number of the lepton run and beam line condition for each cycle in the EXTENSION

Detector	PHASE-1 0 *degree*	EXTENSION 2 *degrees*	
	1.5×10^{12} ppp	1.5×10^{12} ppp	2.5×10^{12} ppp
counting rate	MHz	MHz	MHz
W1L(plane)	60.	-	48.
(hottest wire)	0.87	-	0.69
H1	7.01	3.86	5.53
EMF	18.23	11.06	15.55
CH	2.12	1.08	1.48
MU1	6.23	3.09	4.26
MU2	2.31	1.08	1.49
MU3	2.94	1.40	1.97
MU4	3.29	1.54	2.17
chamber current	μA	μA	μA
W1,W2	165	88	145
W3	160	60	110
W4,W5	71	35	63
# of hit per plane			
W1,W2	10	7	9
W3	9	5	7
W4,W5	6	4	5
H1	2.0	1.6	1.8

Table C.3: Single counting rate of each detector at the first discriminator, the drift chamber current, and the averaged number of hits per plane.

Signal	PHASE-1 0 *degree*	EXTENSION 2 *degrees*	
	1.5×10^{12} ppp	1.5×10^{12} ppp	2.5×10^{12} ppp
(Prescaling factor)	500	250	500
counting rate	Hz	Hz	Hz
parallel	$496K$	$253K$	$376K$
Para	$12.8K$	$5.6K$	$9.2K$
Spara	$30.1K$	$13.8K$	$22.7K$
muon	$329K$	$150K$	$212K$
electron	$78K$	$332K$	$440K$
master trigger	204	178	228
$\mu_L\mu_R$	34	21	31
$\mu_L e_R$	45	33	50
$e_L\mu_R$	37	33	50
$e_L e_R$	20	34	54
$\pi\pi$	59	39	32
hardware-filter OK	(×90.2%)	(×68.5%)	(×83.2%)
	184	122	190
software-filter OK	(×76.7%)	(×84.0%)	(×93.7%)
	140	102	154
(dead-time)	6.7%	3.9%	6.3%

Table C.4: Counting rates at various trigger stages, and the dead-time ratio.

plane No. i	Z_i (cm)	$Z_{i+1} - Z_i$ (cm)	chamber plane
1	38.40	0.78	W1 X
2	39.18	1.64	W1 X'
3	40.82	0.78	W1 Y
4	41.60	17.40	W1 Y'
5	59.00	19.00	
6	78.00	19.00	
7	97.00	19.00	
8	116.00	17.40	
9	133.40	0.78	W2 X
10	134.18	1.64	W2 X'
11	135.82	0.78	W2 Y
12	136.60	16.90	W2 Y'
13	153.50	18.50	
14	172.00	18.50	
15	190.50	18.50	
16	209.00	18.50	
17	227.50	18.50	
18	246.00	18.50	
19	264.50	18.50	
20	283.00	18.50	
21	301.50	16.90	
22	318.40	0.78	W3 X
23	319.18	1.64	W3 X'
24	320.82	0.78	W3 Y
25	321.60	16.90	W3 Y'
26	338.50	18.50	
27	357.00	18.50	
28	375.50	18.50	
29	394.00	18.50	
30	412.50	16.50	
31	431.00	18.50	
32	449.50	18.50	
33	468.00	18.50	
34	486.50	16.90	
35	503.40	0.78	W4 X
36	504.18	1.64	W4 X'
37	505.82	0.78	W4 Y'
38	506.60	17.40	W4 Y
39	524.00	19.00	
40	543.00	19.00	
41	562.00	19.00	
42	581.00	17.40	
43	598.40	0.78	W5 X
44	599.18	1.64	W5 X'
45	600.82	0.78	W5 Y
46	601.60	-	W5 Y'

Table D.1: Z coordinate of each plane used for spline interpolation on the beam line.

Cycle	Prescaling factor	$\sigma_{M_{\pi\pi}}$ (MeV/c^2)	$N^{0\ n}_{\pi\pi}$	$N^{b.g.\ n}_{\pi\pi}$	$N^{s.\ n}_{\pi\pi}$	$N^{n}_{\pi\pi}$ (10^6)
K	300	1.690	2597	63.5	2533.5	0.760± 0.015
L	300	1.540	3636	69.0	3567.0	1.100± 0.019
	500	2.138	60	1.0	59.0	
M	300	1.294	2379	17.5	2361.5	1.031± 0.019
	500	1.199	651	6.0	645.0	
N	500	1.276	2274	18.5	2255.5	1.128± 0.024
O	500	1.320	3342	29.0	3313.0	1.657± 0.029
P	500	1.247	3784	34.0	3750.0	1.875± 0.031
Q	500	1.267	10009	83.5	9925.5	4.963± 0.050
R	500	1.242	6991	61.0	6930.0	3.465± 0.042
S	500	1.276	7564	66.0	7498.0	3.749± 0.044
T	500	1.243	5074	35.5	5038.5	2.519± 0.036
U	500	1.270	7637	63.0	7574.0	3.787± 0.044
V	500	1.262	8756	77.0	8679.0	4.340± 0.047
W	500	1.271	8392	69.0	8323.0	4.162± 0.046
X	500	1.254	6699	62.0	6637.0	3.319± 0.041
Y	500	1.299	4674	49.0	4625.0	2.985± 0.037
	300	1.277	2263	22.5	2240.5	
PHASE-1		1.296	86782	827.0	85955.0	

Table E.1: Number of the $K^0_L \to \pi^+\pi^-$ events in the fiducial region for each cycle in the PHASE-1

Cycle	Prescaling factor	$\sigma_{M_{\pi\pi}}$ (MeV/c^2)	$N^{0\ n}_{\pi\pi}$	$N^{b.g.\ n}_{\pi\pi}$	$N^{s.\ n}_{\pi\pi}$	$N^{n}_{\pi\pi}$ (10^6)
ZA	250	1.250	8309	62.0	8247.0	2.062± 0.023
ZB	250	1.283	11628	106.0	11522.0	2.881± 0.027
ZC	250	1.265	15154	130.0	15024.0	4.177± 0.034
	500	1.370	849	8.0	841.0	
ZD	250	1.256	15290	138.0	15152.0	4.695± 0.038
	500	1.309	1830	15.5	1814.5	
ZE	500	1.271	11390	105.5	11284.5	5.746± 0.054
	250	1.115	416	2.5	413.5	
ZF	500	1.267	6455	93.0	6362.0	3.347± 0.041
	250	1.367	673	7.5	665.5	
EXTENSION		1.266	71994	668.0	71326.0	
Total		1.285	158776	1495.0	157281.0	63.744

Table E.2: Number of the $K^0_L \to \pi^+\pi^-$ events in the fiducial region for each cycle in the EXTENSION

	$\pi\pi$	$\pi\mu\nu$	$\pi e\nu$
branching ratio (10^{-2})	0.203	27.0	38.7
generated events (10^6)	5.0	525.69	571.03
accepted events	52239	430326	584402
detector acceptance (%)	1.045	0.082	0.102
pulser-run 2.5×10^{12} ppp			
tracked events	40983	209435	230689
tracking efficiency (%)	78.5	48.7	39.5
selected events			
selection criteria	28883	149947	158467
fiducial region	27352	779	438
selection efficiency (%)	66.7	0.372	0.290
absolute acceptance A (%)	0.547	0.00015	0.00008
	± 0.003	± 0.00001	± 0.00001
$A_{\pi\pi}/A$	1.000	0.00027	0.00014
		± 0.00001	± 0.00001
$(470 < M_{\pi\pi} < 485 MeV/c^2)$		872	531
$(510 < M_{\pi\pi} < 525 MeV/c^2)$		232	1018

Table E.3: Results of acceptance calculation from a Monte Carlo simulation for the $K_L^0 \to \pi^+\pi^-$, $K_L^0 \to \pi\mu\nu$, and $K_L^0 \to \pi e\nu$ decays

	$\pi\pi$	$\mu^+\mu^-$	$\mu_L e_R$	$e_L \mu_R$	ee
generated events (10^6)	5.0	5.0	5.0	5.0	5.0
accepted events	52239	43157	46315	46857	43804
detector acceptance (%)	1.045	0.863	0.926	0.937	0.876
pulser-run 2.5×10^{12} ppp					
tracked events	40983	37129	39842	40359	37761
tracking efficiency (%)	78.5	86.0	86.0	86.1	86.2
selected events					
selection criteria	28883	26357	27766	27871	25475
muon momentum $\geq 1.0\, GeV/c$		23456	25765	25846	
fiducial region	27352	23027	25231	25242	24701
selection efficiency (%)	66.7	62.0	63.3	62.5	65.4
absolute acceptance A (%)	0.547	0.461	0.505	0.505	0.494
	± 0.003	± 0.003	± 0.003	± 0.003	± 0.003
$A_{\pi\pi}/A$	1.000	1.188	1.084	1.084	1.107
		± 0.011	± 0.009	± 0.009	± 0.010
δ_M (MeV/c^2)	1.28	1.48	1.61	1.59	1.75

Table E.4: Results of acceptance calculation from a Monte Carlo simulation with accidental hits superposition for two-body kaon decays

	$\pi\pi$	$\mu^+\mu^-$	$\mu_L e_R$	$e_L \mu_R$	ee
generated events (10^6)	5.0	5.0	5.0	5.0	5.0
accepted events	52239	43157	46315	46857	43804
detector acceptance (%)	1.045	0.863	0.926	0.937	0.876
(Monte Carlo data only)					
tracked events	47232	42572	45561	46091	43160
tracking efficiency (%)	90.4	98.6	98.4	98.4	98.5
selected events					
selection criteria	39660	35940	37699	38174	34843
muon momentum $\geq 1.0\,GeV/c$		32230	35065	35523	
fiducial region	37730	31712	34395	34761	33875
selection efficiency (%)	79.9	74.5	75.5	75.4	78.5
absolute acceptance A (%)	0.755	0.634	0.688	0.695	0.678
	$\pm$0.004	$\pm$0.004	$\pm$0.004	$\pm$0.004	$\pm$0.004
$A_{\pi\pi}/A$	1.000	1.190	1.097	1.085	1.114
		$\pm$0.009	$\pm$0.008	$\pm$0.008	$\pm$0.008
δ_M (MeV/c^2)	1.28	1.47	1.61	1.58	1.74

Table E.5: Results of acceptance calculation from a Monte Carlo simulation *without* accidental hits superposition for two-body kaon decays

momentum	PID efficiency			(corrected)	M.C.fraction	product
	N_i	n_i	ε_i	ε_i	$f\{i\}$	$\varepsilon_i \cdot f\{i\}$
(GeV/c^2)					(%)	(%)
1.0-1.1	15	10	.667$\pm$.126	.670$\pm$.127	3.73$\pm$0.13	2.50$\pm$0.48
1.1-1.2	23	18	.783$\pm$.088	.786$\pm$.088	4.67$\pm$0.14	3.67$\pm$0.43
1.2-1.3	72	65	.903$\pm$.035	.907$\pm$.035	5.76$\pm$0.16	5.22$\pm$0.25
1.3-1.4	124	119	.960$\pm$.018	.964$\pm$.018	6.37$\pm$0.17	6.14$\pm$0.20
1.4-1.5	209	190	.909$\pm$.020	.913$\pm$.020	7.03$\pm$0.17	6.42$\pm$0.21
1.5-1.6	287	276	.962$\pm$.011	.966$\pm$.012	7.07$\pm$0.18	6.83$\pm$0.19
1.6-1.7	386	351	.909$\pm$.015	.914$\pm$.015	6.82$\pm$0.17	6.23$\pm$0.19
1.7-1.8	426	399	.937$\pm$.012	.941$\pm$.012	6.81$\pm$0.17	6.41$\pm$0.18
1.8-1.9	476	447	.939$\pm$.011	.944$\pm$.011	6.21$\pm$0.16	5.86$\pm$0.17
1.9-2.0	500	468	.936$\pm$.011	.941$\pm$.011	5.68$\pm$0.16	5.34$\pm$0.16
2.0-2.1	528	493	.934$\pm$.011	.938$\pm$.011	5.26$\pm$0.15	4.93$\pm$0.15
2.1-2.3	1032	955	.925$\pm$.008	.930$\pm$.009	9.06$\pm$0.20	8.43$\pm$0.20
2.3-2.5	857	818	.954$\pm$.007	.959$\pm$.008	6.76$\pm$0.17	6.48$\pm$0.17
2.5-3.0	1356	1247	.920$\pm$.007	.924$\pm$.008	11.41$\pm$0.22	10.54$\pm$0.22
3.0-3.5	461	424	.920$\pm$.013	.924$\pm$.013	5.03$\pm$0.15	4.65$\pm$0.15
3.5-4.0	107	97	.907$\pm$.028	.911$\pm$.028	1.84$\pm$0.09	1.68$\pm$0.10
4.0-4.5	17	17	1.000$\pm$.058	1.000$\pm$.059	0.48$\pm$0.05	0.48$\pm$0.06
total	6876	6394	0.930$\pm$.003			91.85$\pm$0.73

Table E.6: muon identification efficiency in ZD cycle.

momentum	PID efficiency			$(\pi \to \mu)$	M.C.fraction	product
	N_i	n_i	ε_i	$\Delta\varepsilon_i$	$f\{i\}$	$(1-\varepsilon_i)\cdot f\{i\}$
(GeV/c^2)					(%)	(%)
0.5-1.0	1984	0	.0000±.0005	.0000±.0000	9.78±0.19	9.78±0.19
1.0-1.1	1768	40	.0226±.0035	.0116±.0025	5.89±0.15	5.72±0.15
1.1-1.2	2428	121	.0498±.0044	.0178±.0035	6.14±0.15	5.94±0.15
1.2-1.3	3136	173	.0552±.0041	.0137±.0028	6.84±0.16	6.56±0.16
1.3-1.4	3470	240	.0692±.0043	.0206±.0032	6.83±0.16	6.50±0.15
1.4-1.5	3767	270	.0717±.0042	.0183±.0030	6.51±0.15	6.16±0.15
1.5-1.6	3759	280	.0745±.0043	.0232±.0032	6.64±0.16	6.29±0.15
1.6-1.7	3814	308	.0808±.0044	.0211±.0031	6.38±0.15	6.00±0.15
1.7-1.8	3590	171	.0476±.0036	.0201±.0032	5.85±0.15	5.70±0.14
1.8-1.9	3368	146	.0433±.0035	.0182±.0031	5.49±0.14	5.35±0.14
1.9-2.0	3170	126	.0397±.0035	.0202±.0034	4.80±0.13	4.71±0.13
2.0-2.1	2930	131	.0447±.0038	.0205±.0035	4.13±0.12	4.01±0.12
2.1-2.3	5161	252	.0488±.0030	.0197±.0026	7.32±0.15	7.11±0.16
2.3-2.5	4033	182	.0451±.0033	.0151±.0026	5.48±0.14	5.32±0.14
2.5-3.0	6764	228	.0337±.0022	.0156±.0020	7.78±0.17	7.64±0.17
3.0-3.5	3229	79	.0245±.0027	.0065±.0019	3.08±0.11	3.02±0.10
3.5-4.0	1362	32	.0235±.0041	.0043±.0025	0.96±0.06	0.94±0.06
4.0-4.5	468	15	.0321±.0082	.0074±.0052	0.22±0.03	0.22±0.03
total	58201	2794	0.0480±.0009			96.97±0.60

Table E.7: Efficiency of the pion to be misidentified as an muon in ZD cycle.

		Left arm			Right arm		
detector	efficiency	N_i	n_i	ε_i (%)	N_i	n_i	ε_i (%)
muon identifier	ε_{μ}^{MU}	6876	6394	92.99±0.31	6801	6198	91.13±0.34
	$\varepsilon_{\mu\to PION}^{MU}$	5634	37	0.657±0.108	5476	37	0.676±0.111
	$\varepsilon_{\pi\to\mu}^{MU}$	58201	2794	4.801±0.089	59903	2859	4.773±0.087
	ε_{PION}^{MU}	39153	35282	90.11±0.15	39283	35320	89.91±0.015
	$\varepsilon_{e\to\mu}^{MU}$	17407	31	0.178±0.032	17577	45	0.256±0.038
Čerenkov counter	$\varepsilon_{\mu\to e}^{CH}$	6694	15	0.224±0.051	6608	17	0.257±0.062
	$\varepsilon_{\pi\to e}^{CH}$	53642	51	0.095±0.013	53982	106	0.196±0.019
	ε_{e}^{CH}	18553	17407	93.82±0.17	19310	17577	91.03±0.21
shower counter	$\varepsilon_{\mu\to\pi}^{EM}$	6752	87	1.289±0.137	6688	124	1.854±0.165
	$\varepsilon_{\pi\to e}^{EM}$	58201	4610	7.921±0.112	59903	6027	10.061±0.123
	ε_{e}^{EM}	17808	17281	97.04±0.13	17982	17312	96.3±0.14

Table E.8: Overall efficiencies of each counter using the selected samples in ZD cycle

	Left arm			Right arm		
Cycle	$\epsilon_{\mu}^{MU\,L}$	$\epsilon_{e}^{CH\,L}$	$\epsilon_{e}^{EM\,L}$	$\epsilon_{\mu}^{MU\,R}$	$\epsilon_{e}^{CH\,R}$	$\epsilon_{e}^{EM\,R}$
K	.892±.039	.734±.016	.928±.006	.881±.023	.751±.015	.931±.006
L	.929±.019	.674±.017	.922±.005	.920±.037	.753±.015	.930±.005
M	.892±.041	.941±.015	.894±.006	.851±.040	.899±.014	.894±.006
N	.891±.019	.928±.016	.917±.006	.848±.038	.904±.017	.920±.006
O	.849±.040	.934±.011	.918±.005	.862±.023	.901±.024	.928±.004
P	.904±.015	.930±.011	.912±.005	.900±.016	.894±.014	.919±.004
Q	.907±.008	.937±.010	.912±.003	.895±.009	.909±.004	.935±.002
R	.918±.009	.943±.006	.915±.003	.925±.011	.914±.018	.945±.003
S	.874±.013	.936±.005	.911±.003	.876±.009	.904±.006	.931±.003
T	.903±.012	.926±.012	.918±.004	.882±.014	.892±.012	.937±.003
U	.870±.012	.942±.008	.925±.003	.873±.011	.901±.009	.934±.003
V	.880±.009	.936±.016	.916±.003	.882±.009	.908±.006	.934±.003
W	.870±.009	.929±.010	.911±.003	.877±.010	.915±.012	.930±.003
X	.855±.010	.923±.005	.902±.003	.873±.011	.908±.006	.929±.003
Y	.867±.011	.933±.007	.908±.003	.908±.011	.904±.006	.920±.003
ZA	.931±.015	.954±.010	.970±.002	.911±.010	.915±.015	.961±.002
ZB	.926±.011	.950±.004	.976±.002	.920±.008	.907±.008	.969±.002
ZC	.924±.007	.943±.010	.967±.002	.899±.007	.906±.004	.963±.002
ZD	.919±.007	.938±.003	.967±.001	.910±.006	.902±.005	.960±.002
ZE	.906±.009	.937±.004	.967±.002	.895±.007	.882±.011	.961±.002
ZF	.893±.011	.943±.005	.965±.002	.885±.011	.905±.012	.940±.003
average	.895±.004	.930±.003	.933±.003	.892±.004	.899±.003	.941±.003

Table E.9: The particle identification efficiencies for each cycle

Cycle	$N_{\pi\pi}^{n}$ (10^6)	$\epsilon_{\mu\mu}^{n}$	$\epsilon_{\mu e}^{n}$	ϵ_{ee}^{n}	$\epsilon_{\pi\pi}^{n}$	$C_{\pi\pi/\mu\mu}$
K	0.760±.015	.757±.037	.596±.028	.472±.015	.930±.007	1.023±.007
L	1.100±.019	.826±.038	.599±.025	.422±.015	.944±.006	1.024±.008
M	1.031±.019	.718±.043	.685±.039	.665±.019	.938±.006	1.029±.014
N	1.128±.024	.714±.035	.704±.030	.697±.021	.938±.007	1.017±.010
O	1.657±.029	.715±.035	.708±.033	.710±.025	.940±.006	1.010±.002
P	1.875±.031	.776±.020	.733±.018	.692±.017	.932±.006	1.019±.009
Q	4.963±.050	.771±.011	.745±.010	.719±.011	.934±.006	1.021±.008
R	3.465±.042	.815±.014	.777±.015	.740±.018	.939±.006	1.012±.003
S	3.749±.044	.723±.014	.715±.012	.712±.008	.933±.006	1.030±.006
T	2.519±.036	.753±.016	.729±.016	.701±.016	.936±.006	1.017±.005
U	3.787±.044	.722±.014	.721±.013	.726±.012	.938±.006	1.016±.002
V	4.340±.047	.730±.011	.725±.012	.723±.016	.937±.006	1.018±.004
W	4.162±.046	.723±.012	.716±.012	.714±.015	.936±.006	1.015±.001
X	3.319±.041	.710±.013	.701±.011	.696±.008	.935±.006	1.019±.003
Y	2.985±.037	.745±.013	.722±.011	.699±.009	.937±.006	1.018±.003
ZA	2.062±.023	.823±.016	.815±.017	.809±.019	.942±.006	1.007±.002
ZB	2.881±.027	.823±.013	.816±.012	.811±.010	.943±.006	1.007±.002
ZC	4.177±.034	.800±.010	.794±.010	.790±.012	.939±.006	1.0
ZD	4.695±.038	.806±.009	.793±.009	.780±.007	.938±.006	1.0
ZE	5.746±.054	.779±.011	.768±.011	.763±.013	.937±.006	1.0
ZF	3.347±.041	.762±.014	.765±.014	.770±.013	.937±.006	1.0
average		.763±.004	.744±.004	.730±.004	.937±.003	1.013±.003

Table E.10: The event identification efficiencies and the correction factor of the dead-time difference for each cycle

Cycle	$N_{\pi\pi}^{\ n}$ (10^6)	$N_{\mu\mu}^{0\ n}$	$N_{\mu\mu}^{b.g.\ n}$	$\epsilon_{\pi\pi}^{n}\, C_{\pi\pi/\mu\mu}^{n} / \epsilon_{\mu\mu}^{n}$	$(N_{\mu\mu}^{0\,n} / N_{\pi\pi}^{n}) \times (\epsilon_{\pi\pi}^{n}\, C_{\pi\pi/\mu\mu}^{n} / \epsilon_{\mu\mu}^{n})$ (10^{-6})
K	0.760±.015	5	0	1.257±.063	8.27±3.70
L	1.100±.019	2	0	1.170±.055	2.13±1.50
M	1.031±.019	1	0	1.344±.083	1.30±1.30
N	1.128±.024	3	0	1.335±.067	3.55±2.05
O	1.657±.029	8	0	1.328±.066	6.41±2.27
P	1.875±.031	4	0	1.223±.034	2.61±1.31
Q	4.963±.050	13	2	1.237±.022	3.24±0.90
R	3.465±.042	9	0	1.167±.021	3.03±1.01
S	3.749±.044	7	0	1.330±.028	2.48±0.94
T	2.519±.036	6	0	1.265±.029	3.01±1.23
U	3.787±.044	9	1	1.319±.026	3.14±1.05
V	4.340±.047	12	1	1.307±.022	3.61±1.04
W	4.162±.046	16	0	1.313±.023	5.05±1.26
X	3.319±.041	9	0	1.342±.026	3.64±1.21
Y	2.985±.037	7	0	1.280±.025	3.00±1.13
ZA	2.062±.023	7	0	1.152±.024	3.91±1.48
ZB	2.881±.027	10	0	1.154±.019	4.01±1.27
ZC	4.177±.034	15	0	1.174±.016	4.22±1.09
ZD	4.695±.038	13	0	1.163±.015	3.22±0.89
ZE	5.746±.054	14	0	1.204±.018	2.93±0.78
ZF	3.347±.041	9	1	1.229±.024	3.31±1.10
Total	63.744	179	5	1.243±.009	3.49±0.26

Table E.11: Number of the $K_L^0 \to \mu^+\mu^-$ events in the fiducial region and the ratio with respect to the number of $K_L^0 \to \pi^+\pi^-$ events and correction factors for each cycle

Factor	Value (Uncertainty)		
	$K_L^0 \to \mu^+\mu^-$	$K_L^0 \to \mu e$	$K_L^0 \to ee$
$N_{\pi\pi}$	$(6.374\pm.062) \times 10^7$ (1.0%)		
$A_{\pi\pi} / A$	1.192±.018 (1.5%)	1.065±.010 (0.9%)	1.064±0.010 (0.9%)
$\overline{\frac{\epsilon_{\pi\pi}}{\epsilon}} \cdot \overline{C^{d.t.}}$	1.243±.009 (0.7%)	1.274±.008 (0.6%)	1.300±.007 (0.5%)
$1 - \epsilon_{\pi\pi\to\times}^{N.I.}$	0.943±.006 (0.6%)		
B.R.($K_L^0 \to \pi^+\pi^-$)	$(2.03\pm0.04) \times 10^{-3}$ (2.0%)		
sensitivity (10^{-11})	4.45±0.18	4.08±0.12	4.16±0.13
N	177.8±13.4±1.2	< 2.3	< 3.9
Branching Ratio	$(7.9\pm0.6\pm\ 0.3) \times 10^{-9}$	$< 9.4 \times 10^{-11}$	$< 1.6 \times 10^{-11}$

Table E.12: Tabulation of the factors used for the calculation of the sensitivities and the branching ratios

muon identifier	○	○	×	○	○
Čerenkov	○	×	○	○	×
shower counter	○	×	○	×	○
$N^0_{\mu\mu}$	179	215	185	190	179
$N^{b.g.}_{\mu\mu}$	5	39	11	7	5
$N_{\mu\mu}$	177.8	190.6	180.8	187.9	177.8
$\epsilon_{\mu\mu}$	0.763±.006	0.799±.006	0.790±.006	0.796±.006	0.766±.006
$N_{\mu\mu}/\epsilon_{\mu\mu}$	233.0	238.6	228.9	236.1	232.2
$B.R.(K^0_L \to \mu^+\mu^-)$ (10^{-9})	7.9±0.6	8.1±0.6	7.7±0.6	8.0±0.6	7.9±0.6

Table E.13: Tabulation of the results of the branching ratio calculation for different muon identification processes

Figure Captions

Fig. 1.1 Leading diagrams for the $K^0_L \to \mu^+\mu^-$ decay. (a) Diagram involving the exchange of two photons. (b) Z^0 exchange diagrams. (c) W box diagram.

Fig. 2.1 Plan view of the East Counter Hall of the KEK-PS.

Fig. 2.2 Vertical view of the beam line.

Fig. 2.3 Schematic view of the KEK E137 detector system.

Fig. 2.4 Cell structure of the drift chamber. The black circles are sense wires and the open circles are field wires.

Fig. 2.5 Distribution of $Dsum \times 1/\sqrt{2}$ of the (a)W2L and (b)W4L. *Dsum* is defined in Section 4.1. The root mean-squared of this distribution was regarded as the intrinsic spatial resolution of the chamber.

Fig. 2.6 Schematic view of the (a)H1 and (b)H2 hodoscope.

Fig. 2.7 Description of the requirement for parallel coincidence.

Fig. 2.8 Description of the requirement for semi-parallel coincidence.

Fig. 2.9 Block diagram of the hodoscope signals. " L " stands for the signal from the counter in the left arm.

Fig. 2.10 Distribution of the meantime of the (a) H1L and (b) H2L hodoscope. For H1 the meantime was calculated from the average of the H1-U TDC and H1-D TDC, while the H2 meantime was calculated from the meantimer TDC.

Fig. 2.11 Schematic view of the gas Čerenkov counter.

Fig. 2.12 Block diagram of the Čerenkov counter signals.

Fig. 2.13 Schematic view of the electromagnetic shower counter.

Fig. 2.14 Block diagram of the shower counter signals.

Fig. 2.15 Schematic view of the muon identifier.

Fig. 2.16 Block diagram of the muon identifier signals.

Fig. 3.1 Logic diagram of the trigger.

Fig. 3.2 Block diagram of the online data-taking system.

Fig. 3.3 Block diagram of the time sequence of the data acquisition.

Fig. 3.4 K_L^0 momentum spectrum calculated from Sanford-Wang's formula. The solid line is the spectrum taken at $0\,deg$, and the dashed line is the spectrum taken at $3\,deg$.

Fig. 3.5 K_L^0 momentum spectrum calculated from the method to extrapolate the production data at 300 GeV protons using Feynman scaling. The unit of the vertical axis is arbitrary. The solid line is the spectrum taken at $0\,deg$, and the dotted line is the spectrum taken at $2\,deg$.

Fig. 4.1 Description of the algorithm of the Y-view track finding. Details are described in Appendix B.

Fig. 4.2 Description of the algorithm of the X-view track finding. Details are described in Appendix B.

Fig. 4.3 Definition of the collinearity angle θ.

Fig. 4.4 Four left-right ambiguity solutions for the staggered-hit wires.

Fig. 4.5 Hit wire search around the staggered-hit wires. When two wires {A,B} (surrounded by a circle) were hit, other two combinations of wires, {A,C} and {B,D}, were examined.

Fig. 4.6 Hit wire search around the single-hit wire. when a wire E (surrounded by a circle) was hit, other three wires in the direction of the track, F, G, and H (surrounded by the dotted circle) , were examined.

Fig. 4.7 Staggered-hit wires search around the single-hit wire. When a selected single wire was changed from E, staggered-hit wires of the following combination(s) were examined : F $\Longleftrightarrow$ {F,G} , G $\Longleftrightarrow$ {F,G} and {G,H} , H $\Longleftrightarrow$ {G,H} .

Fig. 4.8 Momentum distributions of the muons whose last plane in the muon identifier were MU2(solid line), MU3(dotted line), and MU4(dotdashed line). The arrows in the figure indicate the momentum range for muon identification.

Fig. 4.9 Distribution of the energy-momentum ratio, E/P, for muons (left side) and electrons (right side). The arrows in the figure indicates the cuts on E/p.

Fig. 4.10 Scatter plot between the momentum measured in the spectrometer, p, and the energy in the shower counter, E, for the electron sample.

Fig. 4.11 Scatter plot between p and E for the muon sample.

Fig. 4.12 Distribution of the probability of the track χ^2 for the left arm.

For all the figures in Section 4.4., the histogram with the solid line represent the distribution of real $K_L^0 \to \pi^+\pi^-$ events, and the open squares represent the distribution of Monte Carlo $K_L^0 \to \pi^+\pi^-$ events. The arrow in the figure indicates the cut. The distributions are normalized to contain the same numbers of events in the range of the cut imposed by the criteria.

Fig. 4.13 Distributions of the reduced track χ^2 for the left arm in the (a) linear scale, and (b) semi-Log scale.

Fig. 4.14 Distribution of UD for the left arm.

Fig. 4.15 Distributions of the track momentum for the (a)left and (b)right arms.

Fig. 4.16 Distribution of the momentum balance PB.

Fig. 4.17 Distribution of the reconstructed kaon momentum, p_K.

Fig. 4.18 Distributions of p_K in the (a)PHASE-1 and (b)EXTENSION.

Fig. 4.19 Distribution of the vertex distance, *Dist*.

Fig. 4.20 Distribution of the Z coordinate of the vertex point, V_Z.

Fig. 4.21 Distribution of the direction angle squared, θ_V^2, between the beam line and the line which connected the vertex point and the target.

Fig. 4.22 Distribution of the X coordinate of the track at the exit of the decay chamber for the left arm.

Fig. 4.23 Distribution of the X coordinate of the track at the entrance to the upstream magnet for the left arm.

Fig. 4.24 Distribution of the Y coordinate of the track at the exit of the downstream magnet for the left arm.

Fig. 4.25 Scatter plot of the invariant mass ($M_{\pi\pi}$) vs the collinearity angle squared (θ^2) for 10^3 $K_L^0 \to \pi^+\pi^-$ events.

Fig. 4.26 Distribution of the $M_{\pi\pi}$ with $\theta^2 < 3(mrad)^2$ for all the $K_L^0 \to \pi^+\pi^-$ events. The solid curve is the distribution obtained from the Monte Carlo $K_L^0 \to \pi^+\pi^-$ events, which is normalized to contain the same number of events in the fiducial region. It is the same for Fig. 4.27.

Fig. 4.27 Distribution of the θ^2 with $493\,MeV/c^2 < M_{\pi\pi} < 502\,MeV/c^2$ for all the $K_L^0 \to \pi^+\pi^-$ events.

Fig. 4.28 Scatter plot of the invariant mass ($M_{\mu\mu}$) vs θ^2 for the $K_L^0 \to \mu^+\mu^-$ events. The box indicates the boundary of the fiducial region.

Fig. 4.29 Distribution of the $M_{\mu\mu}$ with $\theta^2 < 3\,(mrad)^2$ for the $K_L^0 \to \mu^+\mu^-$ events. The solid curve is the distribution obtained from the Monte Carlo $K_L^0 \to \mu^+\mu^-$ events, which is normalized to contain the same number of events in the fiducial region. It is the same for Fig. 4.30.

Fig. 4.30 Distribution of the θ^2 with $493\,MeV/c^2 < M_{\mu\mu} < 502\,MeV/c^2$ for the $K_L^0 \to \mu^+\mu^-$ events.

Fig. 4.31 Scatter plot of the invariant mass ($M_{\mu e}$) vs θ^2 for the $K_L^0 \to \mu e$ events. The box indicates the boundary of the fiducial region.

Fig. 4.32 Scatter plot of the invariant mass (M_{ee}) vs θ^2 for the $K_L^0 \to ee$ events. The box indicates the boundary of the fiducial region.

Fig. 4.33 Scatter plot of M_{ee} vs the K_L^0 transverse momentum with respect to the target-to-vertex direction, p_t, for the $K_L^0 \to ee$ events.

Fig. 4.34 Scatter plot of M_{ee} vs p_t of the background events expected from a Monte Carlo calculation for $K_L^0 \to ee$ events at ten times the sensitivity of this experiment; contributions from the decays $K_L^0 \to \pi e\nu$ $(\cdot)$, $K_L^0 \to ee\gamma$ $(+)$, and $K_L^0 \to eeee$ $(circ)$.

Fig. 5.1 Distribution of the $M_{\pi\pi}$ with $\theta^2 < 3(mrad)^2$ for all the $K_L^0 \to \pi^+\pi^-$ events in the semi-log scale. The histogram is data, and the plots with error bar are from the Monte Carlo $K_L^0 \to \pi^+\pi^-$ events.

Fig. 5.2 Distribution of the θ^2 with $493\,MeV/c^2 < M_{\pi\pi} < 502\,MeV/c^2$ for all the $K_L^0 \to \pi^+\pi^-$ events in the semi-log scale.

Fig. 5.3 Distribution of the proper time for all the $K_L^0 \to \pi^+\pi^-$ events in the semi-log scale.

Fig. 5.4 Distribution of the $M_{\pi\pi}$ with $\theta^2 < 3(mrad)^2$ for all the $K_L^0 \to \pi^+\pi^-$ events in the semi-log scale. The plots with error bar are from the Monte Carlo $K_L^0 \to \pi^+\pi^-$ and $K_L^0 \to \pi^+\pi^-\gamma$ events. Details of this figure are described in Appendix D.

Fig. 5.5 Distribution of the $M_{\pi\pi}$ with $\theta^2 < 3(mrad)^2$ for the minimum bias $K_L^0 \to \pi^+\pi^-$ events (prescaling factor= 500) in the semi-log scale.

Fig. 5.6 (a)$M_{\pi\pi}$ distributions of the background for the minimum bias events estimated from the Monte Carlo $K_L^0 \to \pi\mu\nu$ and $K_L^0 \to \pi e\nu$ events, (b)contribution from the $K_L^0 \to \pi\mu\nu$ events, and (c)contribution from the $K_L^0 \to \pi e\nu$ events. They are shown by the plots with error bar.

Fig. 5.7 (a) Tracking efficiencies of the $K_L^0 \to \pi^+\pi^-$ events for various beam intensities. Points with error bars are the numbers of $K_L^0 \to \pi^+\pi^-$ events per 10^{12} ppp from the real data (arbitrary unit), and the solid line represents the results from the Monte Carlo simulation, which were normalized to the data, with accidental hits superposition using the pulser-run events under various conditions. (dotted line : Monte Carlo data only, and dashed line : accidental hits superposition only for the hodoscopes.) (b) The numbers of $K_L^0 \to \pi^+\pi^-$ events obtained in a beam pulse of 0.5 *second*. They were calculated by the product of the above tracking efficiency and the beam intensity.

Fig. 5.8 Momentum dependence of the muon ID efficiency in the muon identifier using the muon sample in the (a) left and (b) right arm.

Fig. 5.9 (a) Momentum dependence of the efficiency of pions misidentified as muons in the muon identifier in the left arm. (b) Momentum dependence of the pion decay effect on the efficiency of pions misidentified as muons in the muon identifier in the left arm.

Fig. 5.10 Momentum dependence of the electron ID efficiency in the shower counter in the left arm.

Fig. 5.11 Position dependence of the electron ID efficiency in the Čerenkov counter in the left arm.

Fig. 5.12 Momentum dependence of the nuclear interaction loss in the left arm : (a) results from the special run data, and (b) from the FLUKA simulation.

Fig. 5.13 Scatter plot of the invariant mass ($M_{\mu\mu}$) vs θ^2 for the Monte Carlo $K_L^0 \to \pi\mu\nu$ events with the pion decaying in flight into a muon *before* the spectrometer.

Fig. 5.14 Scatter plot of the invariant mass ($M_{\mu\mu}$) vs θ^2 for the Monte Carlo $K_L^0 \to \pi\mu\nu$ events with the pion decaying *after* the spectrometer or being misidentified as a muon.

Fig. 5.15 Scatter plot of the invariant mass ($M_{\mu\mu}$) vs θ^2 for the Monte Carlo $K_L^0 \to \pi\mu\nu$ events with the pion decaying *in* the spectrometer.

Fig. 5.16 Scatter plot of the invariant mass ($M_{\mu\mu}$) vs θ^2 for the Monte Carlo $K_L^0 \to \pi e\nu$ events with the pion decaying after the spectrometer or being misidentified as a muon.

Fig. 5.17 Scatter plot of the invariant mass ($M_{\mu\mu}$) vs θ^2 for the Monte Carlo $K_L^0 \to \pi e\nu$ events with the pion decaying before or in the spectrometer.

Fig. 5.18 Distribution of the θ^2 with $493\,MeV/c^2 < M_{\mu\mu} < 502\,MeV/c^2$ for the Monte Carlo $K_L^0 \to \pi e\nu$ events with the pion decaying after the spectrometer or being misidentified as a muon.

Fig. 5.19 Distribution of the θ^2 with $493\,MeV/c^2 < M_{\mu\mu} < 502\,MeV/c^2$ for the Monte Carlo $K_L^0 \to \pi e\nu$ events with the pion decaying before or in the spectrometer.

Fig. 5.20 Distribution of the $M_{\mu\mu}$ with $\theta^2 < 3\,(mrad)^2$ for the $K_L^0 \to \mu^+\mu^-$ events in the semi-log scale. (a)The plots with error bar are from the Monte Carlo $K_L^0 \to \pi\mu\nu$ events, which are normalized to the sensitivity of this experiment. (b) Squares are from the events with the pion decaying in flight into a muon *before* the spectrometer, diamonds are from the events with the pion decaying *after* the spectrometer or being misidentified as a muon, and stars are from the events with the pion decaying *in* the spectrometer.

Fig. 5.21 Scatter plot of the invariant mass ($M_{\mu\mu}$) vs θ^2 for the $K_L^0 \to \mu^+\mu^-$ events in the PHASE-1.

Fig. 5.22 Scatter plot of the invariant mass ($M_{\mu\mu}$) vs θ^2 for the $K_L^0 \to \mu^+\mu^-$ events in the EXTENSION.

Fig. 5.23 Distribution of the dependence of DR on χ^2. DR is normalized to the value when $\chi^2 = 4.0$.

Fig. 5.24 Distribution of the dependence of the double ratio DR on $Dist$. DR is normalized to the value when $Dist = 1.5\,cm$.

Fig. 5.25 Distribution of the dependence of DR on UD. DR is normalized to the value when $UD = 0.06$.

Fig. 5.26 Distribution of the dependence of the double ratio of the muon and pion tracks $DR_{L\,arm}$ on UD. DR is normalized to the value when $UD = 0.20$.

Fig. 5.27 The experimental results of the $K_L^0 \to \mu^+\mu^-$ branching ratio of all the experiments until now. The horizontal lines show the unitarity limit (solid line : mean value, dotted lines : allowed values from the error of the branching ratio of $K_L^0 \to \gamma\gamma$ decay).

Fig. 5.28 (a) The $K_L^0 \to \mu^+\mu^-$ branching ratio (10^{-9}) in each cycle, where the cycle K (ZF) corresponds to the cycle number of 10 (30), and the $K_L^0 \to \mu^+\mu^-$ branching ratio (10^{-9}) as a function of (b) kaon momentum, (c) vertex point, and (d) X coordinate of the track at th exit of the decay chamber.

Fig. 5.29 The $K_L^0 \to \mu^+\mu^-$ branching ratio (10^{-9}) in each cycle of (a)PHASE-1 and (b)EXTENSION, as a function of proton beam intensity.

Fig. 5.30 Magnetic field dependence of the acceptance. $B = 1.0$ corresponds to the nominal field strength.

Fig. 5.31 $K_L^0 \to \pi^+\pi^-$ track angle distribution of $K_L^0 \to \pi^+\pi^-$ events using the H2 information for different magnetic fields. The histograms are Monte Carlo results and the bars are the experimental data. The horizontal bars at the bottom indicate H2 scintillators. The scintillator labeled "n" in the one that corresponds to the H1 counters and satisfy the parallel trigger condition.

Fig. 6.1 Allowed regions in the ρ-η parameter space (hatched region) for m_t of 100, 140, 180, and 250 GeV/c^2 and $f_B = 130 \pm 40\,MeV$. The vertical lines show the lower bounds on ρ from the $K_L^0 \to \mu^+\mu^-$ branching ratio.

Fig. 6.2 Allowed regions in the ρ-η parameter space for m_t of 100, 140, 180, and 250 GeV/c^2 and $f_B = 250 \pm 50\,MeV$.

Fig. 6.3 2γ diagrams, based on the vector meson dominance model, with one photon on-shell and the other photon off-shell : (a) $K_L^0 \to \pi, \eta, \eta'$ followed by $\pi, \eta, \eta' \to \gamma\gamma^*$, and (b) $K_L^0 \to K^*\gamma$ followed by $K^* \to \rho, \omega, \phi$ and $\rho, \omega, \phi \to \gamma^*$.

Fig. 6.4 Allowed range for M_t as a function of $\Delta B.R.$, where $-0.30 < \rho < 0.38$ is assumed.

Fig. 6.5 Diagrams for the $K^+ \to \pi^+\nu\bar{\nu}$ decay. (a) Z^0 exchange diagrams, and (b) W box diagram.

Fig. A.1 K_L^0 momentum spectrum (solid line) used for the Monte Carlo simulation : (a) spectrum weighted with the decay probability in the 10 m decay chamber, and (b) generation spectrum in the target. The dotted line is the spectrum calculated from Sanford-Wang's formula (Fig. 3.4), and the squares represent the spectrum calculated from the extrapolation method described in Section 3.3. (Fig. 3.5).

Fig. A.2 Non-Gaussian distribution used for the simulation of multiple scattering. This figure is taken from Marion and Zimmerman [61].

Fig. A.3 The error matrix elements (upper matrix) and the weight matrix elements (lower matrix) for an X-view of the left arm when the momentum is equal to 1.0 GeV/c^2. The 1st column(raw) corresponds to W1LX, the 2nd one corresponds to W1LX', ... , and the 10th one corresponds to W5LX'.

Fig. A.4 Diagrams for the $K_L^0 \to \pi^+\pi^-\gamma$ decay : (a) inner bremsstrahlung, and (b) direct emission.

Fig. A.5 The energy spectrum of photons from $K_L^0 \to \pi^+\pi^-\gamma$ decay in the rest frame (plain histogram). The dotdashed histogram is the contribution from inner bremsstrahlung, and the dotted histogram is the contribution from direct emission.

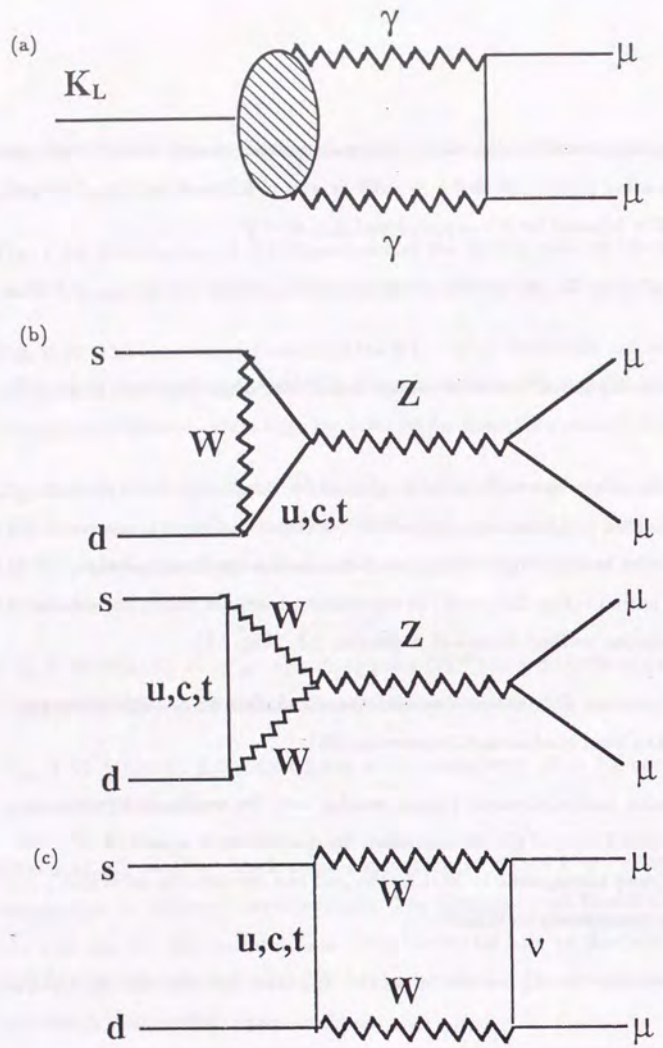

Fig. 1.1

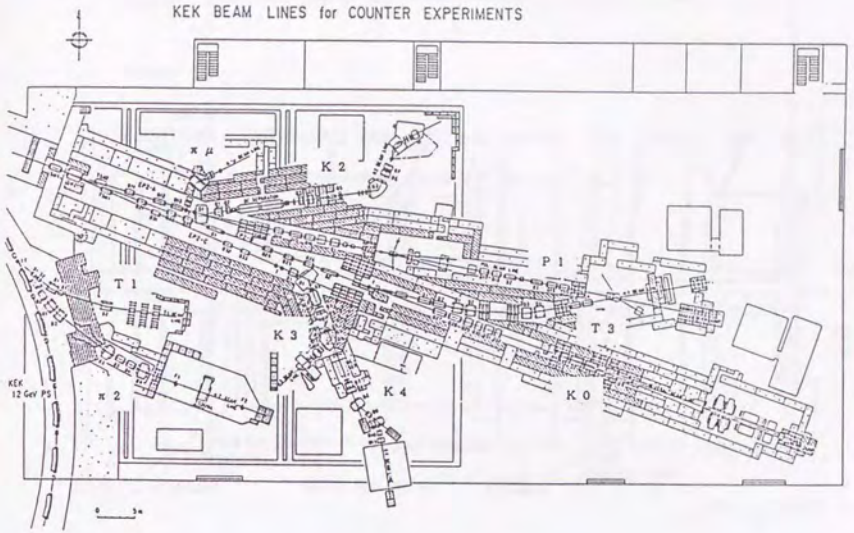

Fig. 2.1

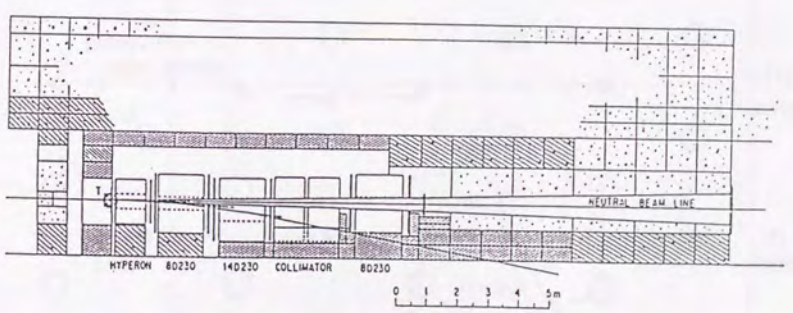

Fig. 2.2

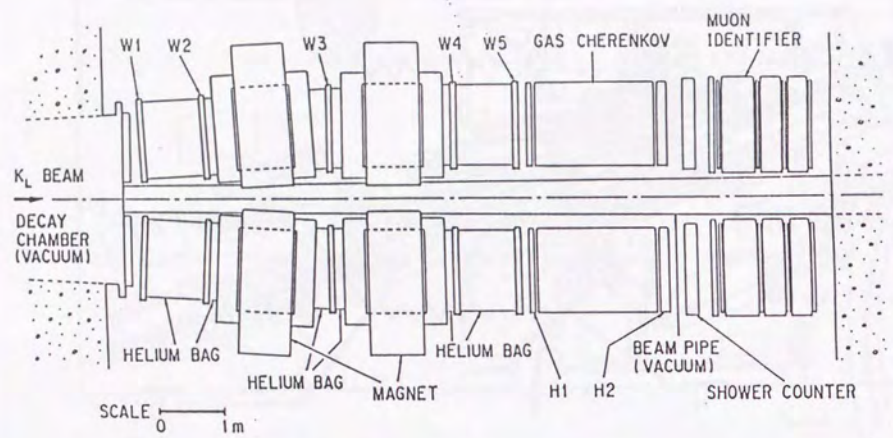

Fig. 2.3

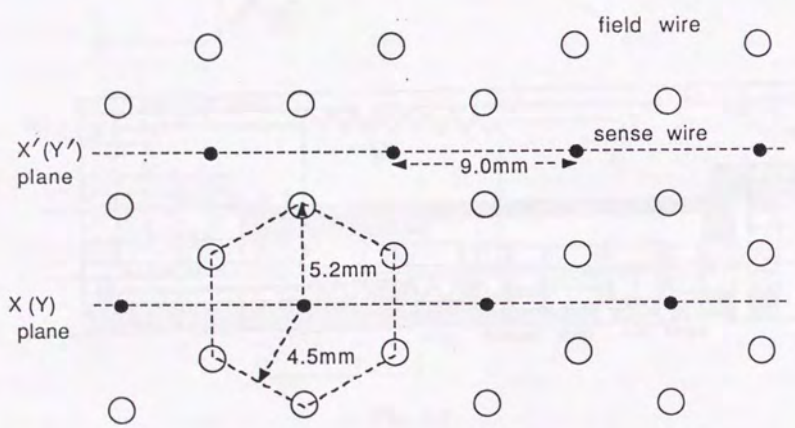

Fig. 2.4

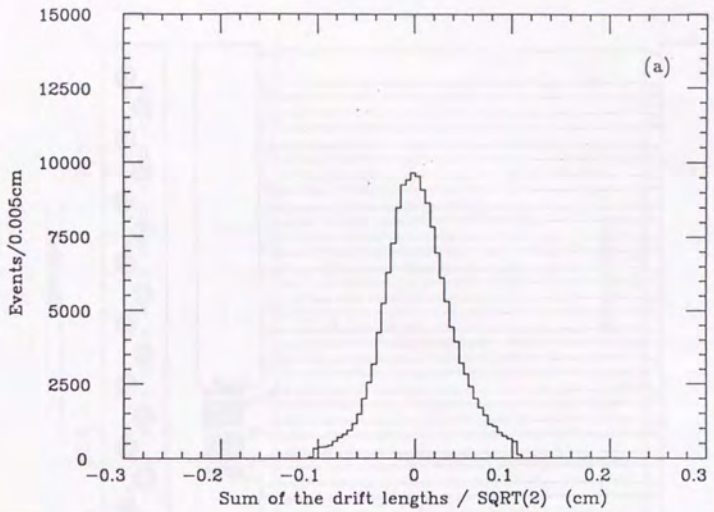

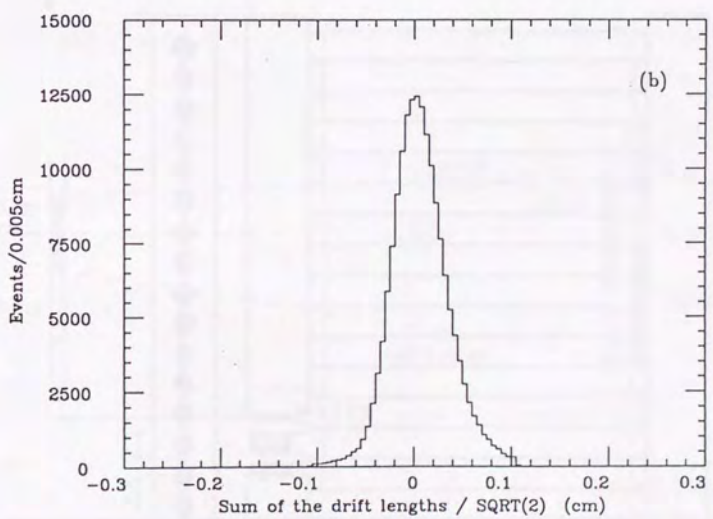

Fig. 2.5

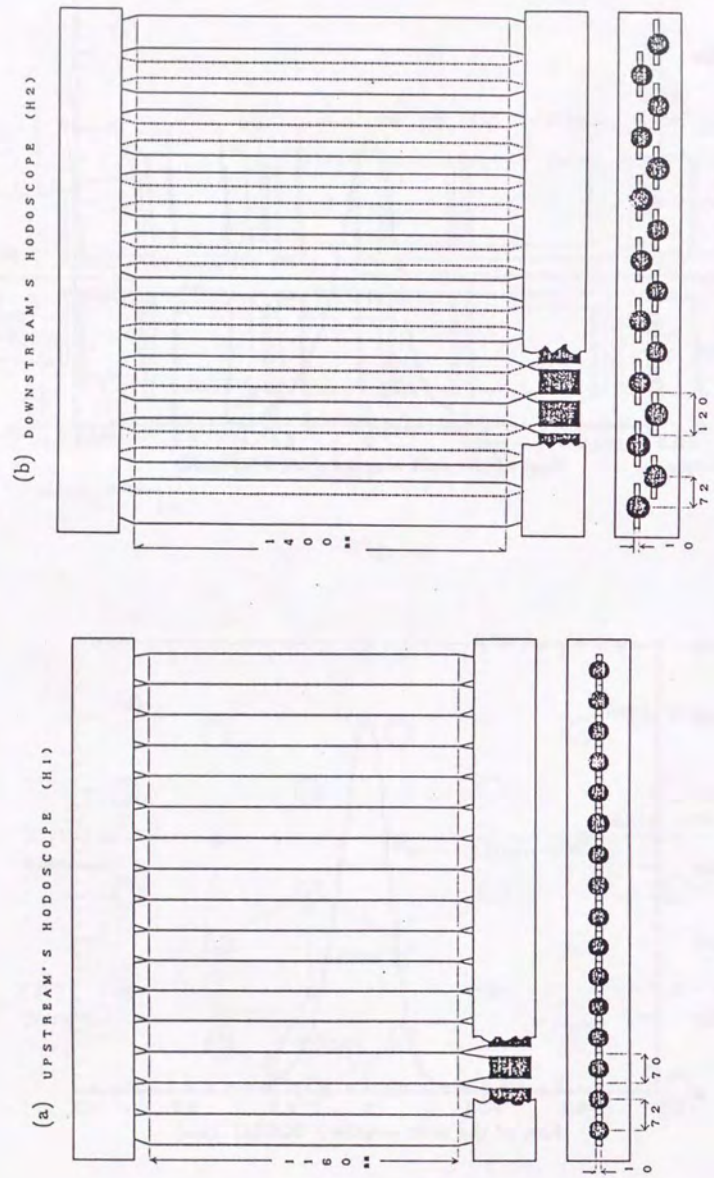

Fig. 2.6

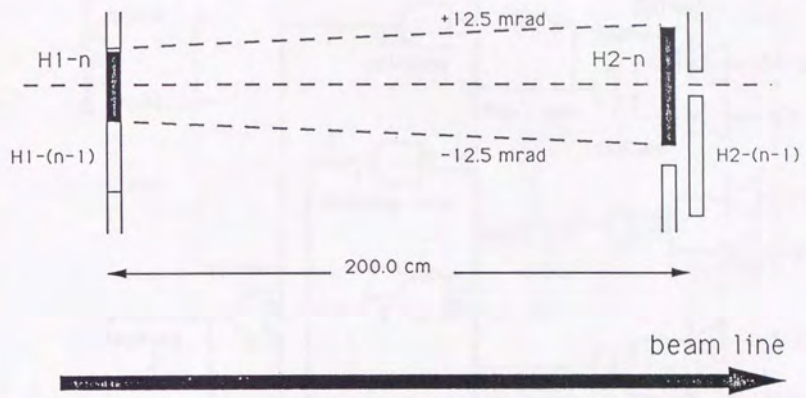

Fig. 2.7

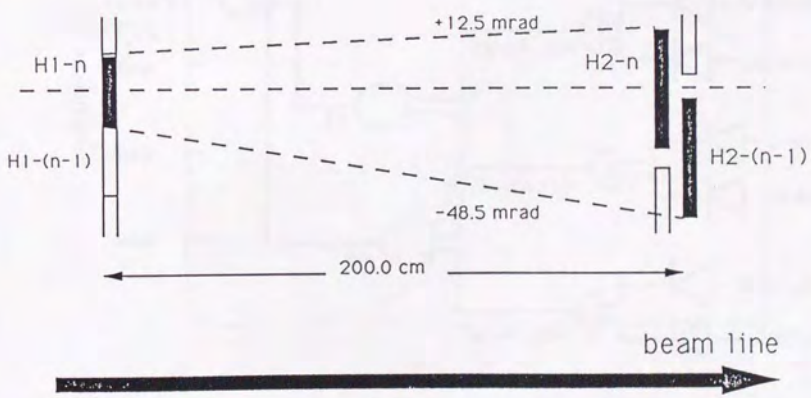

Fig. 2.8

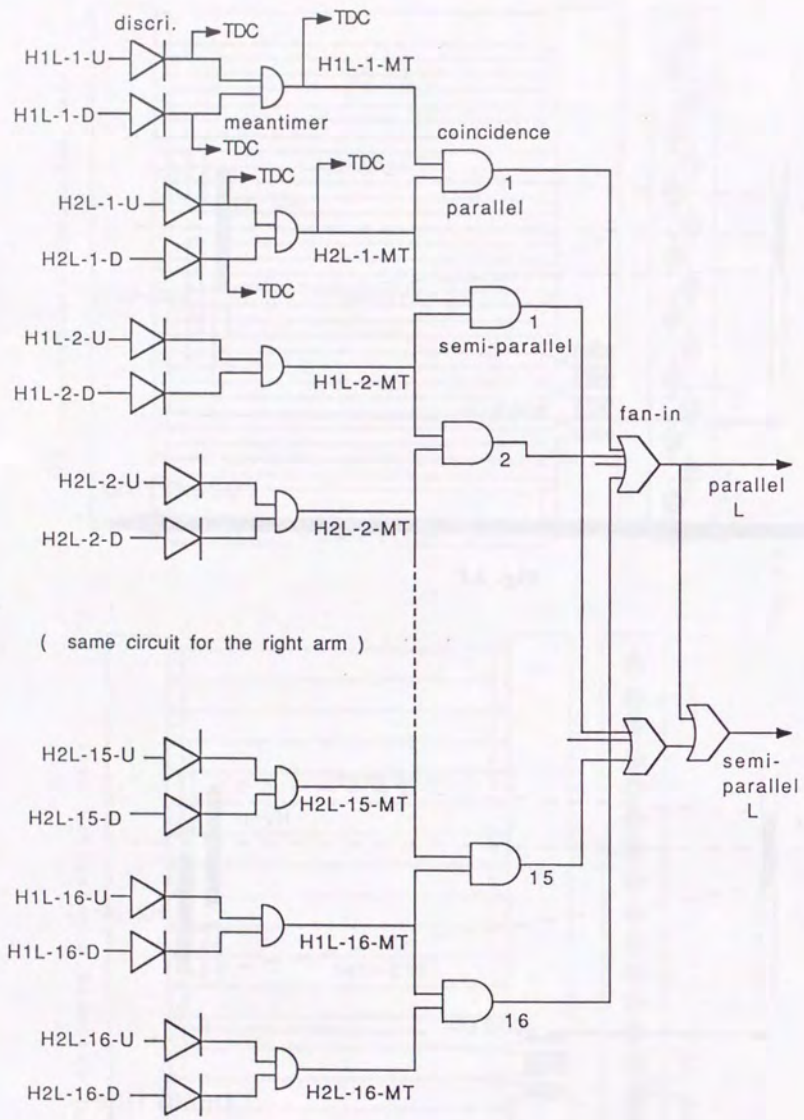

Fig. 2.9

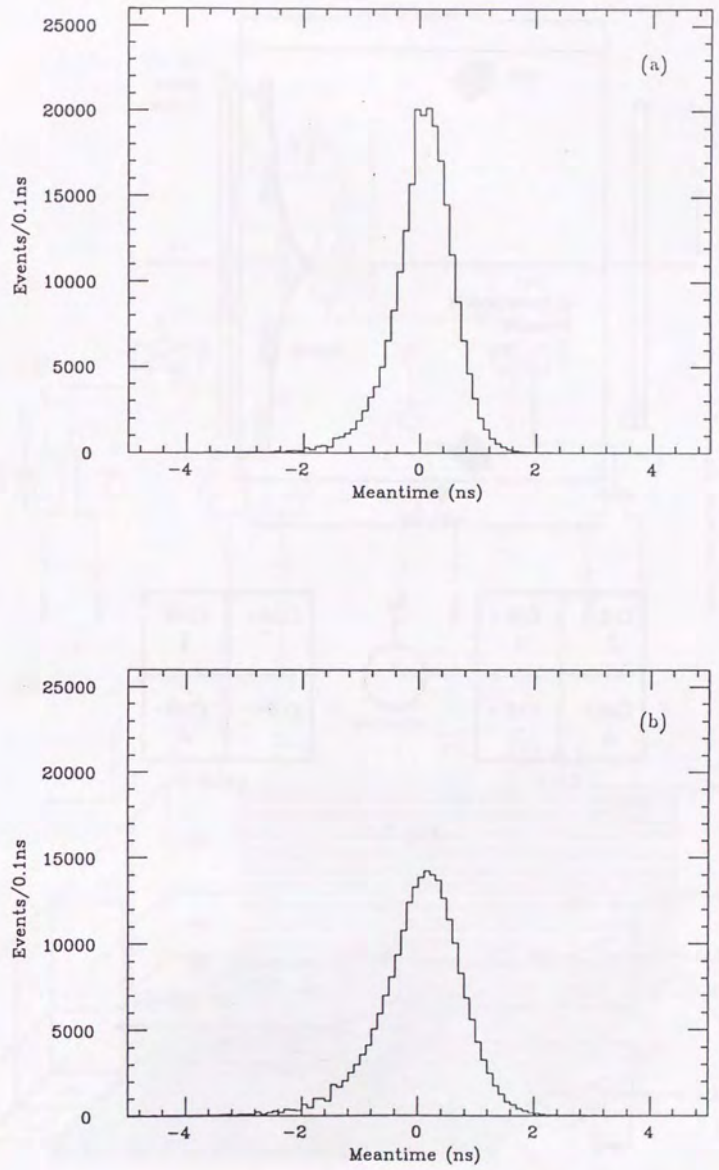

Fig. 2.10

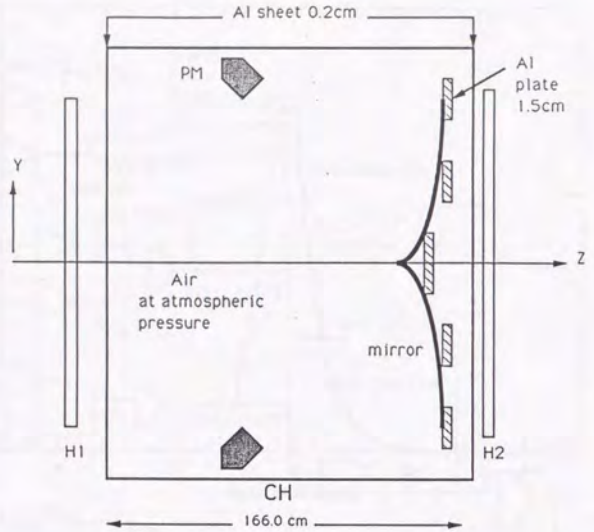

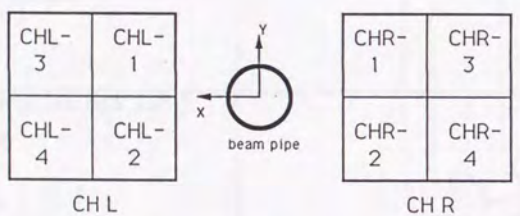

Fig. 2.11

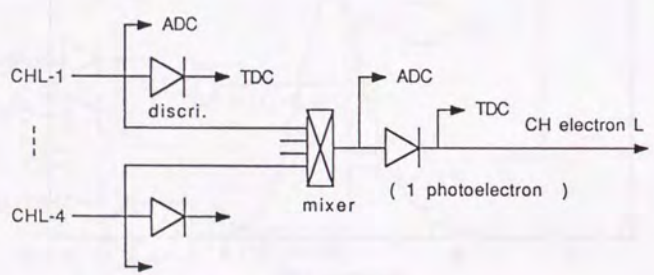

(same circuit for the right arm)

Fig. 2.12

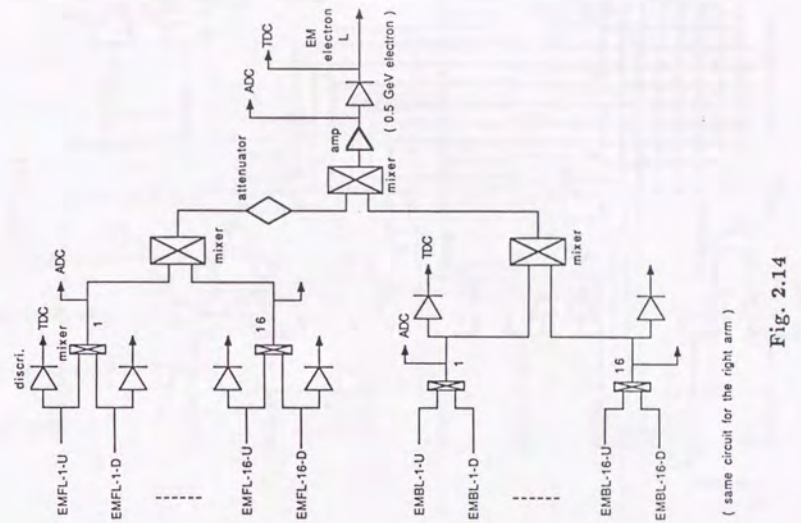

Fig. 2.14

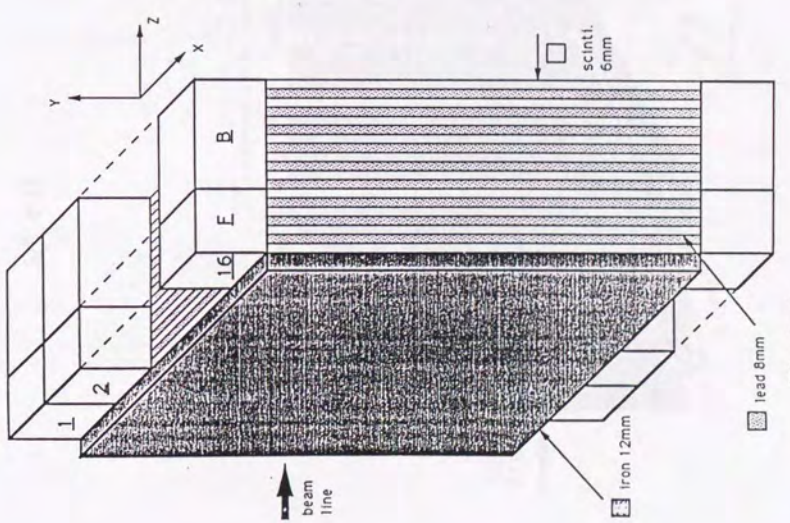

Fig. 2.13

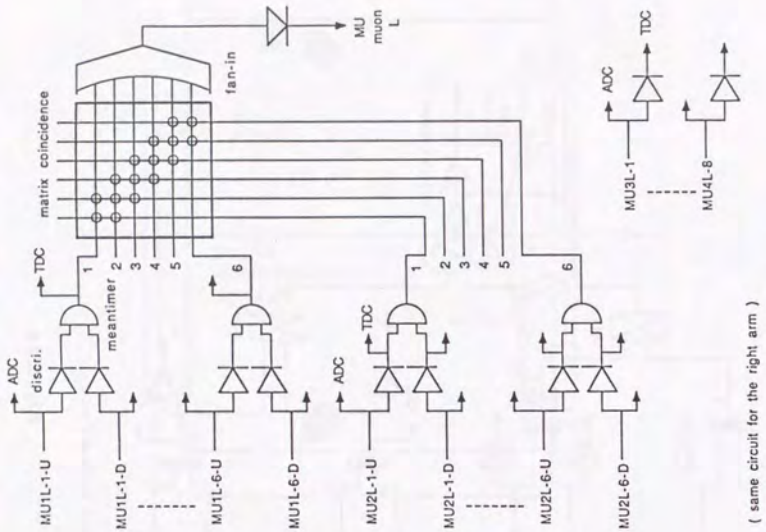

Fig. 2.16

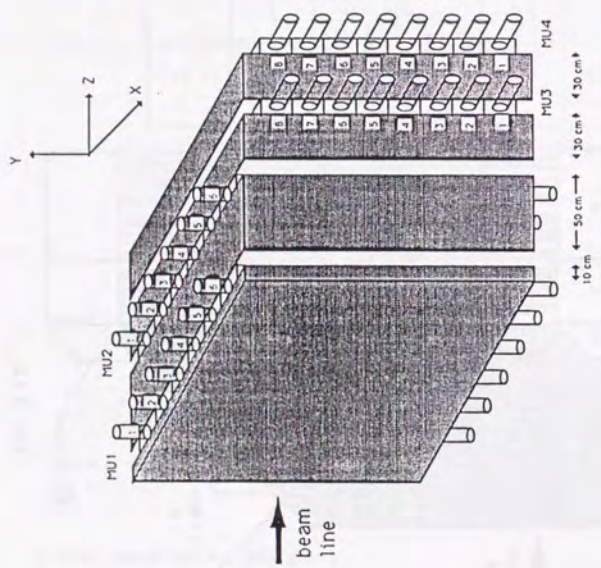

Fig. 2.15

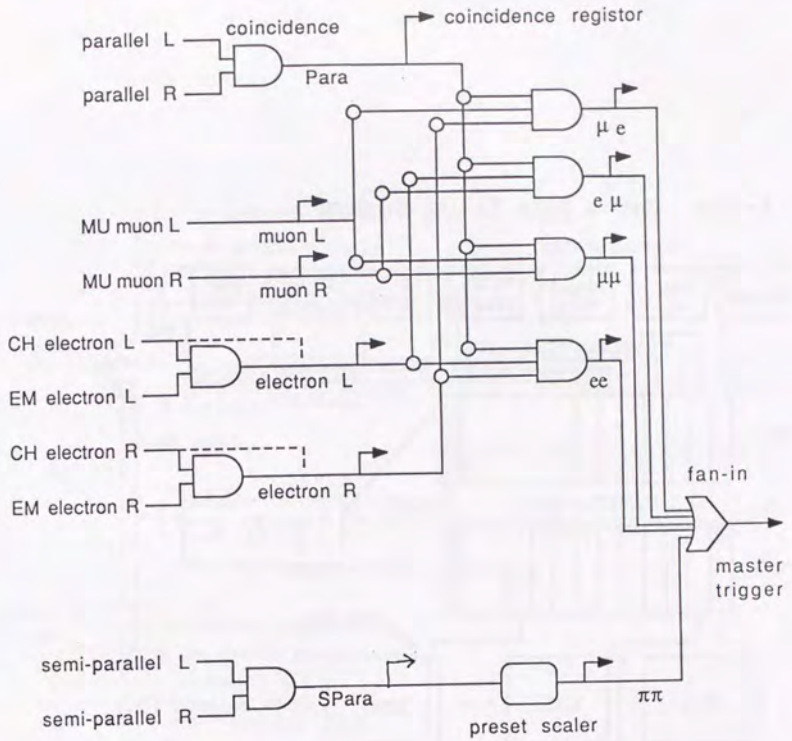

Fig. 3.1

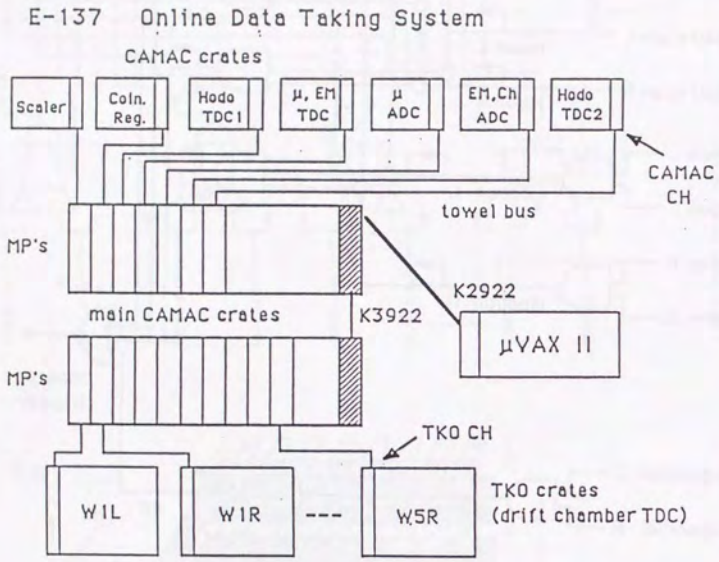
E-137 Online Data Taking System
CAMAC crates
Scaler
Coin. Reg.
Hodo TDC1
μ, EM TDC
μ ADC
EM,Ch ADC
Hodo TDC2
CAMAC CH
towel bus
MP's
main CAMAC crates
K3922
K2922
μVAX II
MP's
TKO CH
W1L
W1R

W5R
TKO crates
(drift chamber TDC)

Fig. 3.2

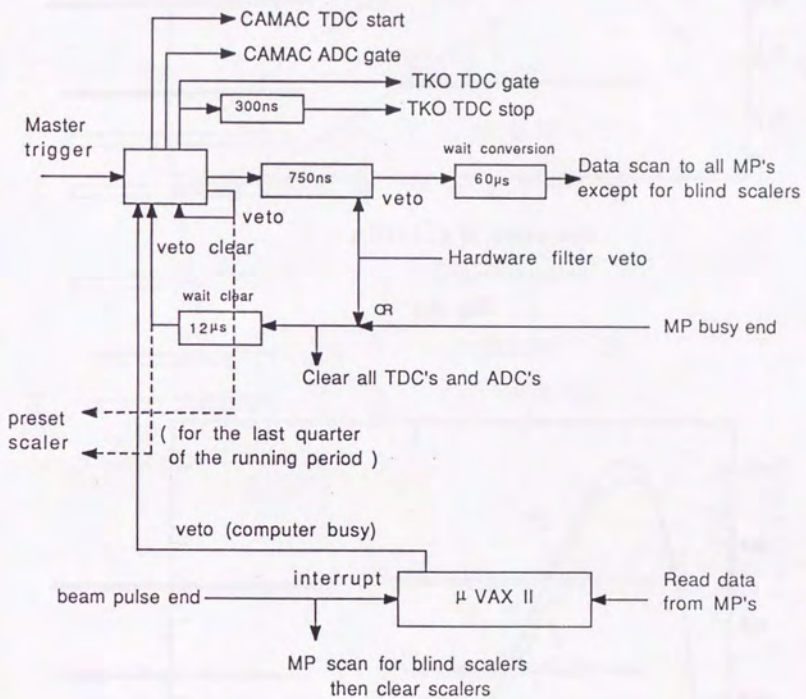
CAMAC TDC start
CAMAC ADC gate
TKO TDC gate
300ns
TKO TDC stop
Master trigger
wait conversion
750ns
veto
60μs
Data scan to all MP's except for blind scalers
veto
veto clear
Hardware filter veto
wait clear
OR
12μs
MP busy end
Clear all TDC's and ADC's
preset scaler
(for the last quarter of the running period)
veto (computer busy)
interrupt
beam pulse end
μ VAX II
Read data from MP's
MP scan for blind scalers
then clear scalers

Fig. 3.3

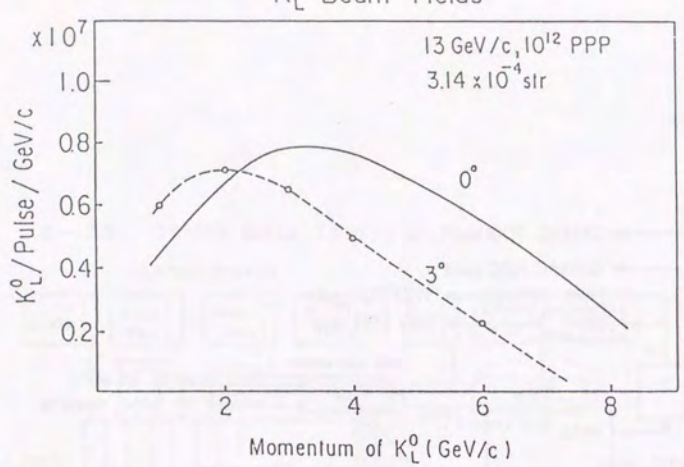

Fig. 3.4

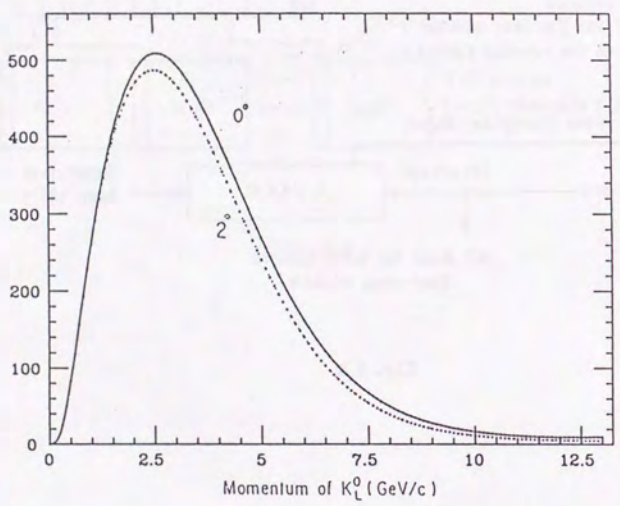

Fig. 3.5

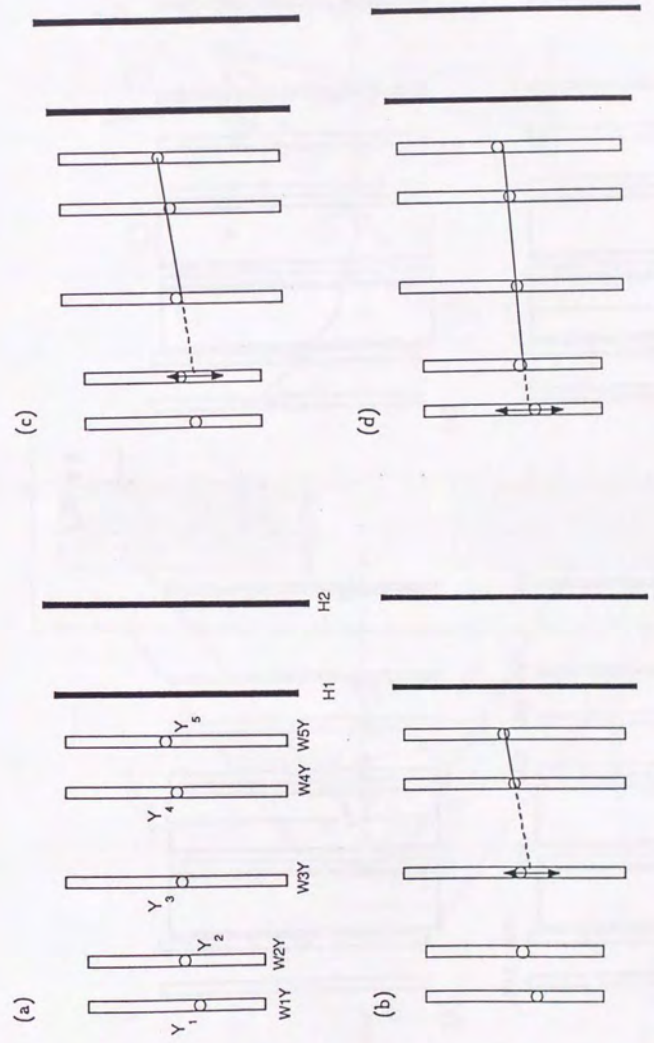

Fig. 4.1

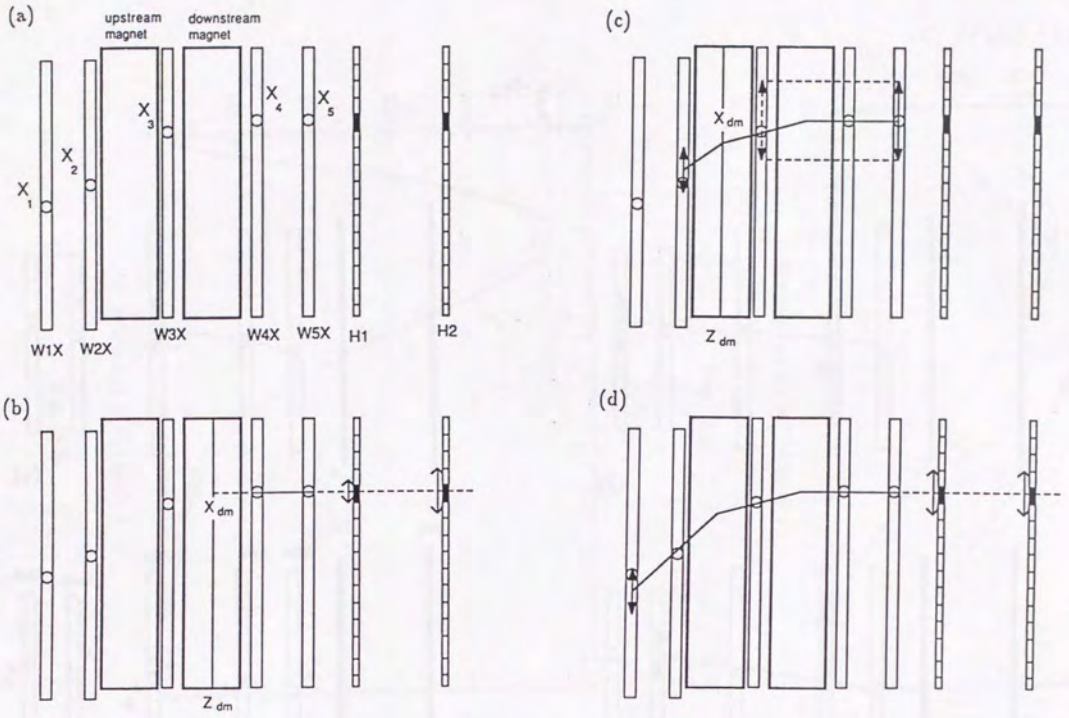

Fig. 4.2

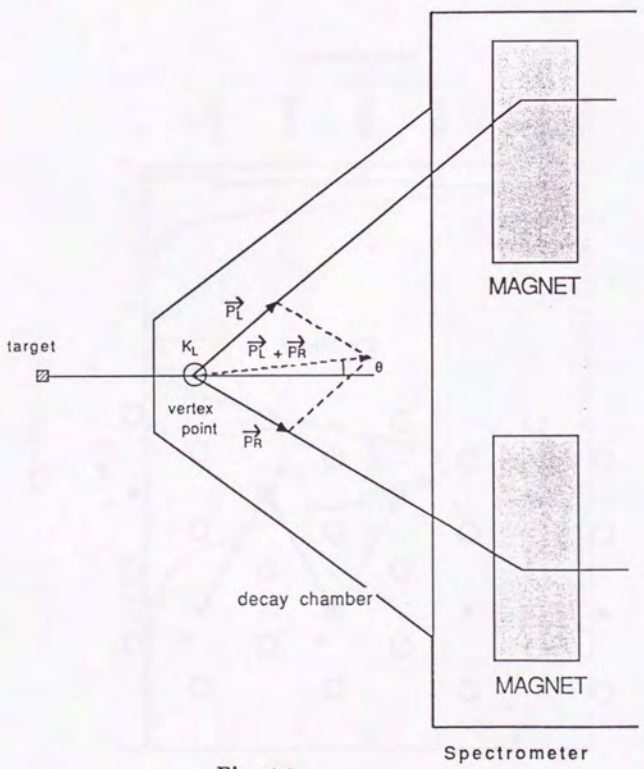

Fig. 4.3

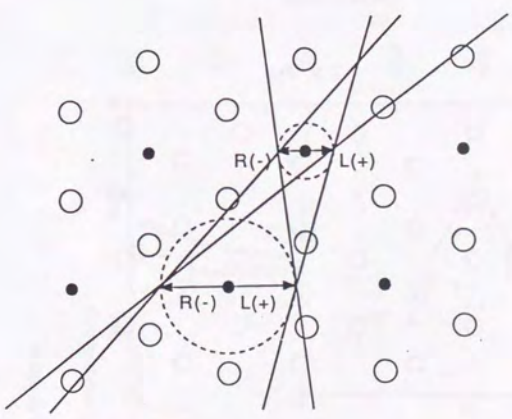

Fig. 4.4

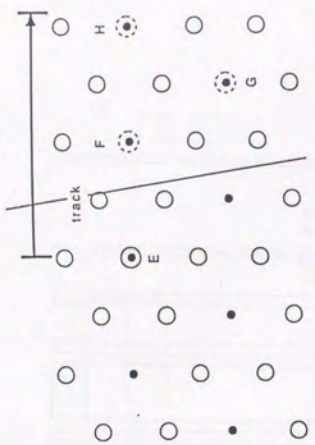

Fig. 4.6

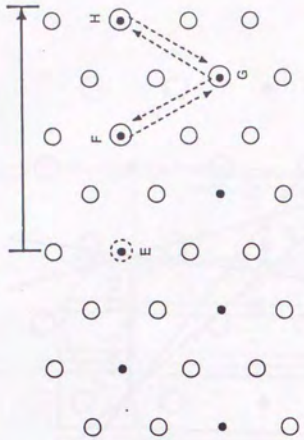

Fig. 4.7

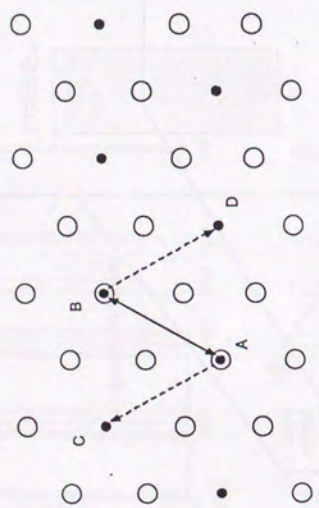

Fig. 4.5

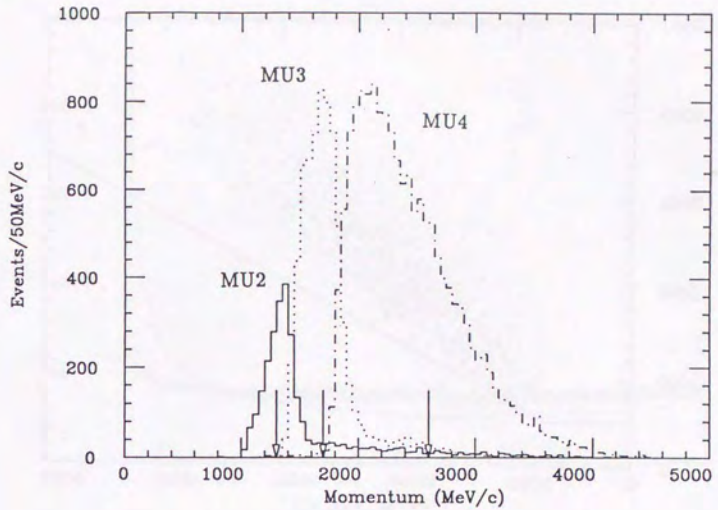

Fig. 4.8

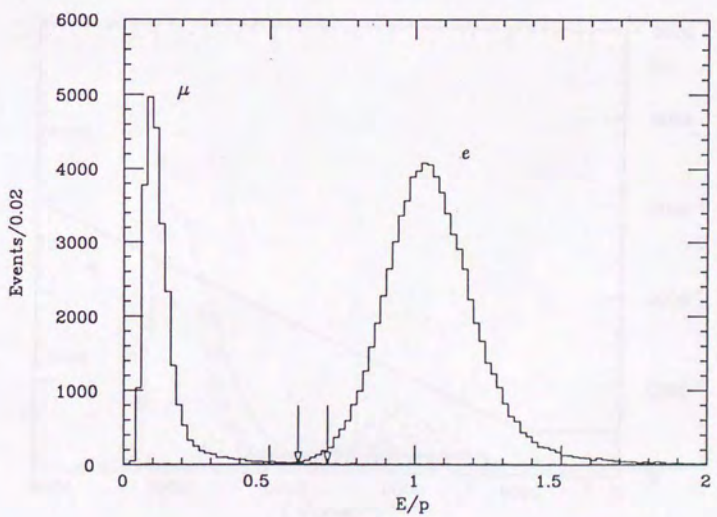

Fig. 4.9

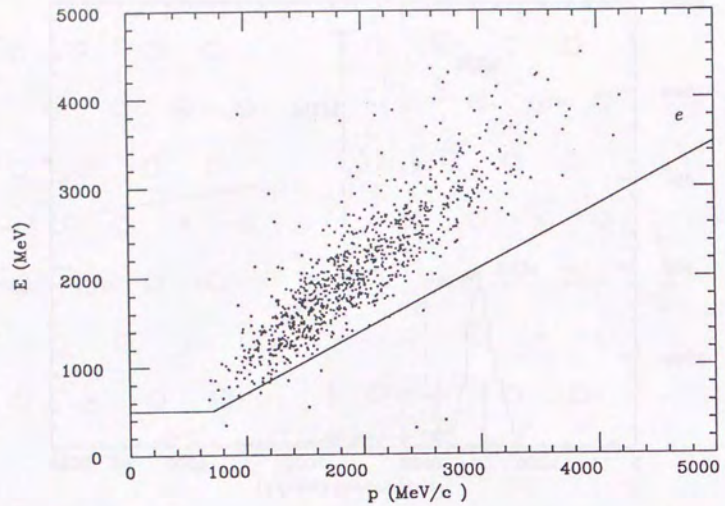

Fig. 4.10

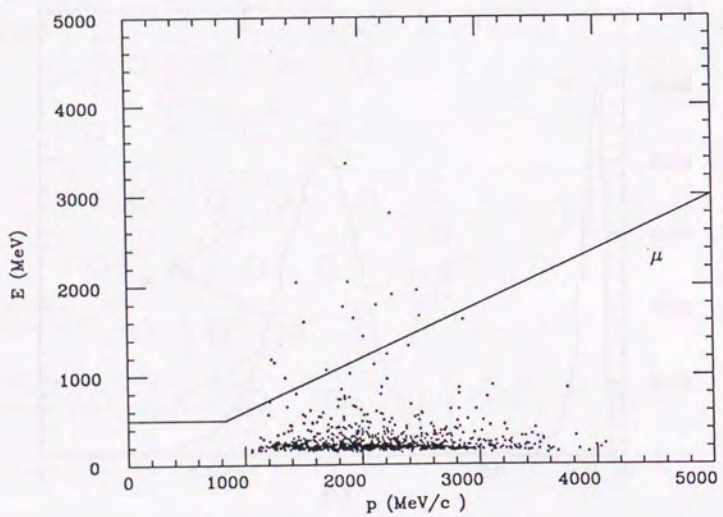

Fig. 4.11

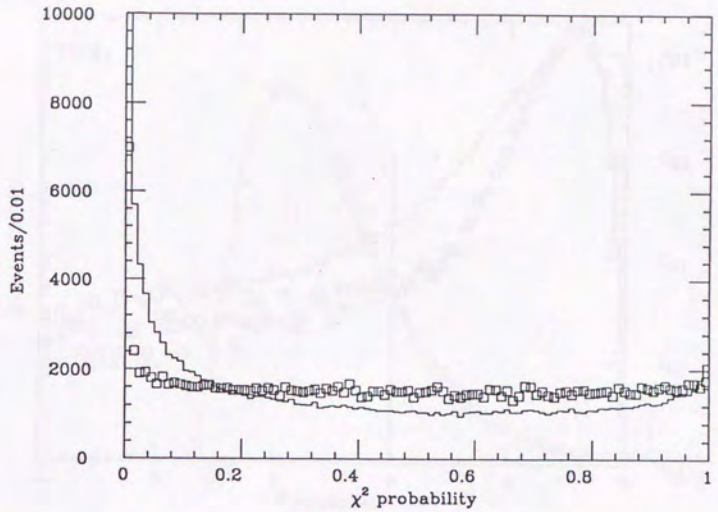

Fig. 4.12

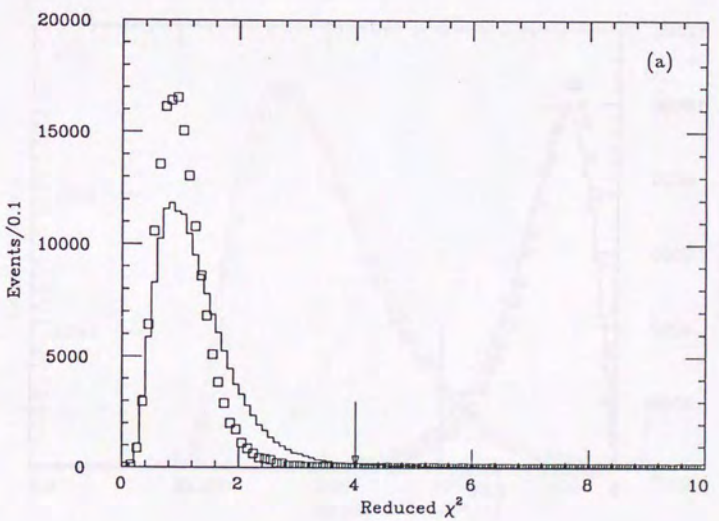

Fig. 4.13

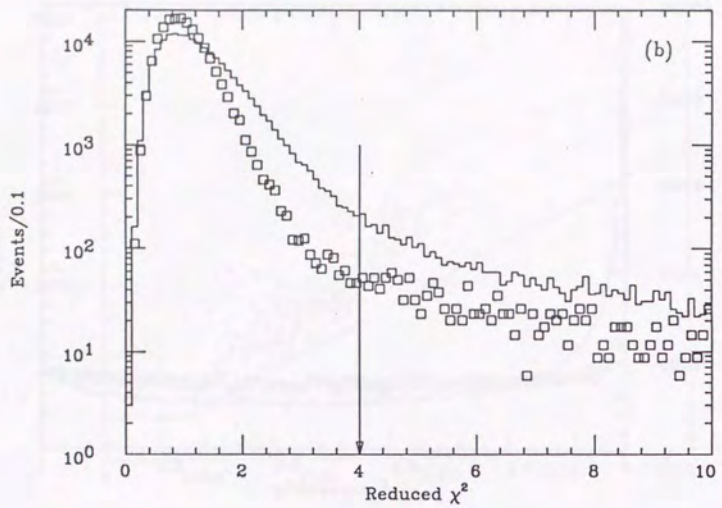

Fig. 4.13

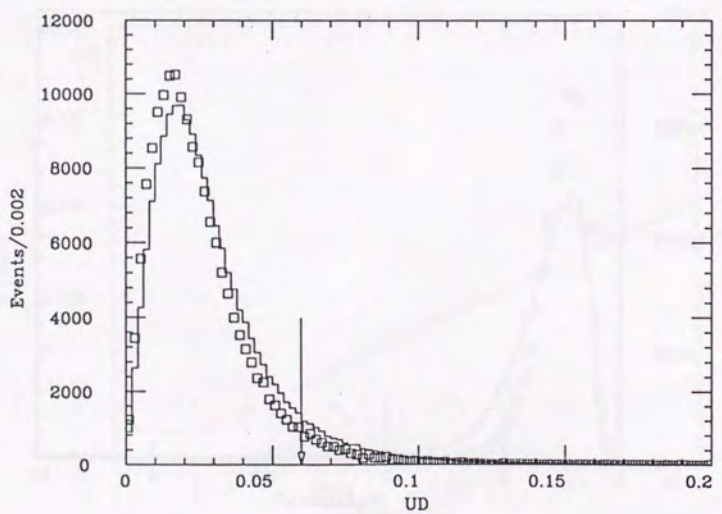

Fig. 4.14

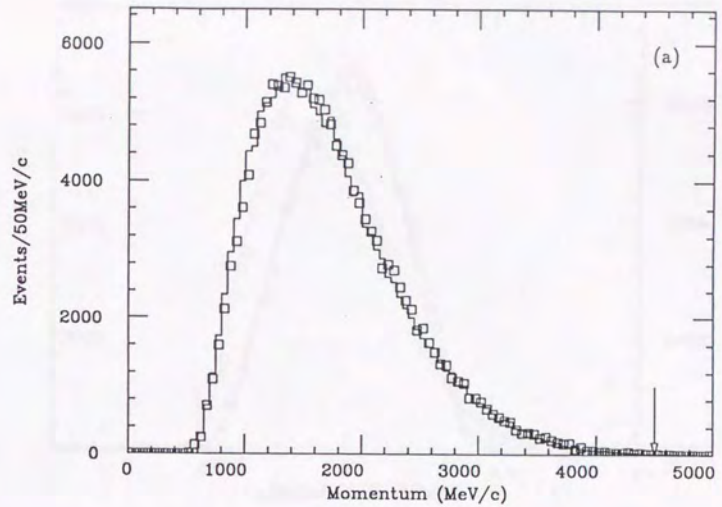

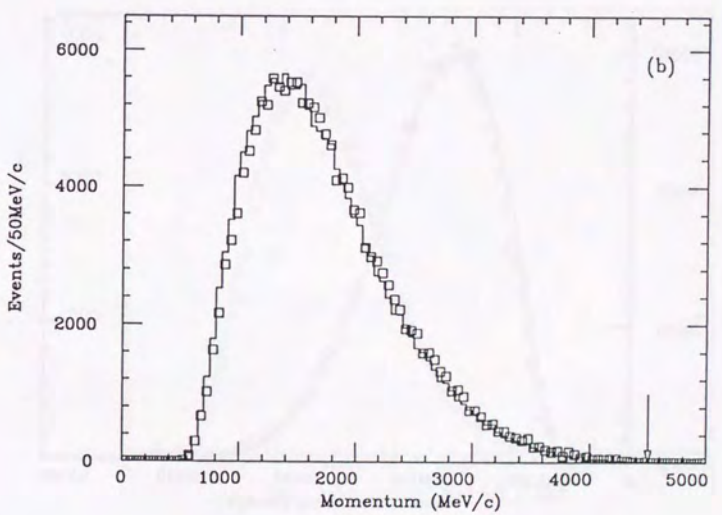

Fig. 4.15

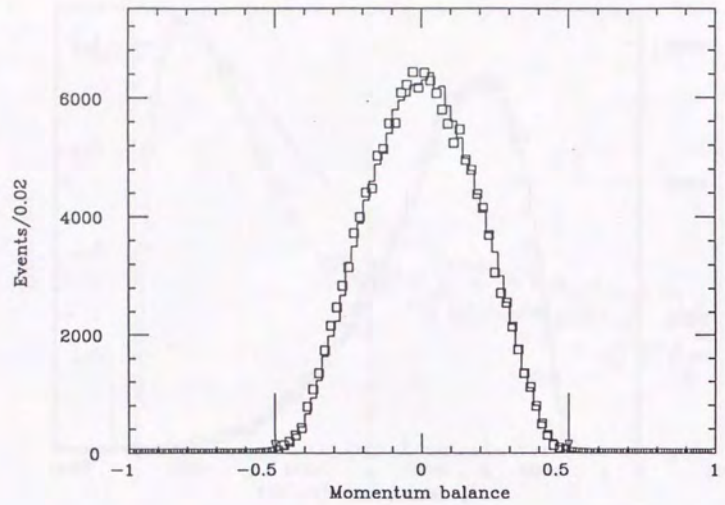

Fig. 4.16

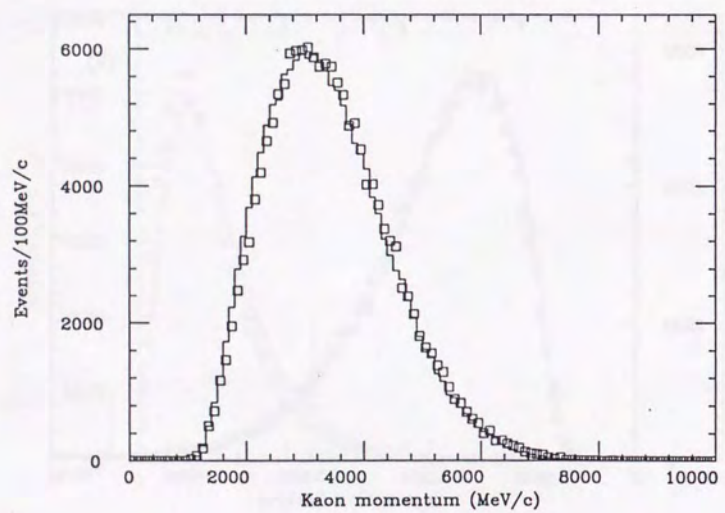

Fig. 4.17

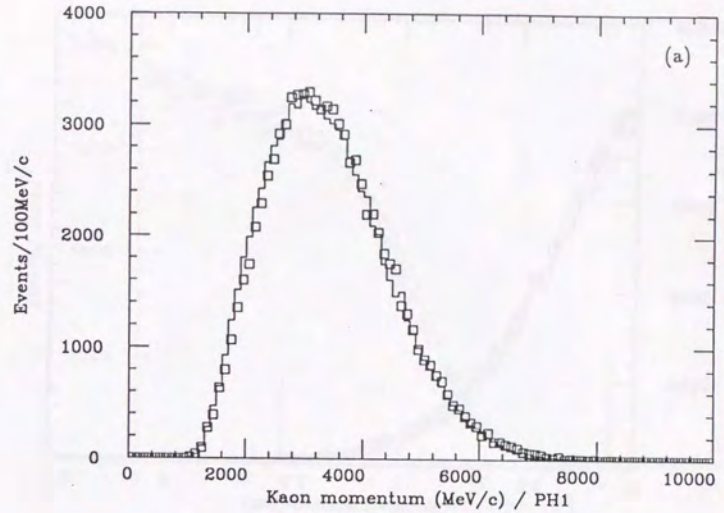

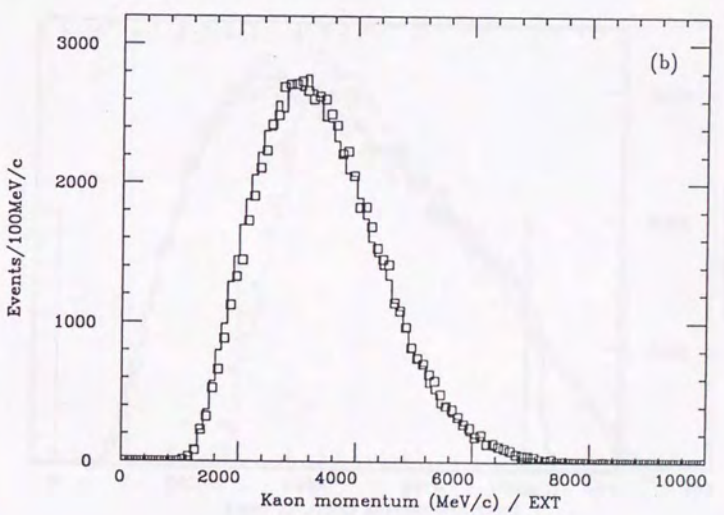

Fig. 4.18

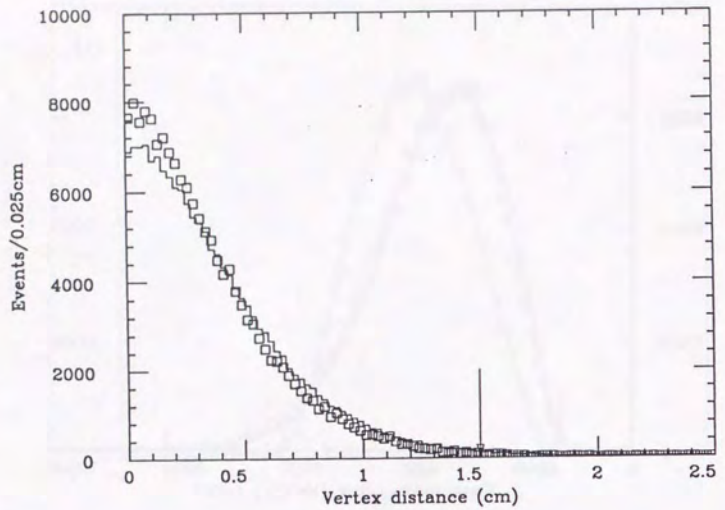

Fig. 4.19

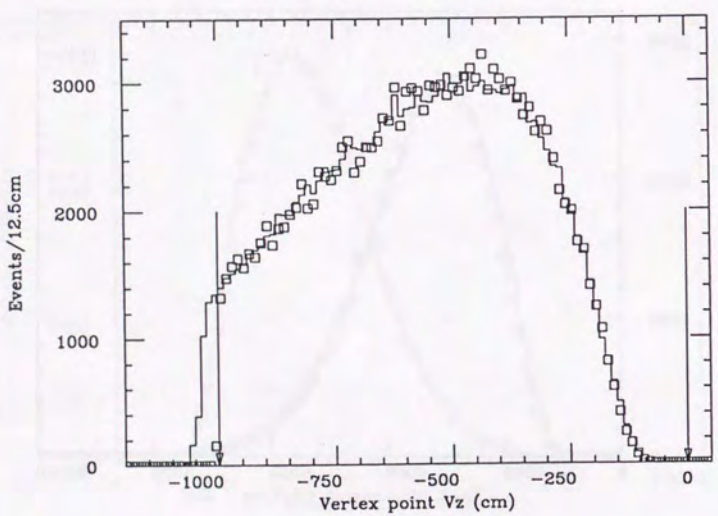

Fig. 4.20

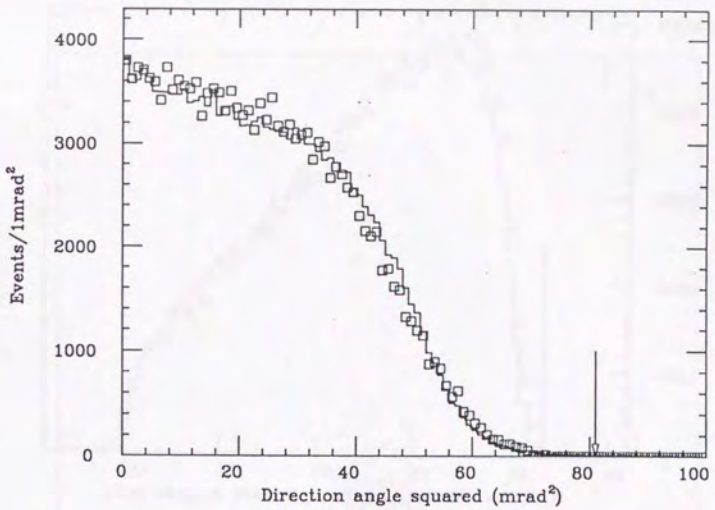

Fig. 4.21

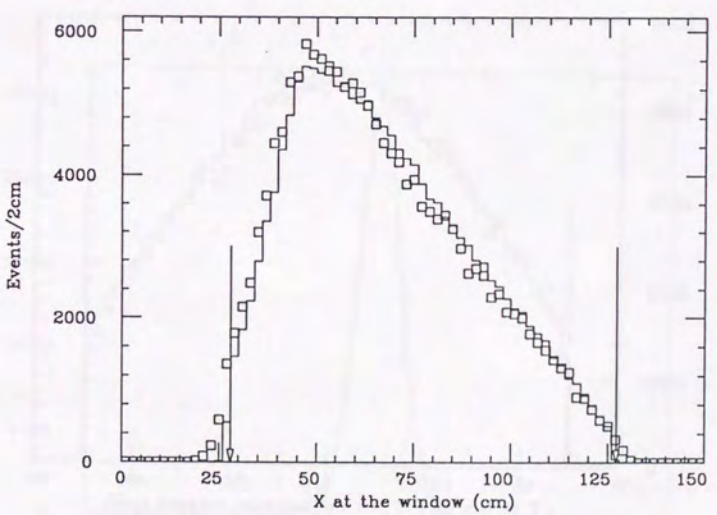

Fig. 4.22

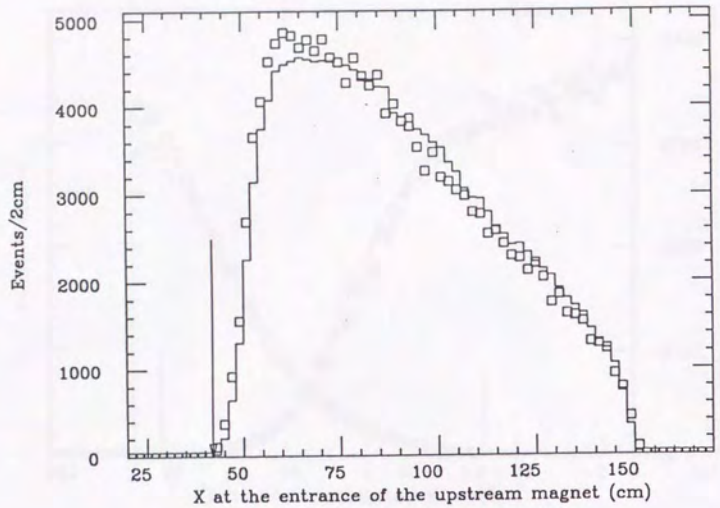

Fig. 4.23

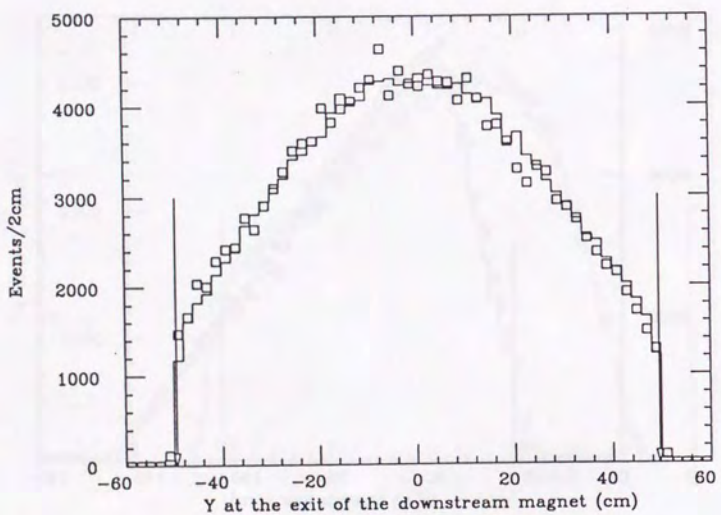

Fig. 4.24

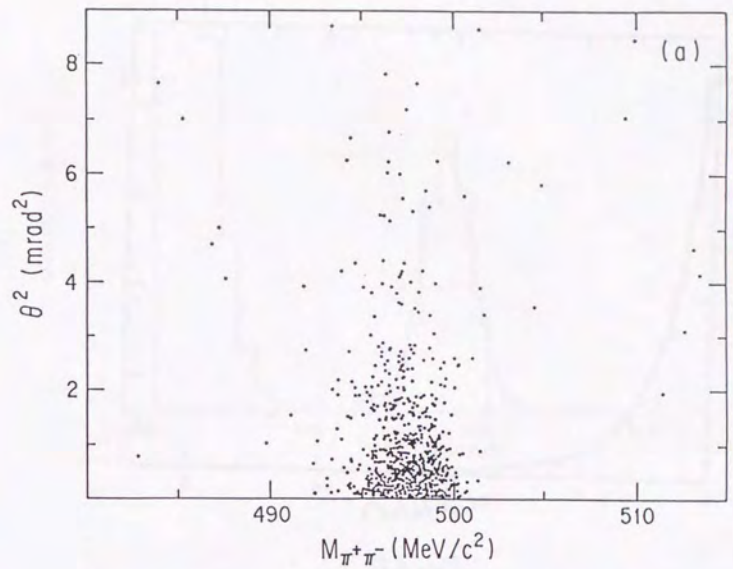

Fig. 4.25

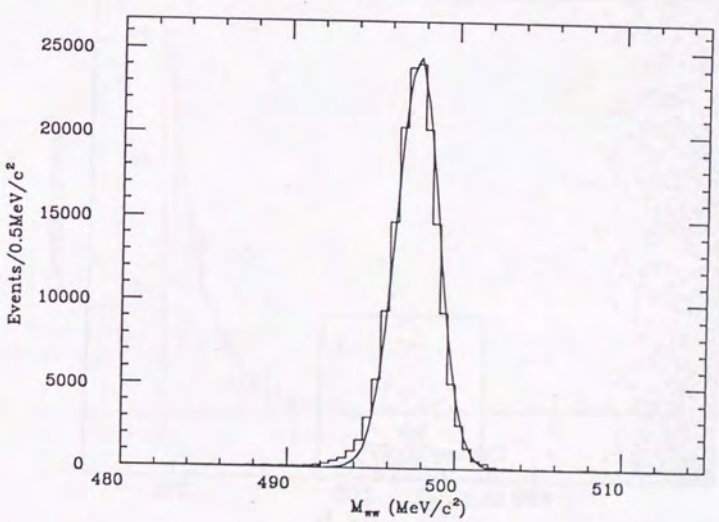

Fig. 4.26

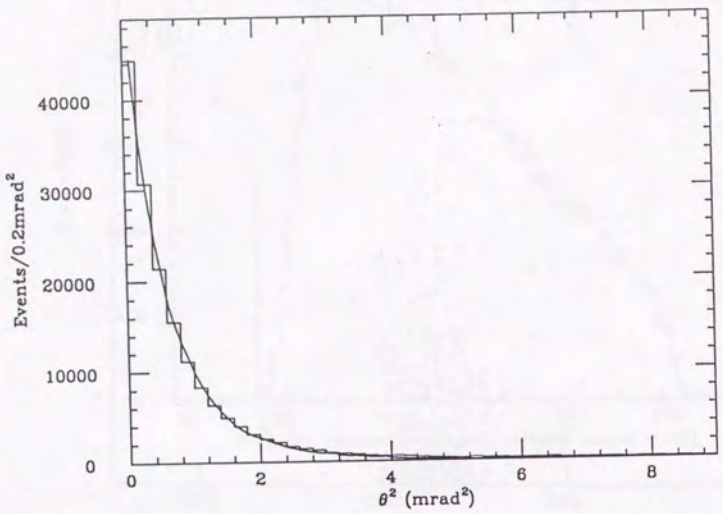

Fig. 4.27

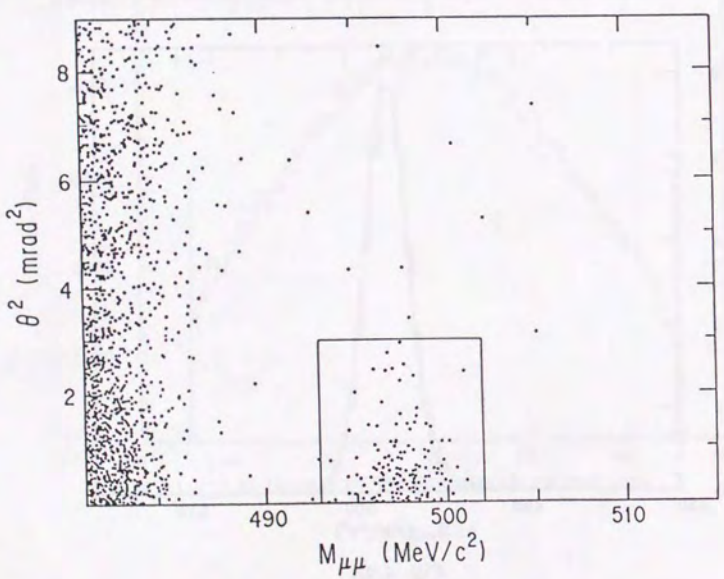

Fig. 4.28

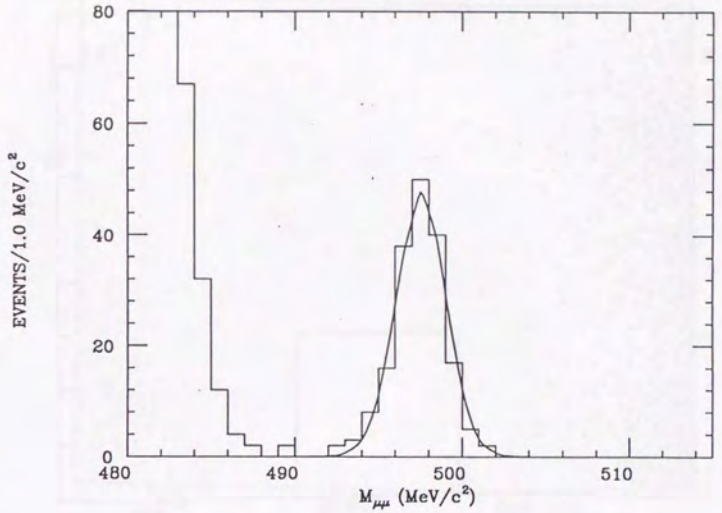

Fig. 4.29

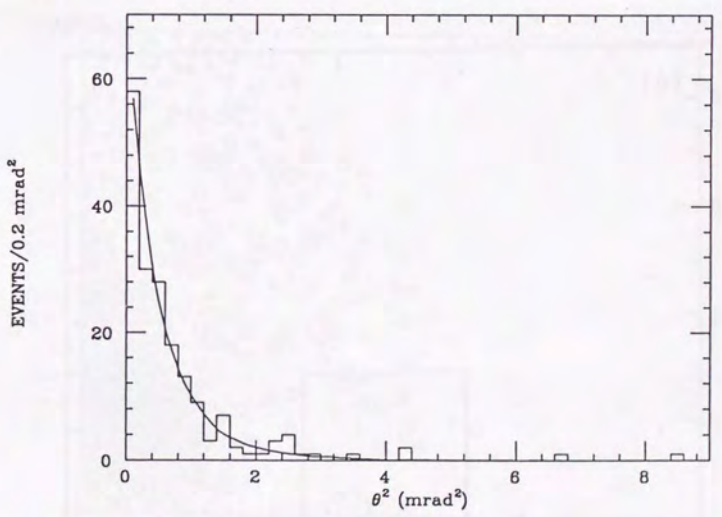

Fig. 4.30

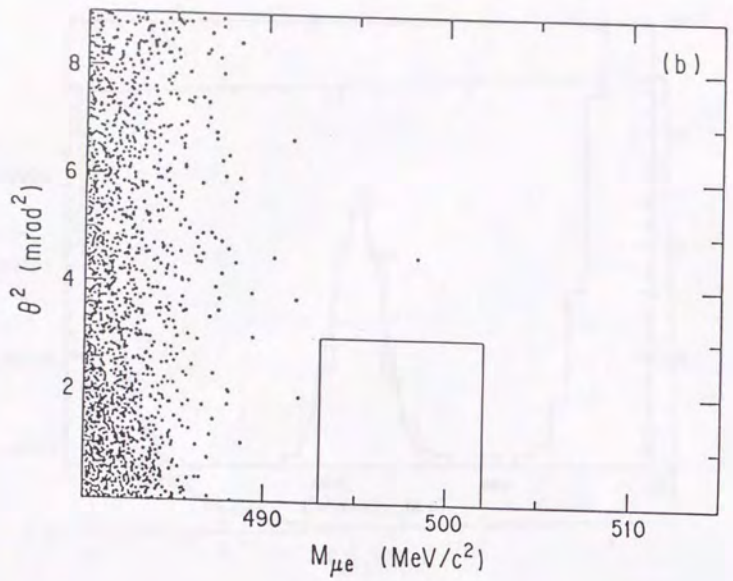

Fig. 4.31

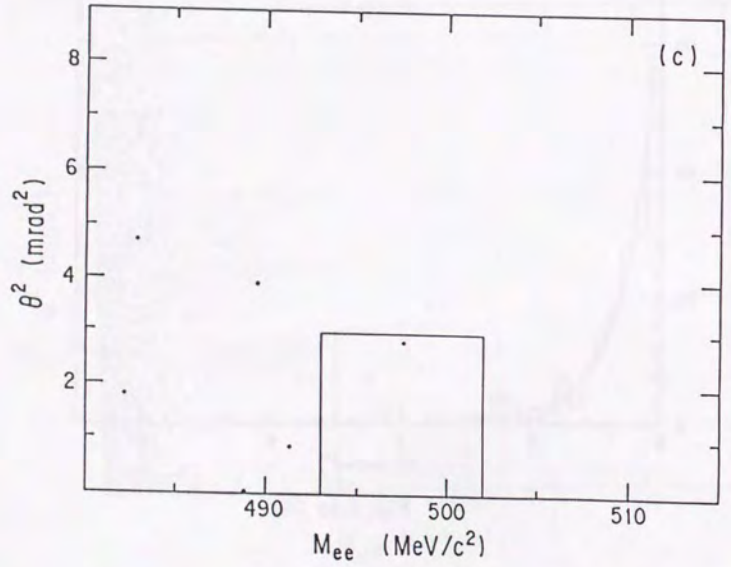

Fig. 4.32

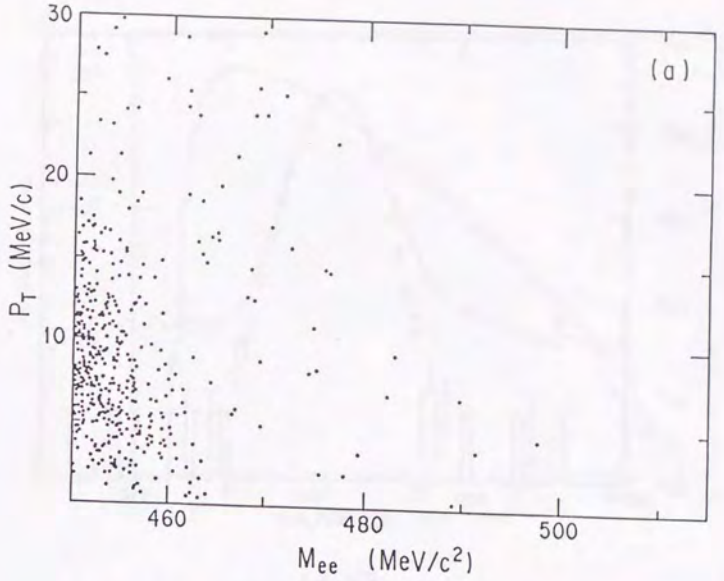

Fig. 4.33

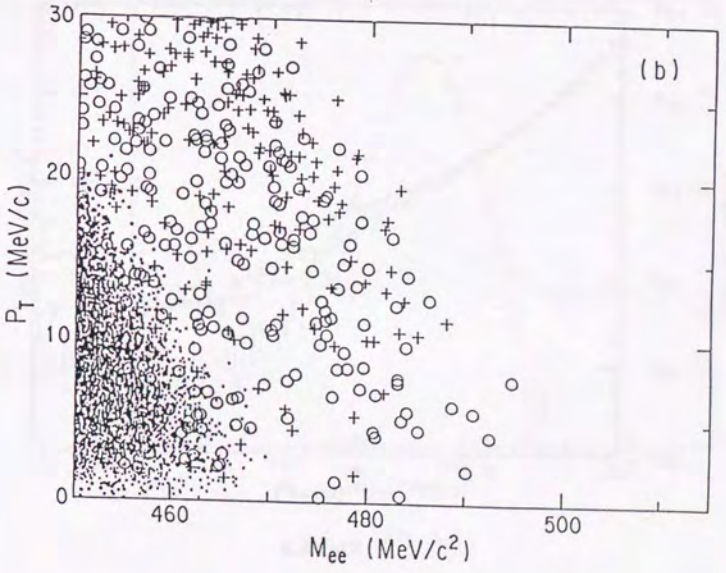

Fig. 4.34

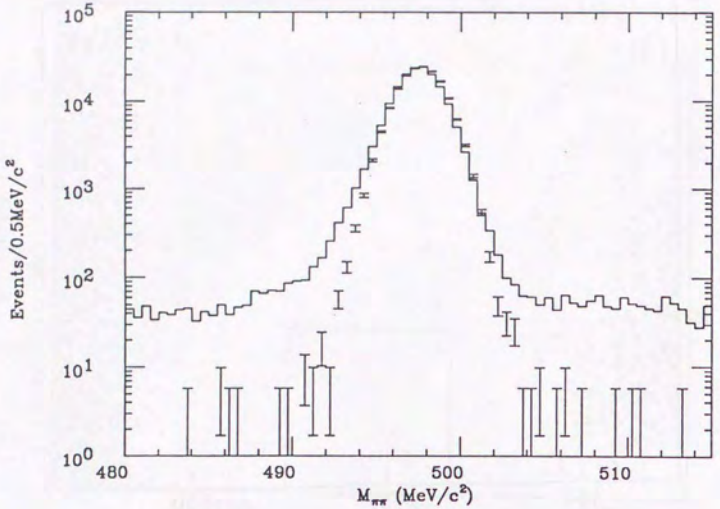

Fig. 5.1

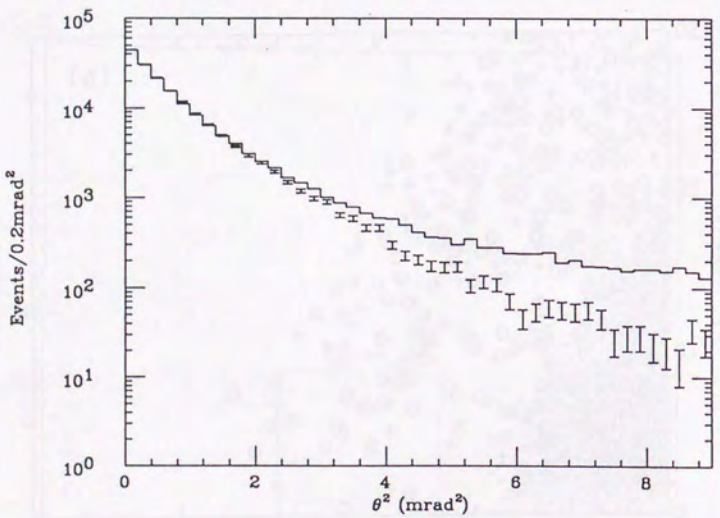

Fig. 5.2

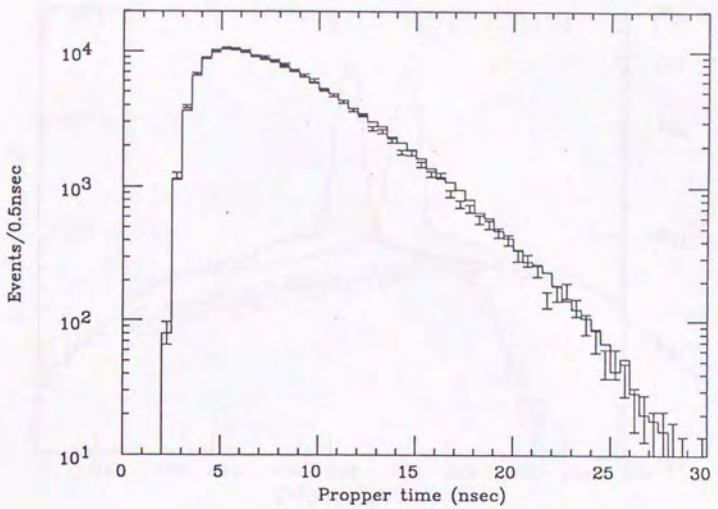

Fig. 5.3

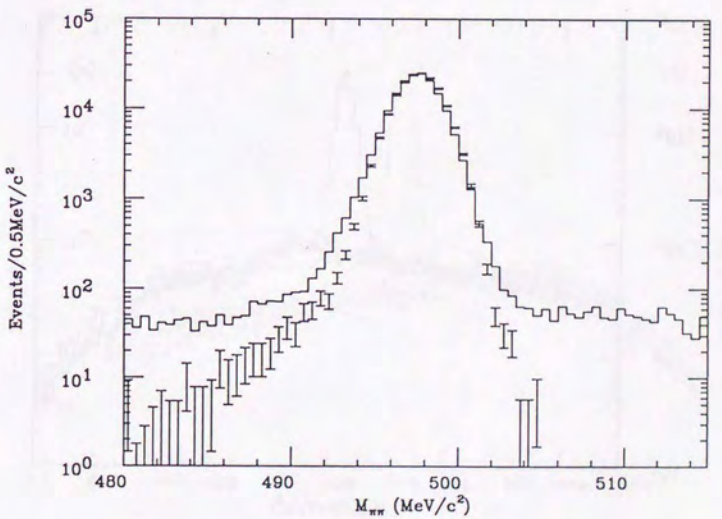

Fig. 5.4

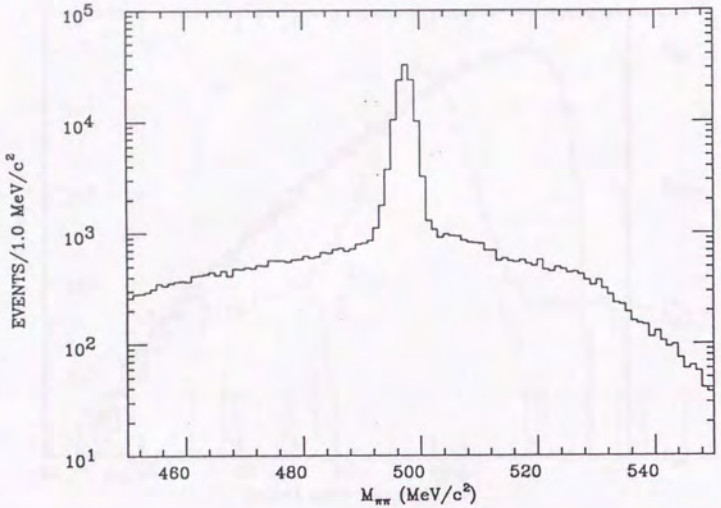

Fig. 5.5

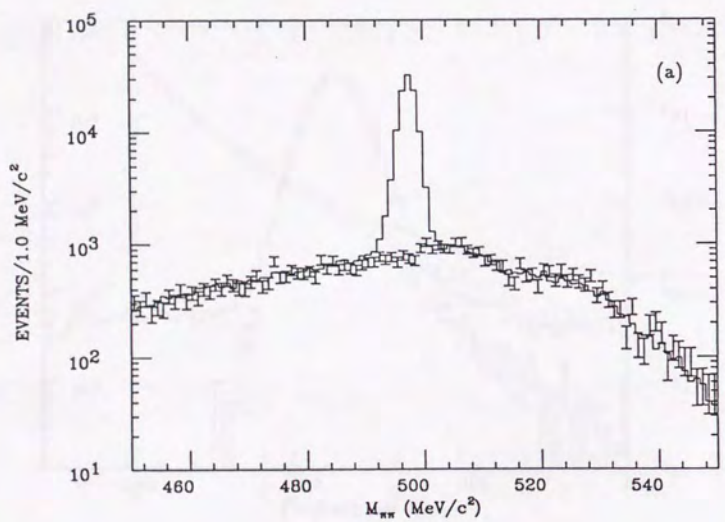

Fig. 5.6

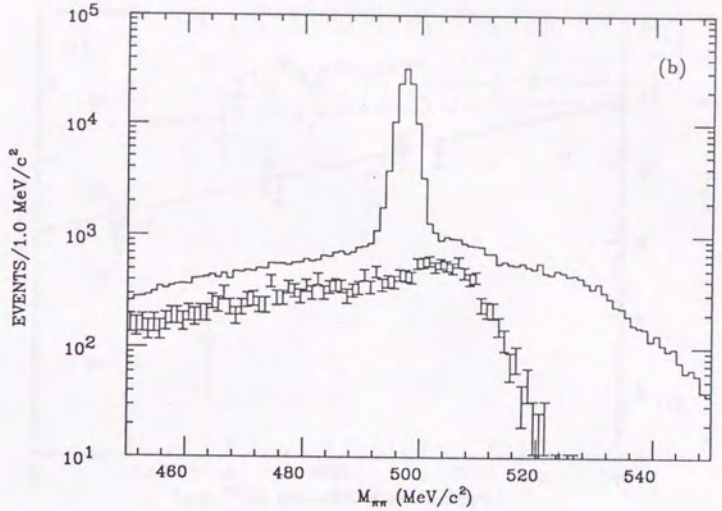

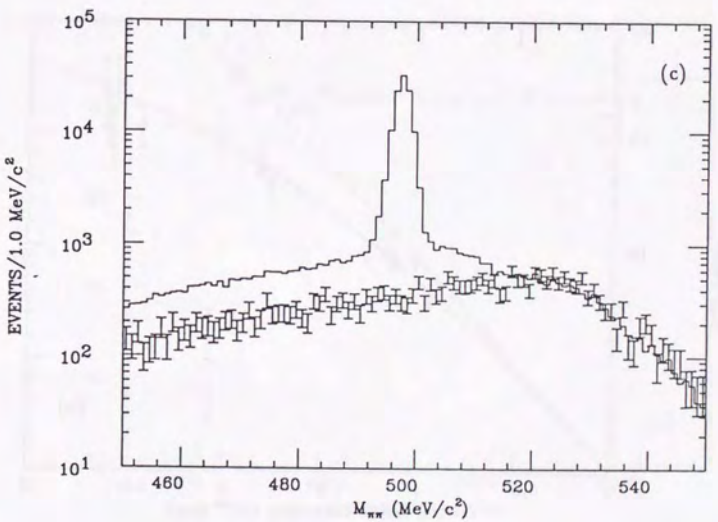

Fig. 5.6

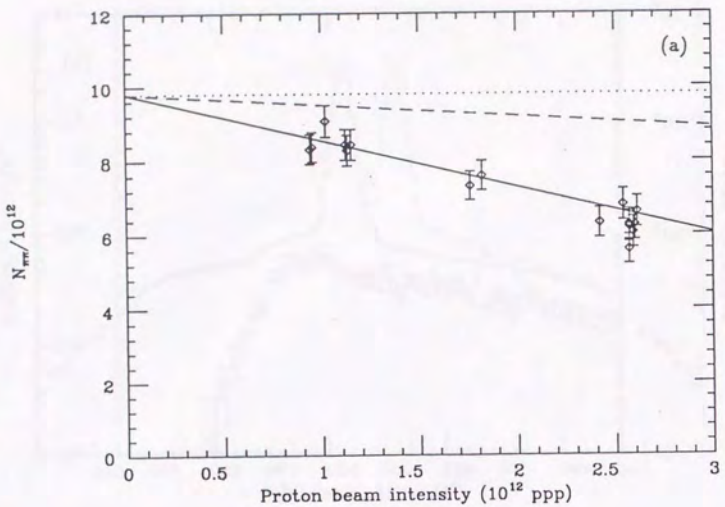
(a)
$N_{\pi^0}/10^{12}$
Proton beam intensity (10^{12} ppp)

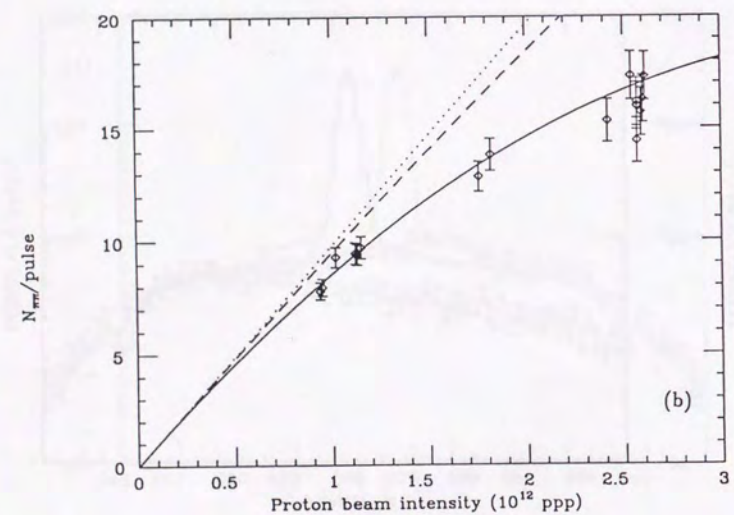
(b)
N_{π^0}/pulse
Proton beam intensity (10^{12} ppp)

Fig. 5.7

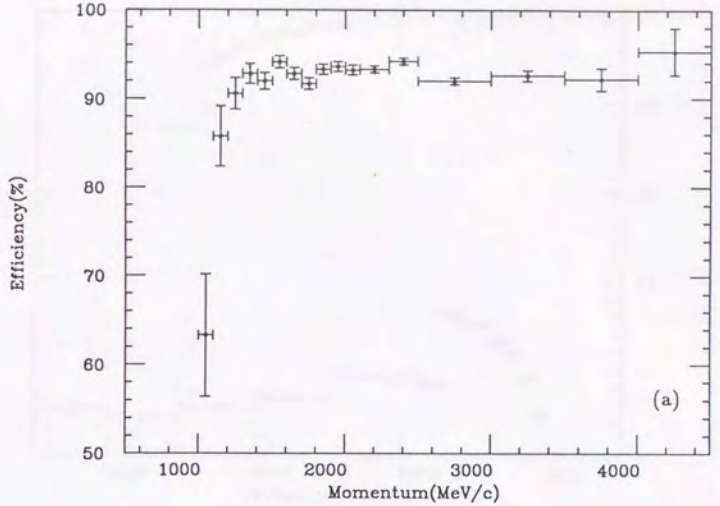
(a)
Efficiency(%)
Momentum(MeV/c)

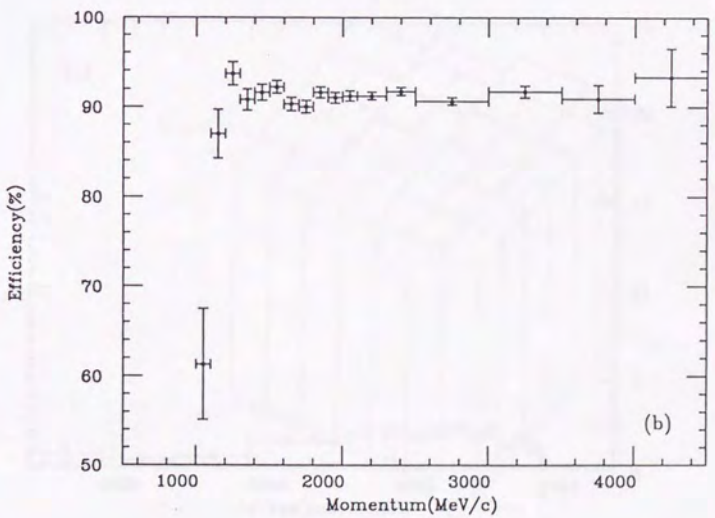
(b)
Efficiency(%)
Momentum(MeV/c)

Fig. 5.8

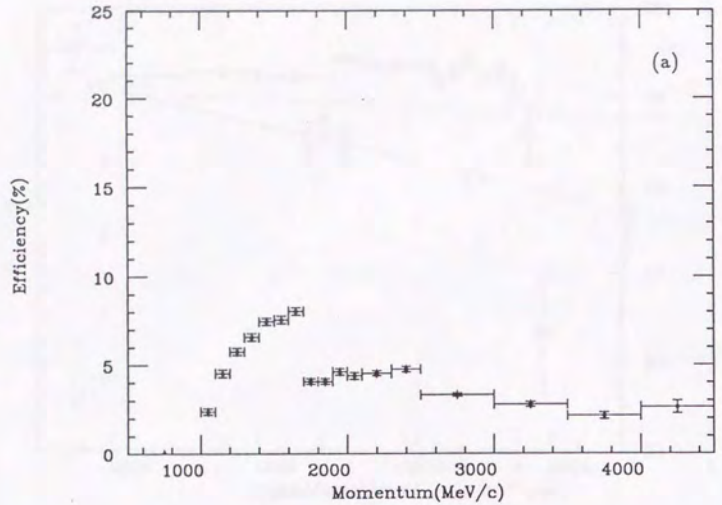

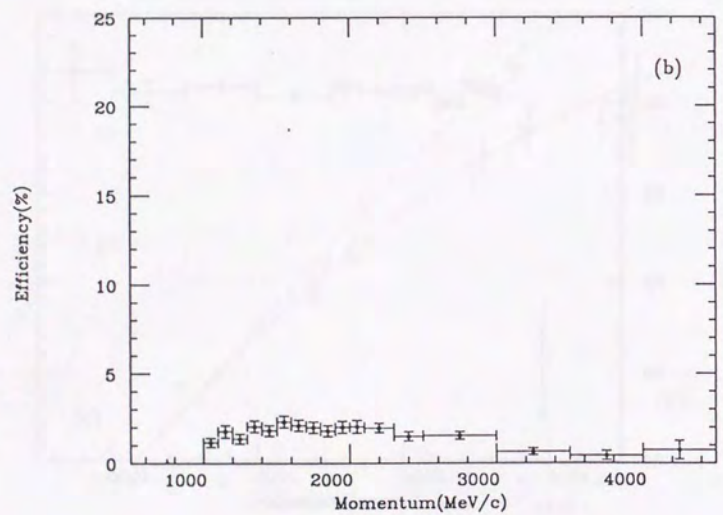

Fig. 5.9

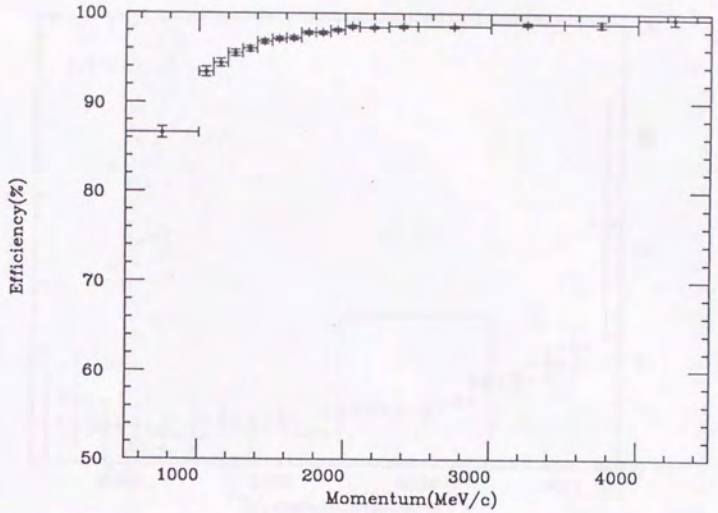

Fig. 5.10

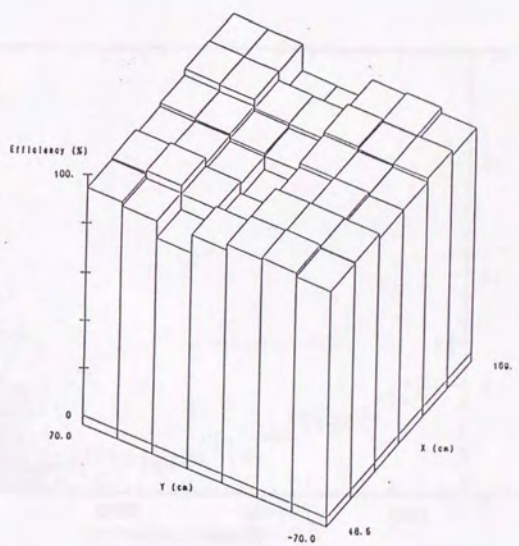

Fig. 5.11

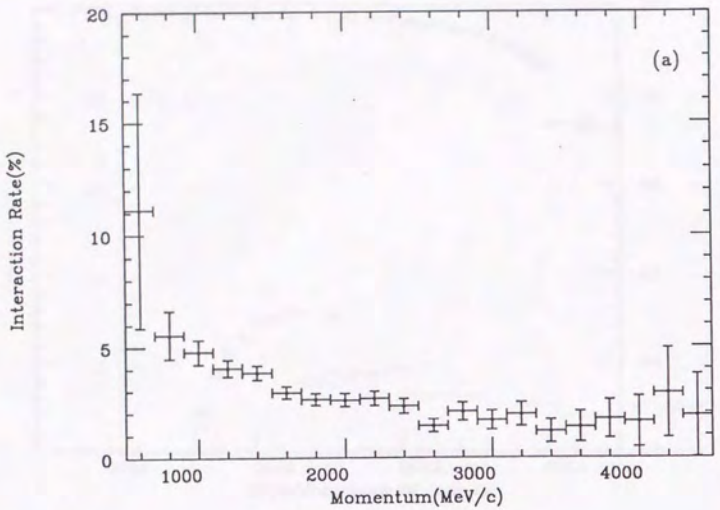

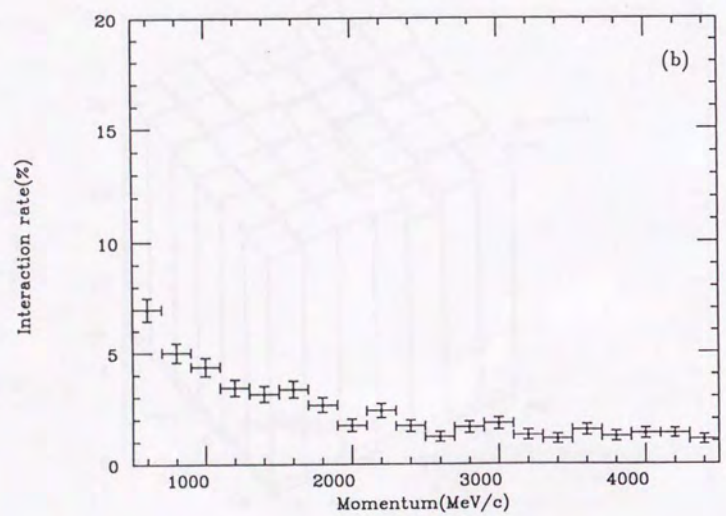

Fig. 5.12

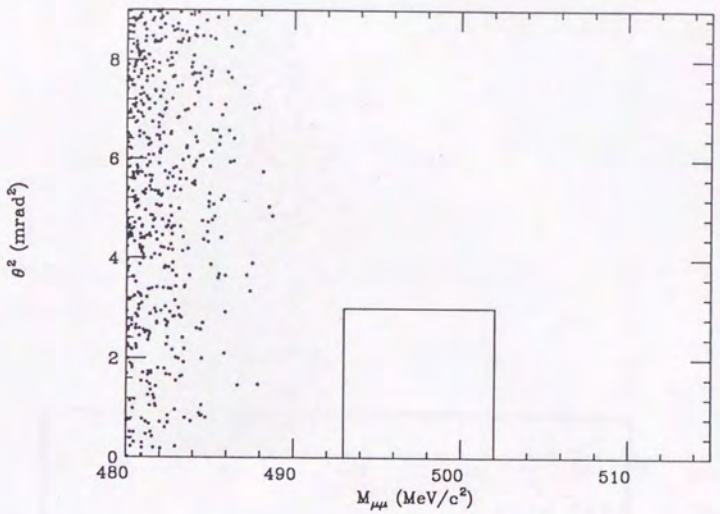

Fig. 5.13

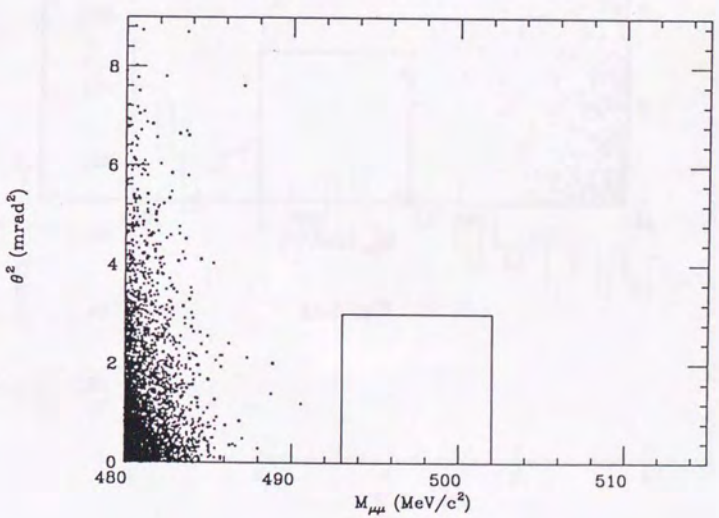

Fig. 5.14

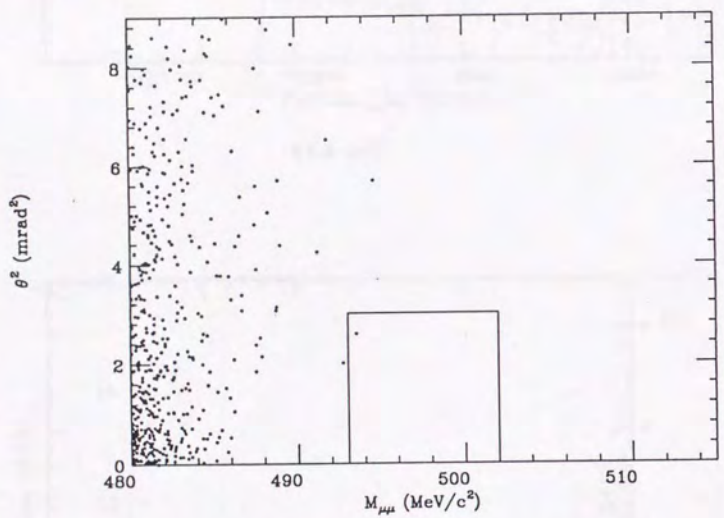

Fig. 5.15

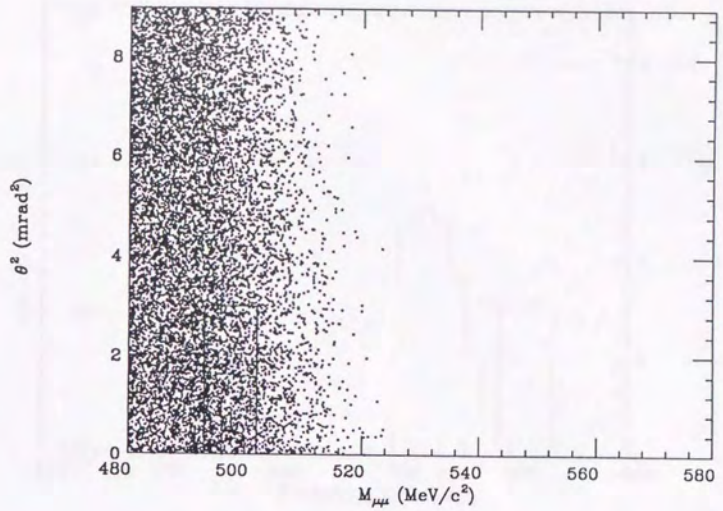

Fig. 5.16

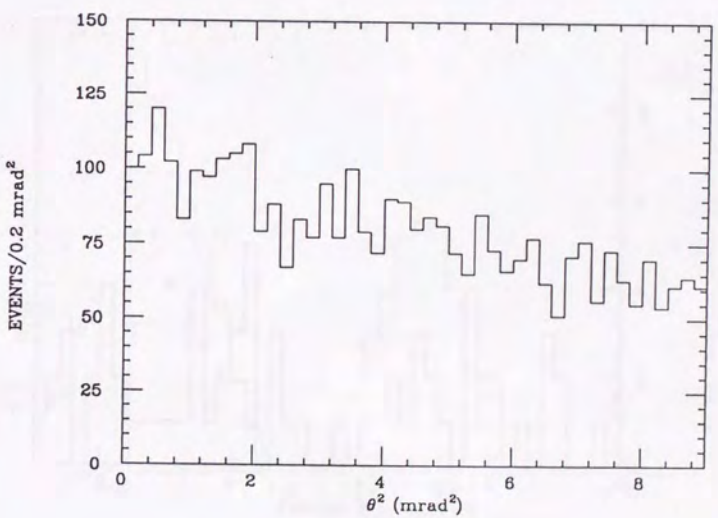

Fig. 5.18

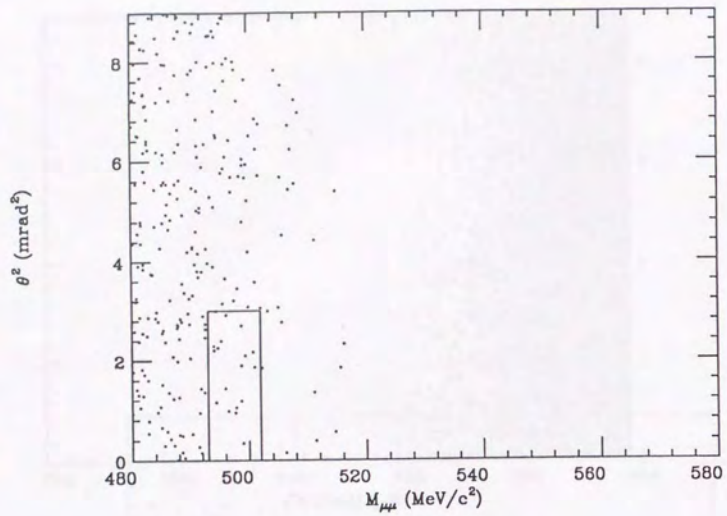

Fig. 5.17

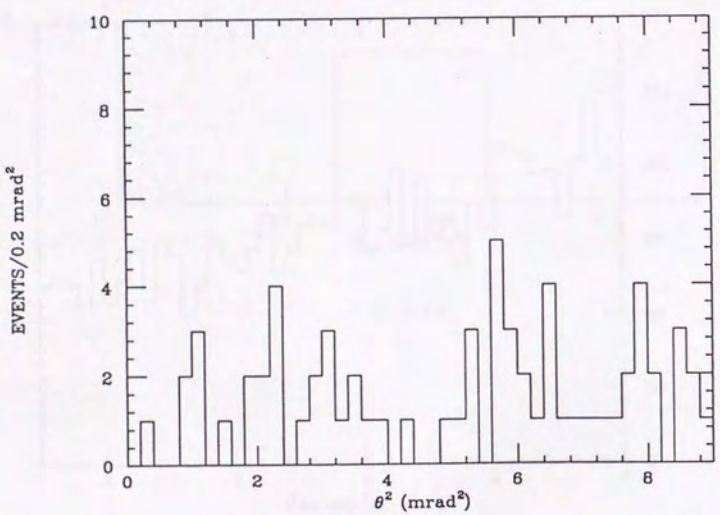

Fig. 5.19

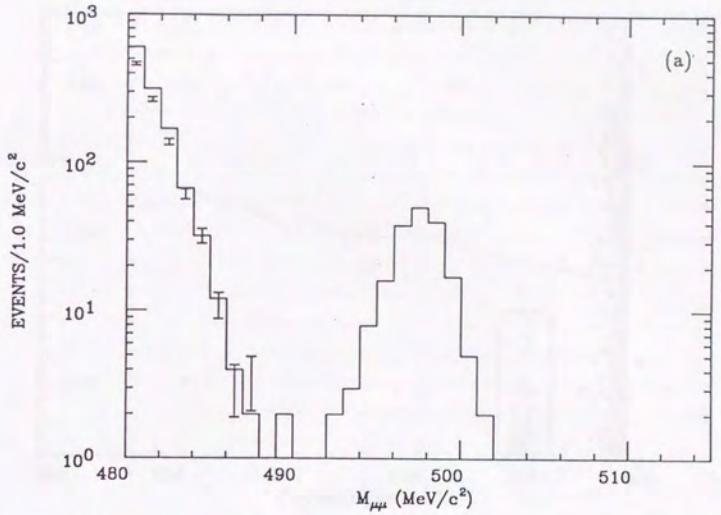

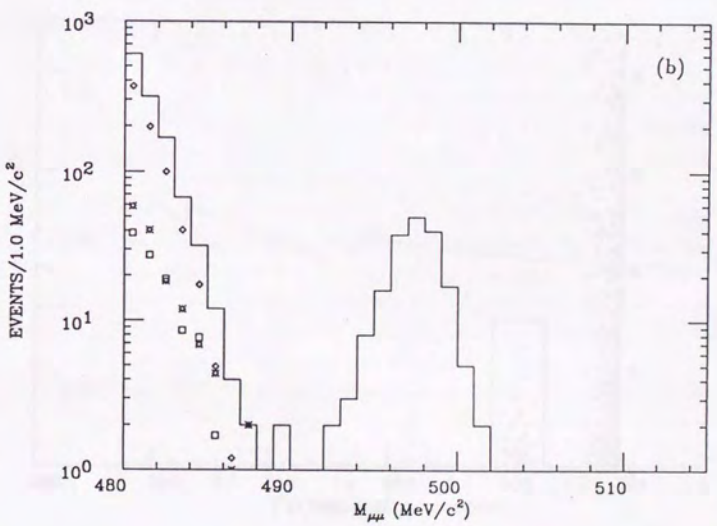

Fig. 5.20

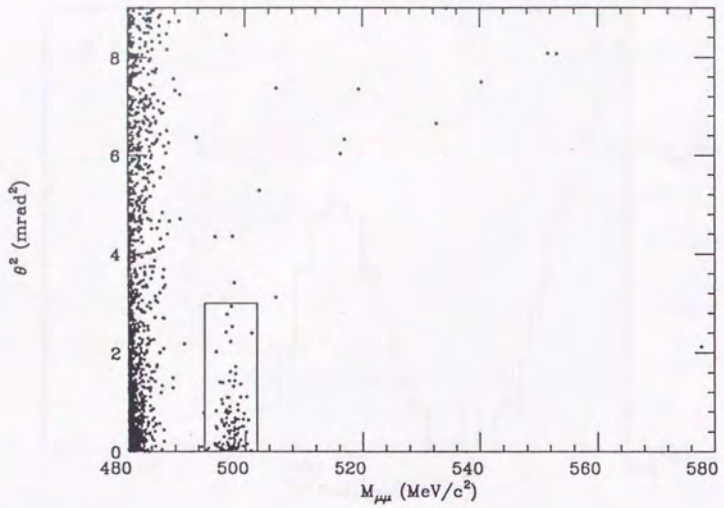

Fig. 5.21

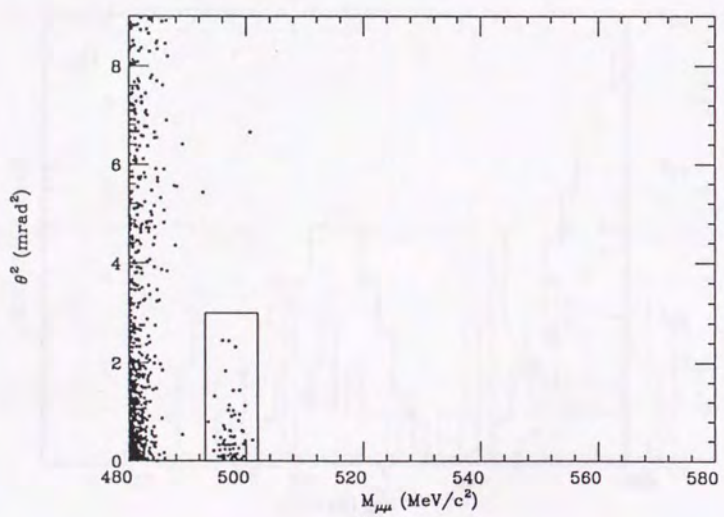

Fig. 5.22

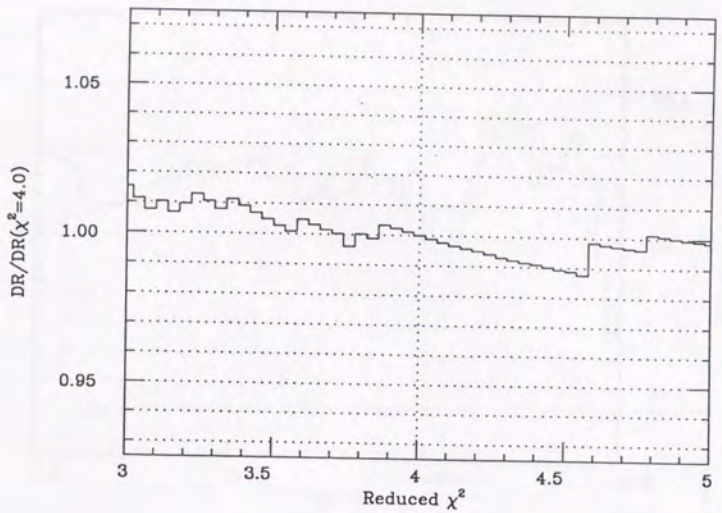

Fig. 5.23

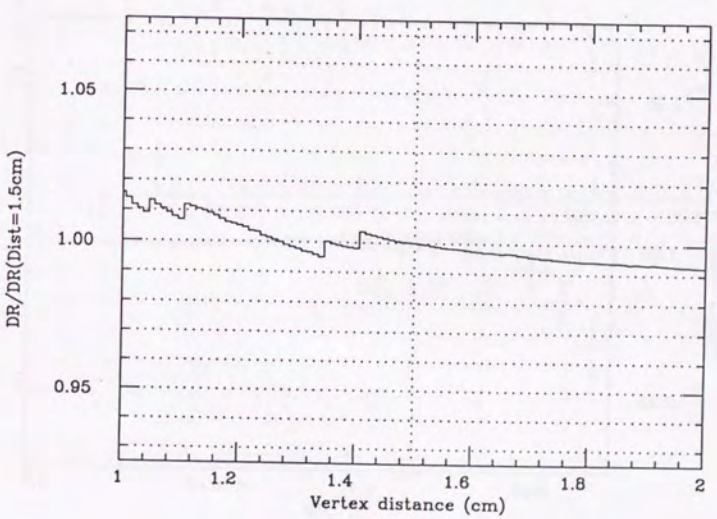

Fig. 5.24

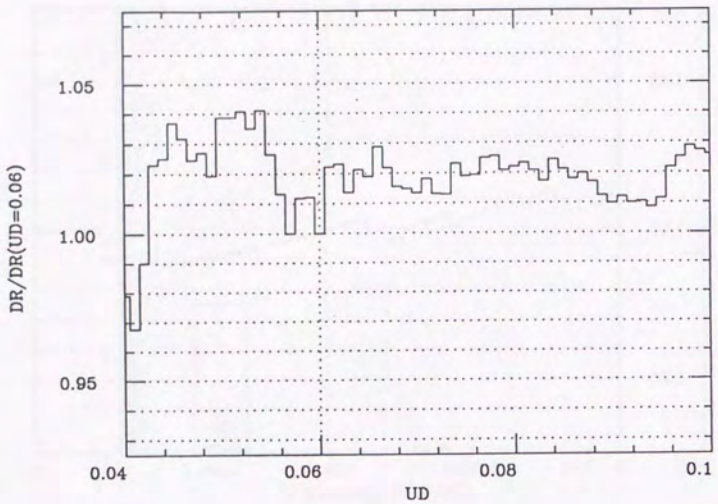

Fig. 5.25

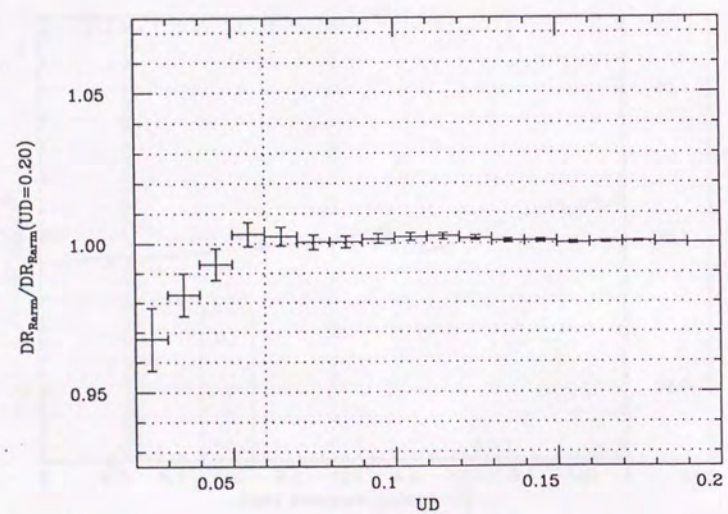

Fig. 5.26

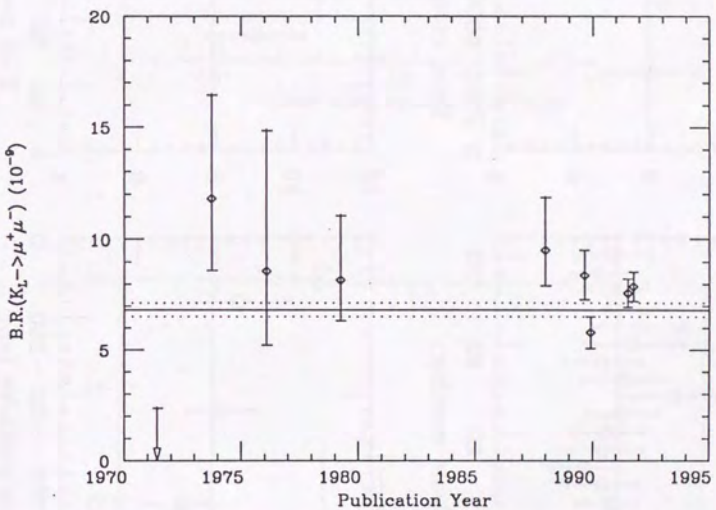

Fig. 5.27

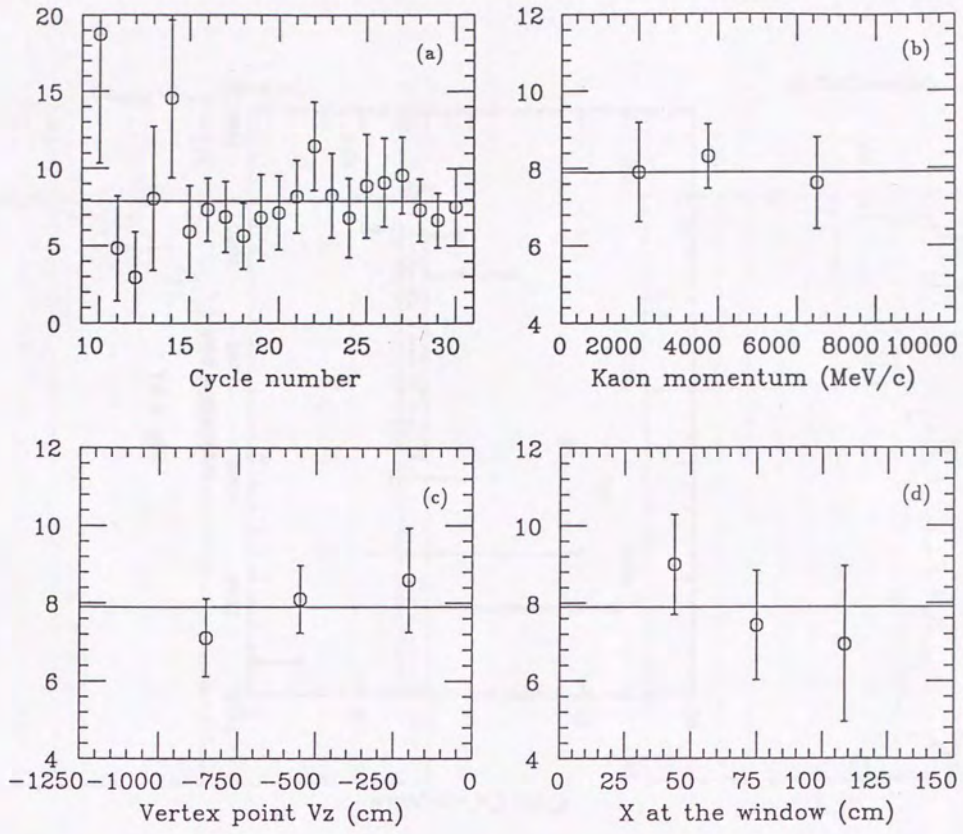

Fig. 5.28

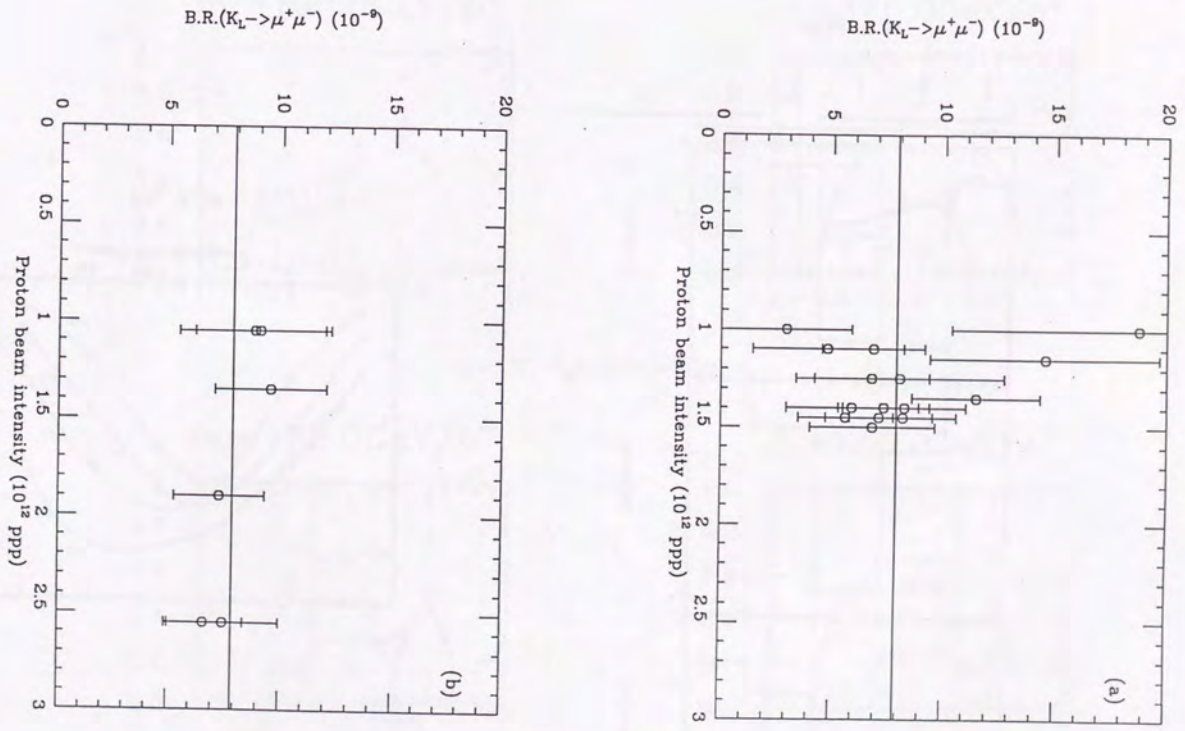

Fig. 5.29

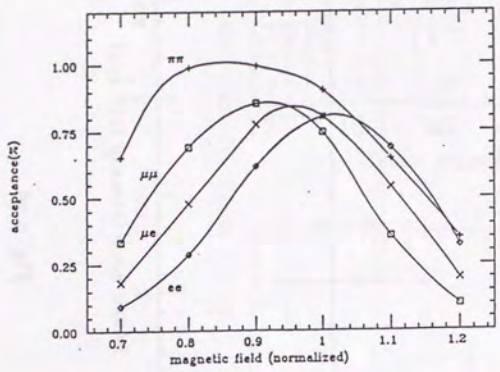

Fig. 5.30

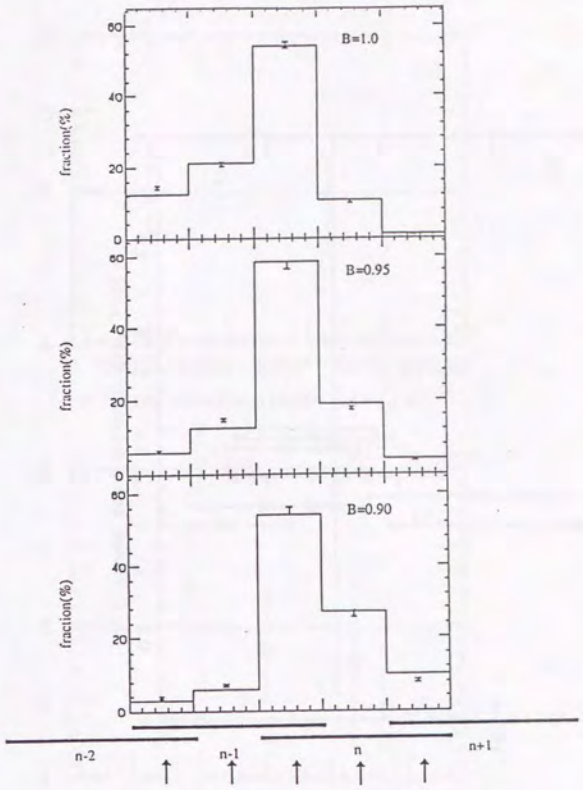

Fig. 5.31

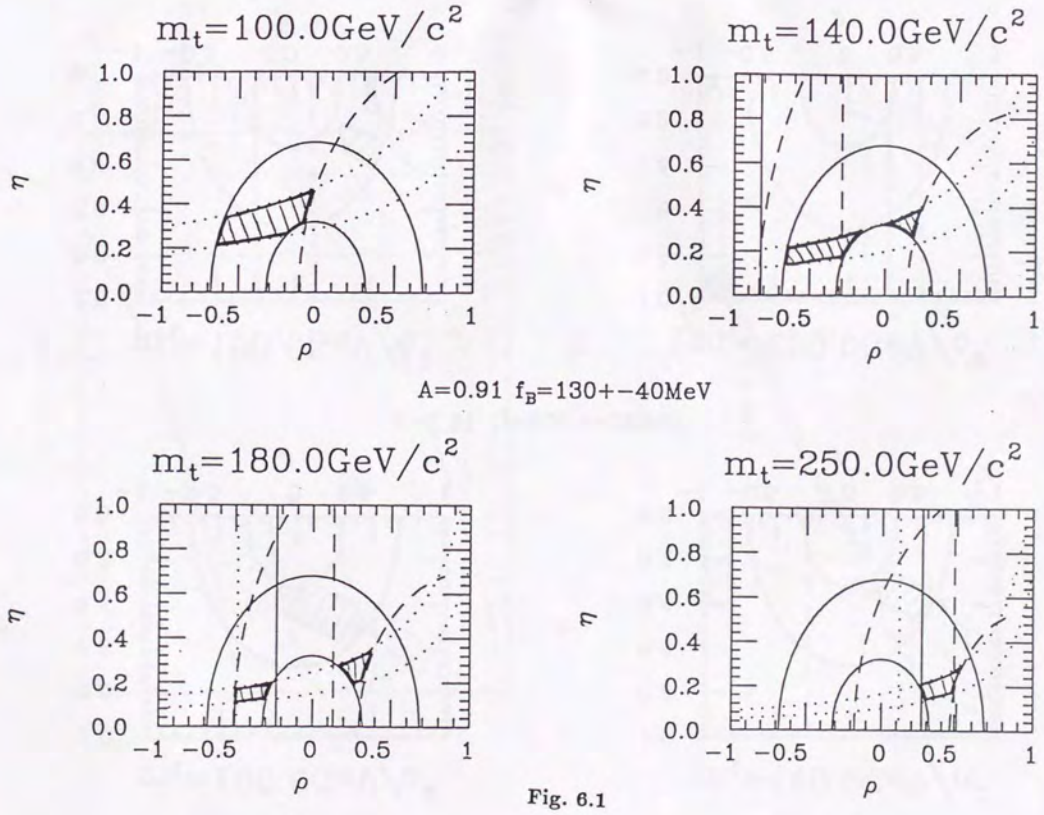

Fig. 6.1

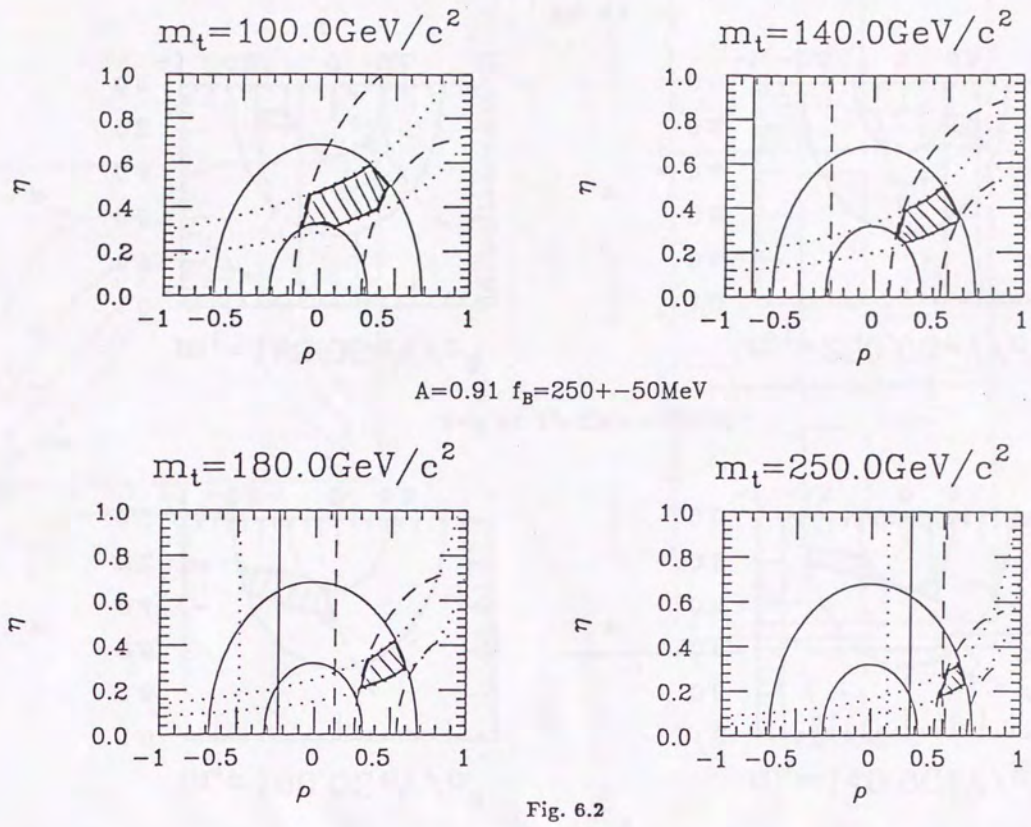

A=0.91 f_B=250+−50MeV

Fig. 6.2

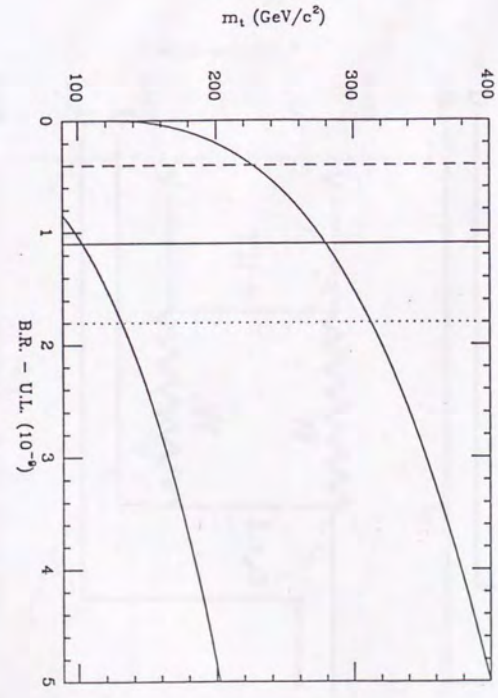

Fig. 6.4

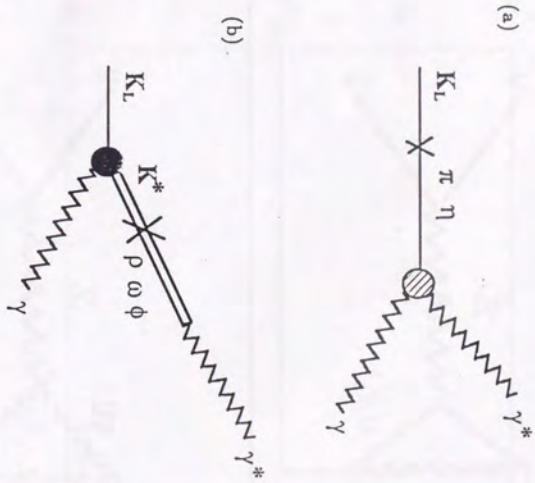

Fig. 6.3

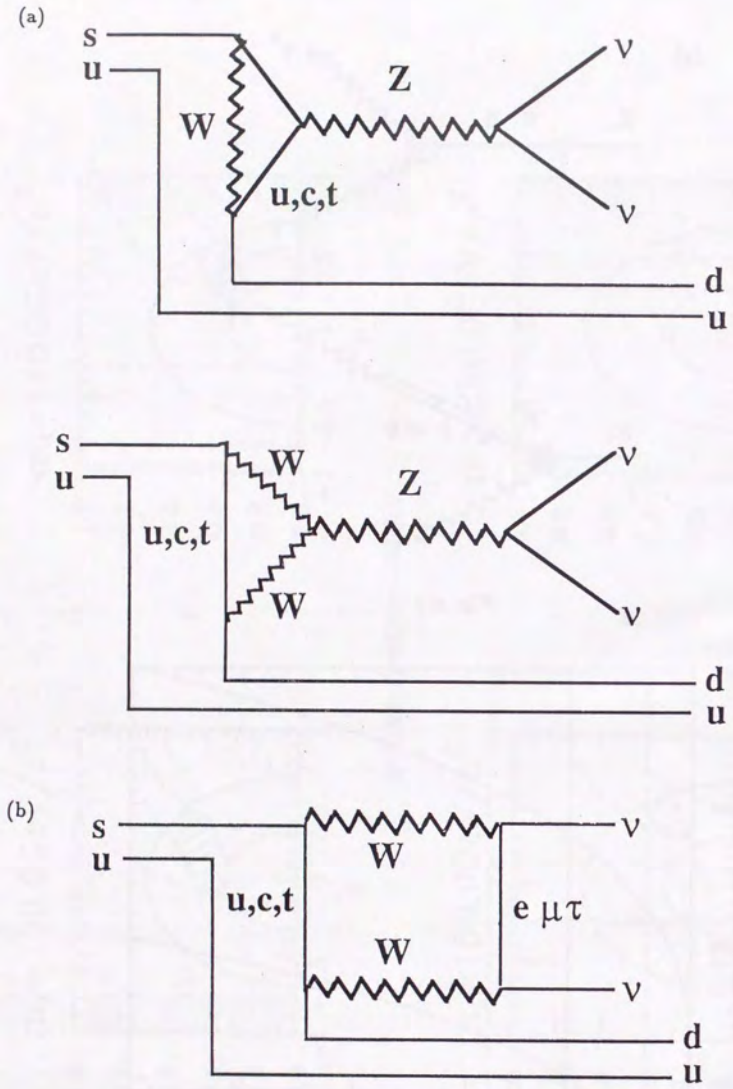
(a)
s
u
W
Z
u,c,t
ν
ν
d
u
s
u
W
Z
u,c,t
W
ν
ν
d
u
(b)
s
u
W
u,c,t
e μ τ
W
ν
ν
d
u

Fig. 6.5

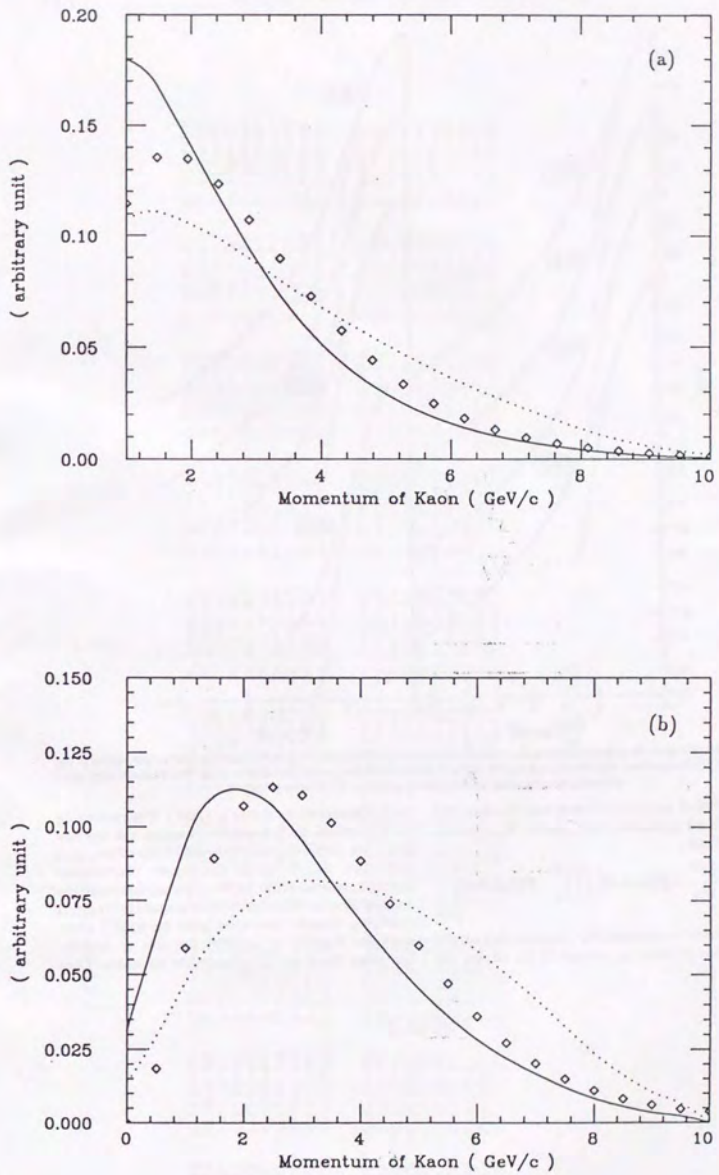
(a)
(arbitrary unit)
0.20
0.15
0.10
0.05
0.00
2
4
6
8
10
Momentum of Kaon (GeV/c)
(b)
(arbitrary unit)
0.150
0.125
0.100
0.075
0.050
0.025
0.000
0
2
4
6
8
10
Momentum of Kaon (GeV/c)

Fig. A.1

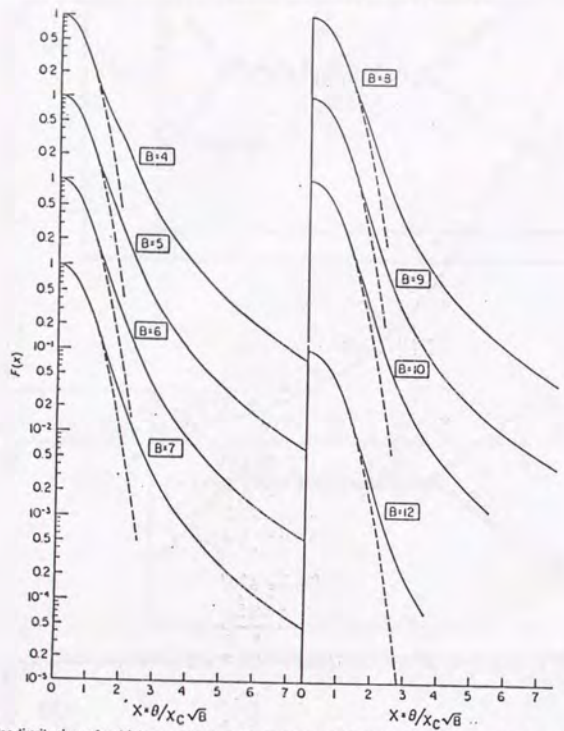

Fig. 1. Angular distributions of multiple scattering from the approximate NSW theory. The curves are given for various values of the parameter B; the independent variable is $x = \theta/(\chi_c B^{\frac{1}{2}})$. All of the curves are normalized to unity at $x = 0$. The dashed curves show Gaussian functions that have the same widths as $F(x)$ at the 1/e points.

The fraction of particles scattered into the cone with a half-angle corresponding to x_w (called $\theta_{1/e}$) can be computed from

$$\text{fraction} = \left\{\int_0^{\theta_{1/e}} F(\theta)\sin\theta\, d\theta\right\} \Big/ \left\{\int_0^{\theta_{max}} F(\theta)\sin\theta\, d\theta\right\}. \tag{31}$$

Such a calculation was made for the scattering from a 1 mg/cm² foil of nickel by protons of 10, 50 and 100 MeV. The results are shown in table 7. If the scattering were described by a Gaussian function, the fraction contained within $\theta_{1/e}$ would be 0.695. Therefore, as is clear from the shapes of the angular distributions (fig. 1), somewhat fewer particles are scattered into the forward direction than would be expected for Gaussian scattering. Graphs have been given by Ball[12]) which show the fraction of particles lost due to multiple scattering for a certain geometrical situation. These

Fig. A.2

Fig. A.3

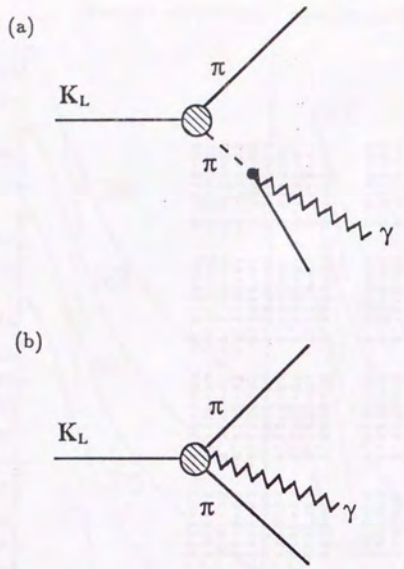
(a)
K_L
π
π
γ
(b)
K_L
π
π
γ

Fig. A.4

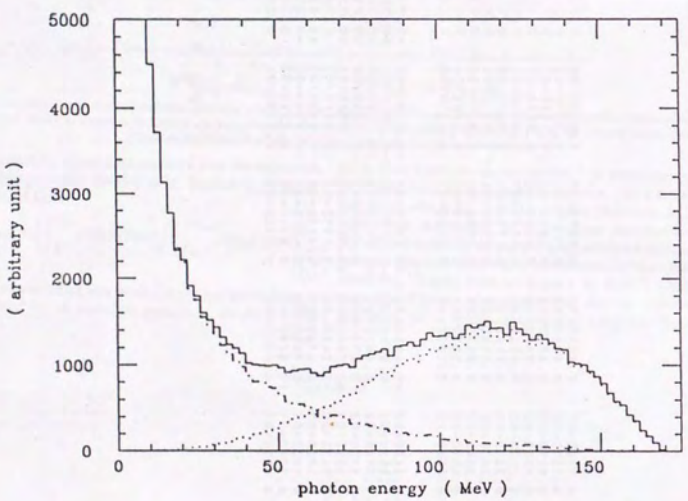
5000
4000
3000
2000
1000
0
(arbitrary unit)
0
50
100
150
photon energy (MeV)

Fig. A.5